OBSERVED CHARACTERISTICS OF CLOUDS AND PRECIPITATING SYSTEMS ASSOCIATED WITH THE TROPICAL CIRCULATION IN GLOBAL MODELS AND REANALYSES

A Dissertation

by

JUSTIN PAUL STACHNIK

Submitted to the Office of Graduate Studies of
Texas A&M University
in partial fulfillment of the requirements for the degree of

DOCTOR OF PHILOSOPHY

Approved by:

Chair of Committee,	Courtney Schumacher
Committee Members,	Benjamin Giese
	Robert Korty
	R. Lee Panetta
Head of Department,	Ping Yang

May 2013

Major Subject: Atmospheric Sciences

ABSTRACT

This dissertation presents a series of work related to the representation of the Hadley circulation (HC) in atmospheric reanalyses and general circulation models (GCMs), with connections to the underlying tropical and subtropical cloud systems that comprise the mean meridional circulation. An intercomparison of eight atmospheric reanalyses showed that significant variability exists in the mean state for HC intensity, with less variability in HC width. Ensemble trends were broadly consistent with previous work and suggest a strengthening and widening of the tropical circulation over the last 30 years.

Composite profiles of the apparent heat source and moisture sink were calculated for the International Satellite Cloud Climatology Project (ISCCP) cloud regimes using sounding observations from 10 field campaigns. Distinct heating profiles were determined for each ISCCP cloud regime, ranging from strong, upper-tropospheric heating for mesoscale convective systems to integrated cooling for populations associated with marine stratus and stratocumulus clouds. The derived profiles were generally similar over land and ocean with the notable exception of the fair-weather cumulus regime, which leads to some uncertainty in the mid- and upper-level reconstruction of subtropical heating.

An instrument simulator indicated that low-latitude cloud properties from the NASA MERRA reanalysis qualitatively matched the distributions of cloud-top pressure and optical thickness in the ISCCP data, though the tallest and thickest clouds were

missing from the reanalysis. Simulator results were sensitive to the choice of cloud overlap parameterization and the reanalysis consistently underpredicted the observed cloud fractions for all regimes. The vertical velocity, temperature, and moisture for each regime in MERRA largely matched observations from previous studies, suggesting that the dynamic and thermodynamic properties of the cloud regimes are well captured by the reanalysis.

Finally, HC interannual variability was examined as a function of the observed frequency of the ISCCP cloud regimes. The strongest HC overturning events were attributed to an El Niño response in the central Pacific Ocean in addition to links between the intensity and position of the Pacific ITCZ. The ISCCP regime describing the most vigorous and organized convection contributed the most towards the total anomalous heating during HC extremes, despite an overall low frequency of occurrence. Idealized GCM simulations forced with the observed three-dimensional diabatic heating from ISCCP data produced too strong a HC with some improvement in other fields. Overall, much progress has been made regarding the links between low-latitude cloud systems and the HC, though future work will continue to address the upscale feedbacks of regional cloud variations upon the tropical circulation.

ACKNOWLEDGEMENTS

I would like to thank my advisor and committee chair, Dr. Courtney Schumacher, for her never-ending guidance, wisdom, and support for my doctoral research. Thank you for having the patience to let me explore my passions in research and teaching while providing the necessary help if I ever felt off track! I hope you are as proud of our work as I am and I look forward to future collaborations for years to come. Additional thanks are given to my other committee members, Drs. Benjamin Giese, Rob Korty, and Lee Panetta, for their service and help in shaping my dissertation research.

Special thanks are needed for those people who provided collaborative support including Paul Ciesielski and Cara-Lyn Lappen. Drs. Shaimi Nasiri and Gerald North of the Texas A&M University faculty also provided support during early conversations pertaining to sections of this work.

Thanks also go to my past and present fellow A-Team members, with special acknowledgements for Larry Hopper and Elinor Martin for their friendship and professional support. I would also like to thank my many students over the years from labs, lectures, and the research environment. They have helped me discover one of my true passions and purpose in life and I learned more from them than they likely realize.

This study was funded by the National Science Foundation (NSF) grant ATM-0449782 and the National Aeronautics and Space Administration (NASA) grants NNX 10AG89G and NNX 10AG81G. Partial funding support was also provided via a teaching assistantship through the Department of Atmospheric Sciences.

Finally, special thanks to all those people both near and far throughout the last few years who provided a simple genuine hello and gave me reason to smile. I could not have done it without you.

TABLE OF CONTENTS

CHAPTER Page

I INTRODUCTION 1

II A COMPARISON OF THE HADLEY CIRCULATION IN MODERN REANALYSES 5

1. Introduction 5
2. Data and Methods 8
   a. Reanalysis Data 8
   b. Other Data 12
3. Results 13
   a. HC Climatology and Ensemble Variability 13
   b. Trends in HC Intensity and Width 17
   c. Interannual Variability and Connections to ENSO 21
4. Summary and Discussion 26

III TOTAL HEATING CHARACTERISTICS OF THE ISCCP TROPICAL AND SUBTROPICAL CLOUD REGIMES 31

1. Introduction 31
2. Data and Methods 34
   a. ISCCP Weather States 34
   b. Large-scale Budget Data 38
   c. Other Data 43
3. Results 44
   a. Q_1 Profiles 44
   b. Q_2 Profiles 51
4. Applications 53
   a. Comparisons to CAM4 Heating 54
   b. Heating Anomalies during the MJO 55
5. Summary and Discussion 58

IV TROPICAL AND SUBTROPICAL CLOUD REGIMES IN THE MERRA REANALYSIS USING AN ISCCP SIMULATOR 62

1. Introduction 62
2. Data and Methods 65
   a. ISCCP Weather States 65
   b. Reanalysis Data 67

CHAPTER Page

c. ISCCP Simulator 69
3. Results 72
a. Evaluation of Simulated MERRA Cloud Regimes 72
b. Trends in the Simulated Regimes 76
c. Large-scale Environmental Conditions 78
4. Summary and Discussion 81

V AN OBSERVATIONAL DECOMPOSITION AND MODEL RECONSTRUCTION OF CLOUDS AND PRECIPITATING SYSTEMS ASSOCIATED WITH THE HADLEY CIRCULATION 87

1. Introduction 87
2. Data and Methods 90
a. Reanalysis Datasets 90
b. ISCCP Cloud Regimes 92
c. Model Setup 95
3. Observational Decomposition 96
a. Cloud Regimes associated with HC Extremes 96
b. Anomalous Tropical and Subtropical Heating 100
4. Model Reconstruction 104
5. Summary and Discussion 107

VI SUMMARY AND CONCLUSIONS 113

REFERENCES 118

APPENDIX A TABLES AND FIGURES FOR CHAPTER II 137

APPENDIX B TABLES AND FIGURES FOR CHAPTER III 152

APPENDIX C TABLES AND FIGURES FOR CHAPTER IV 166

APPENDIX D TABLES AND FIGURES FOR CHAPTER V 176

LIST OF FIGURES

FIGURE		Page
A-1	Annual average, zonal mean meridional mass streamfunction values for each reanalysis dataset during the 1979-2008 period	144
A-2	Same as Fig. A-1, but for JJA	145
A-3	Same as Fig. A-1, but for DJF	146
A-4	Same as Fig. A-1, but for the multi-reanalysis ensemble average	147
A-5	Annual average, zonal mean total precipitation rate (mm day^{-1}) for the GPCP and reanalysis datasets during the 1979-2008 period	148
A-6	Time-series of the annual average, (a) maximum and (b) minimum zonally averaged meridional mass streamfunction, Ψ_N^* and Ψ_S^*, for each reanalysis during the 1958-2008 period	149
A-7	Same as Fig. A-6, but for the Hadley cell width, $\Delta\varphi$	150
A-8	Box-whisker diagram of Ψ_N^* for each reanalysis dataset during DJF for the 1979-2008 period	151
B-1	Joint histograms of cloud-top pressure and optical thickness corresponding to each of the eight weather states identified for the extended low-latitude ISCCP dataset	155
B-2	Geographic distribution of the annual average, relative frequency of occurrence for each weather state from 1984-2007	156
B-3	Campaign average, total diabatic heating (Q_1) profiles for the domains used in this study	157
B-4	Daily average, total diabatic heating (Q_1) composite profiles for the ISCCP cloud regimes	158
B-5	Observed total diabatic heating (Q_1) profiles for each domain (thick, black) and predicted reconstructions (thin, colors) using regime averages trained on the remaining field campaign datasets	159
B-6	Average total heating profiles for each regime over mostly-land (thin, solid) and mostly-ocean (thin, dashed) domains	160

FIGURE Page

B-7 Same as Fig. B-4, but for the apparent moisture sink (Q_2) 161

B-8 Same as Fig. B-6, but for the apparent moisture sink (Q_2) 162

B-9 Annual average, zonal mean total heating for (a) the ISCCP reconstruction, (b) CAM4 control run, and (c) difference quantities (ISCCP-CAM4) during 1984-2007 163

B-10 ISCCP composite heating anomalies by phase for WS8 (cumulus/shallow convection) at approximately 940 hPa for strong MJO events relative to the six-month (November-April) 1983-2008 mean 164

B-11 Vertical-temporal (MJO phases) evolution of the total ISCCP diabatic heating anomalies for strong MJO events over the (a) Indian Ocean (80°-90°E) and (b) Western Pacific (150°-160°E) throughout November-April, 1983-2008 165

C-1 Joint histograms of cloud-top pressure and optical thickness corresponding to each of the eight cloudy ISCCP weather states for the extended low-latitude dataset 168

C-2 Geographic distribution of the annual average, relative frequency of occurrence (RFO) for each ISCCP weather state from 1984-2007 169

C-3 Mean histograms of simulated cloud-top pressure and optical thickness corresponding to the observed ISCCP weather states (July 1983-June 2008) using MERRA data and a maximum (convective) and random (large-scale) cloud overlap parameterization 170

C-4 Same as Fig. C-3, but using a random (convective and large-scale) vertical cloud overlap parameterization 171

C-5 Cloud fraction trends for each p_c-τ bin for the entire 25-yr simulation using a maximum-random vertical cloud overlap parameterization 172

C-6 Same as Fig. C-5, but for the random vertical cloud overlap parameterization 173

FIGURE Page

C-7 Composite pressure vertical velocity profiles (hPa day^{-1}) from MERRA data corresponding to each of the observed ISCCP weather states 174

C-8 Composite soundings from MERRA data corresponding to each of the observed ISCCP weather states 175

D-1 Annual average, zonal mean meridional mass streamfunction for the reanalysis ensemble from 1984-2007 178

D-2 Annual average, relative frequency of occurrence (RFO) for each of the ISCCP cloudy weather states from 1984-2007 179

D-3 Regime-average profiles of the daily average, total diabatic heating (Q_1) for each of the eight ISCCP cloudy weather states 180

D-4 Differences in the frequency of occurrence for each weather state corresponding to the times of HC extremes (strong-weak) for the northern hemispheric (dominant, winter) cell during DJF 1983-2008 181

D-5 Same as Fig. D-4, but for the southern hemispheric (dominant, winter) cell during JJA 1984-2007 182

D-6 Same as Fig. D-4, but for the northern hemispheric (weak, summer) cell during JJA 1984-2007 183

D-7 Average differences in the ISCCP-derived total heating corresponding to the HC extremes (strong-weak) for the winter hemisphere cell during the 1983-2008 period for the (a) northern hemisphere in DJF and (b) southern hemisphere in JJA 184

D-8 Same as Fig. D-7, but for the summer hemisphere cells 185

D-9 Same as Fig. D-1, but for the (a) CAM4-CTRL and (b) ISCCP-CTRL cases 186

D-10 Time series of the annual average (a) maximum and (b) minimum meridional mass streamfunction values from the CAM4-CTRL and ISCCP-CTRL simulations for the northern (Ψ_N^*) and southern hemispheric (Ψ_S^*) cells during 1984-2007, respectively 187

FIGURE Page

D-11 Same as Fig. D-10, but for the (a) level of maximum overturning for the southern hemispheric cell and (b) HC domain average precipitation.....188

LIST OF TABLES

TABLE		Page
A-1	Reanalysis datasets used in this study	138
A-2	Annual average values of Ψ_N^*, Ψ_S^*, p_N^*, p_S^*, and $\Delta\varphi$ for each reanalysis during the 1979-2008 period	139
A-3	Yearly trends of annual average quantities from each reanalysis dataset for the 1979-2008 (1958-2008) period.	140
A-4	Mean values and number of occurrences of Ψ_N^* for the 1979-2008 period for each reanalysis categorized by ENSO phase during DJF	141
A-5	Same as Table A-4, but for Ψ_S^* during JJA	142
A-6	Same as Table A-4, but for the annual average $\Delta\varphi$	143
B-1	Heating data and field campaigns used in this study	153
B-2	Number of samples for each project domain categorized by weather state	154
C-1	Cluster Cloud Fraction (CCF) for each weather state from the ISCCP observations and MERRA simulations using a maximum-random and random vertical cloud overlap parameterization	167
D-1	Trends in annual average quantities from the CAM4 simulations, reanalysis ensemble, and GPCP data for the 1984-2007 period.	177

CHAPTER I

INTRODUCTION

Differences in the solar zenith angle and length of day lead to an excess of shortwave radiation buildup at low-latitudes compared to other parts of the globe. The resultant non-uniform heating creates a strong meridional temperature gradient and is the principle driving force behind the atmospheric general circulation. Warm, moist air parcels that rise in the tropics reach the tropopause and stable layer and eventually diverge poleward in each hemisphere in order to accomplish the redistribution of low-latitude heat energy and moisture. The air begins to cool and converge as it moves outward from the equator, eventually sinking over a broad area usually located between 20°-30° latitude in each hemisphere. A return flow at low-levels brings cooler, drier air into the deep tropics and the subsequent circulation is known as the Hadley cell. The Hadley circulation (HC) is responsible for a significant amount of the meridional overturning in the tropical and subtropical atmosphere (streamfunction values often peak in excess of 1×10^{11} kg s^{-1}) and is important for determining both local weather and climate.

Recent studies have suggested that the intensity and width of the HC has changed over the past few decades, with a corresponding poleward increase in the latitude of the dry zones and subtropical jets with evidence of stronger meridional overturning (e.g., Chen et al. 2002; Mitas and Clement 2005; Fu et al. 2006; Hu and Fu 2007; Seidel and Randel 2007; Birner 2010). Despite a growing body of work, long-term climate trends

concerning HC intensity and width demonstrate significant variability between different types of datasets (i.e., general circulation models, reanalyses, and observations of global winds, tropical ozone concentrations, and tropopause heights, among others) and often disagree on the sign of the apparent intensification and widening. Furthermore, there is no uniform consensus as to expected HC changes in response to global warming. Many of the Intergovernmental Panel on Climate Change (IPCC) Fourth Assessment Report (AR4) models predict a weakening of the tropical circulation by the year 2100 in response to global climate change (e.g., Lu et al. 2007, 2008), despite the suggested intensification throughout recent decades. As such, it remains unknown how HC changes and extremes might influence tropical and subtropical precipitation patterns in future climates.

Global precipitation is suppressed in the subtropics due to the large-scale subsidence associated with the HC, yet the impacts of a weakened Hadley cell (and corresponding descending branch) upon precipitation in this region have not been investigated. Would precipitation be more likely to form in these regions in future climates given the weaker subsidence? Is it possible for semi-arid regions to develop rainy seasons if there are significant diabatic feedbacks that exist along with the potential increase in subtropical cloud systems? Finally, would these responses be identified in the global precipitation patterns or remain confined to regional scales because of local modifications to the HC? Previous work has suggested potential mechanisms for regional changes in the meridional circulation such as considering the effects black carbon and soot aerosols over India and southern China (Menon et al. 2002), though

these feedbacks remain less well understood. Nevertheless, it remains necessary to first obtain a better understanding of the HC in the present day before assessing predictions of HC activity in future and modified climates.

This dissertation presents a series of work related to the representation of the HC in atmospheric reanalyses and general circulation models (GCMs) with connections to the underlying tropical and subtropical cloud systems that comprise the mean meridional circulation. Each chapter is meant to be an independent study and the greater collection will thus contain occasional overlap in the individual descriptions of data and methods. Appropriate references to important results from earlier chapters are made throughout the text and a synthesis and brief discussion is provided at the end of the document.

Given the wide array of HC variability diagnosed with GCMs, observations, and reanalysis, we first evaluate an ensemble of eight atmospheric reanalyses in order to examine the HC climatology, interannual variability, and long-term trends present in many of the newest products and datasets that remain otherwise unevaluated in the tropics (Chapter II). Focus is then shifted towards long-term satellite observations of the cloud regimes that occur throughout the tropical and subtropical latitudes associated with the HC. The heating properties of different cloud regimes is investigated using matching upper-air sounding observations from 10 field campaigns over a range of tropical and subtropical locations (Chapter III). The ability of reanalyses to simulate the observed large-scale environmental conditions and implicit cloud properties is investigated in Chapter IV. The determination of which cloud regimes exhibit the greatest control on HC interannual variability is discussed in Chapter V, along with a comparison of the HC

in reanalyses, GCMs, and models simulations constrained by observations of atmospheric heating. Chapter VI closes the dissertation with a brief summary of results, synthesis, and suggestions for future work.

CHAPTER II

A COMPARISON OF THE HADLEY CIRCULATION IN MODERN REANALYSES*

1. Introduction

The global mean meridional circulation is traditionally divided into three zones comprising a thermally direct polar cell, thermally indirect Ferrel cell, driven by mid-latitude eddies, and a thermally forced cell at low latitudes. The last of these phenomena is commonly referred to as the Hadley circulation (HC, hereafter) and consists of an idealized zone of tropospheric ascent near the equator, poleward flow aloft, subsidence in the subtropics, and a return flow at low levels in each hemisphere. Deep convection in the tropics fuels the HC (e.g., Riehl and Malkus 1958; Riehl and Simpson 1979; Fierro et al. 2009) with the ascending branch following the seasonal migrations of the Intertropical Convergence Zone (ITCZ) and a broader, weaker area of descent usually located between 20°-30° latitude in each hemisphere. The HC accounts for the largest portion of global overturning in the meridional-vertical plane (streamfunction values often peak in excess of 1×10^{11} kg s^{-1}) and is responsible for a major redistribution of energy and heat from the equator to higher latitudes.

Researchers have long studied the HC given its importance in both determining local weather and climate (e.g., tropical rainfall patterns and suppression of precipitation in the subtropics) and influences on weather patterns at higher latitudes due to impacts

on the general circulation. Although the existence of the HC has been well documented for several centuries, questions remain as to how the HC has evolved over the period of record and how future global changes may affect the HC and resulting weather patterns/climate. Studies of the HC require global observations (e.g., satellites or other large-scale, upper-air arrays), numerical reanalyses, or atmospheric general circulation models (GCMs) given the comprehensive nature of the phenomenon.

Comparison of observational metrics, reanalyses, and GCMs often reveal large differences in the mean representation of the HC (e.g., Mitas and Clement 2005; Johanson and Fu 2009), with more significant discrepancies in the observed and forecast trends of HC activity throughout the twentieth (Hu and Fu 2007; Seidel and Randel 2007; Mantsis and Clement 2009) and twenty-first (Lu et al. 2008) centuries. Substantial variability may also exist in the products of those datasets considered alike, with HC trends derived from different reanalyses producing opposite results (e.g., Song and Zhang 2007). Furthermore, opinions differ on whether recent trends in increased equatorial rainfall and decreased subtropical humidity/cloudiness can be viewed as a strengthening of the tropical circulation (Chen et al. 2002; Fu et al. 2006; Sohn and Park 2010) or are better attributed to instrument error and data matching across multiple satellites or sampling during prolonged El Niño-Southern Oscillation (ENSO) periods (Trenberth 2002). The absence of a proper consensus regarding the observed fluctuations of the HC during the previous decades thereby makes verification of GCMs and reanalyses a difficult task.

Although there are numerous studies that compare precipitation and sea surface temperature (SST) from different reanalysis datasets (Quartly et al. 2007; Bosilovich et al. 2008; Ma et al. 2009; Higgins et al. 2010; etc.), few studies appear in the formal literature with a specific intercomparison of the tropical Hadley cell. Previous investigations were limited to a small number of datasets; at least eight global reanalyses are now available for study (Table A-1), often with increased resolution and improved model physics and data assimilation schemes relative to their earlier counterparts. Those recent studies using HC metrics derived from next-generation reanalyses (e.g., tropopause height statistics related to the HC width as in Birner 2010) find divergent trends amongst older and newer datasets. Discrepancy among HC trends from reanalyses studies (e.g., Mitas and Clement 2005; Hu and Fu 2007) and disagreement with observations and GCMs (Mitas and Clement 2006; Seidel and Randel 2007; Johanson and Fu 2009; among others) suggest the need for additional intercomparison studies using a multi-reanalysis ensemble to better elucidate decadal trends and potential biases.

While the HC demonstrates a well-known annual mode (e.g., Dima and Wallace 2003), the interannual variability is less well understood. Oort and Yienger (1996) were among the first to investigate the correlation between SSTs in the eastern equatorial Pacific and the maximum (minimum) values of the meridional mass streamfunction in the northern (southern) hemisphere. Oort and Yienger (1996) found that the absolute value of the streamfunction anomaly was generally maximized during warm ENSO events, with weakening usually observed during La Niña years. Studies since continue to attribute a large portion of the HC interannual variability to ocean-atmospheric

perturbations induced by ENSO cycles (Quan et al. 2004; Ma and Li 2008; etc.), while others find significant non-ENSO variability (e.g., Caballero 2007).

Additional considerations related to HC intensity may include changes to the oceanic mean state with warming in the tropical Indian and western Pacific oceans (Quan et al. 2004), links to monsoon activity (Trenberth et al. 2000; Dima and Wallace 2003), and the influence of subtropical stability and midlatitude baroclinic eddy stresses on the descending branch of the HC (Held 2000; Walker and Schneider 2006; Caballero 2007; Frierson et al. 2007; Lu et al. 2007; Korty and Schneider 2008; Lu et al. 2008; among others). Moreover, Johanson and Fu (2009) were unable to reproduce the observed trends in HC width (e.g., Hu and Fu 2007) when using GCMs forced with prescribed SSTs, concluding that there must be some other influence for HC width beyond SST alone. Examination of a multi-reanalysis ensemble provides the opportunity to identify whether SST anomalies associated with a particular ENSO phase (using prescribed or predicted SSTs) are able to sufficiently explain HC variability in reanalyses or determine if other controlling factors are present in these datasets.

2. Data and Methods

a. Reanalysis Data

As identified in the previous section, atmospheric reanalyses are used herein to examine the structure and properties of the large-scale circulation. Multiple reanalysis datasets have become publically available over the last few years and eight reanalyses (comprising both older and more recent datasets) were identified for the purposes of this

study (Table A-1). Selected reanalyses include the Japan Meteorological Agency (JMA) 25-year Reanalysis Project (JRA; Onogi et al. 2007), the European Centre for Medium-Range Weather Forecasts (ECMWF) Interim Reanalysis (ERAINT; Dee and Uppala 2009), the ECMWF 40-year Reanalysis (ERA40; Uppala et al. 2005), the National Centers for Environmental Prediction-National Center for Atmospheric Research (NCEP/NCAR) 40-year Reanalysis Project (NNRP; Kalnay et al. 1996), the National Centers for Environmental Prediction-Department of Energy (NCEP/DOE) Reanalysis Project (NDRP; Kanamitsu et al. 2002), the National Centers for Environmental Prediction (NCEP) Climate Forecast System Reanalysis (CFSR; Saha et al. 2010), the National Aeronautics and Space Administration (NASA) Modern-Era Retrospective Analysis for Research and Applications (MERRA; Rienecker et al. 2011), and the National Oceanic and Atmospheric Administration-Cooperative Institute for Research in Environmental Sciences (NOAA/CIRES) Twentieth Century Reanalysis Version 2 (20CR; Compo et al. 2011).

Whereas each reanalysis was developed to meet specific goals with distinct model physics and resolutions, nearly all of the reanalyses ingest a variety of surface, upper-air, and satellite observations (when available) using either a 3-D or 4-D variational assimilation technique. The 20CR does not include any upper-air or satellite observations, however, and only assimilates surface pressure, SSTs, and sea ice coverage using an ensemble Kalman filter. Several of the newest reanalyses contain adaptive schemes for changing concentrations of atmospheric aerosols, CO_2, and other trace gases and may thus be useful in discovering multi-decadal HC trends in the recent climate. All

of the reanalyses are forced with specified SSTs with the notable exception of the CFSR, which is a fully-coupled land-ocean-atmosphere reanalysis. Other technical details related to the differences in the reanalysis frameworks can be found in the references above.

As a first-order approach to eliminate resolution dependency in the reanalysis solutions, all relevant surface and upper-air variables were regridded to a common horizontal fixed grid of 2.5° x 2.5° using either spherical harmonics or bilinear interpolation. Upper-air variables were also regridded in the vertical with a common 10 hPa pressure increment (ranging from 1000 – 10 hPa) using linear interpolation. Unphysical solutions resulting from the interpolation (e.g., negative precipitation rates) were corrected by specifying appropriate upper and lower boundaries for each affected variable. Additional tests were performed to document the sensitivity of selected variables to interpolation functions and the mean variable quantities (and to a lesser extent, maximum and minimum values) only changed by a small amount. Monthly averages (if not already available) were calculated for all variables.

The meridional stream function, Ψ, satisfying the zonal mean continuity equation in spherical coordinates can be calculated at each pressure, p, and latitude, φ, as a function of the downward integrated meridional wind, v, and is expressed as

$$\Psi(p,\varphi) = \frac{2\pi a \cos(\varphi)}{g} \int_{p}^{p_s} [v(p,\varphi)] dp \,, \quad \text{(II-1)}$$

where a is the planetary radius, g is the gravitational acceleration, and bracketed terms denote a zonal average. Using this notation, v is by definition positive (i.e., northward) in

regions where $\frac{\partial \Psi}{\partial p} > 0$. Streamfunction values are set to zero at the top of the atmosphere, and the lowest level is modified such that Ψ equals zero at the lower boundary to ensure mass conservation and a steady-state solution to the continuity equation.

Several quantities of interest were determined from the latitude-pressure cross-sections of Ψ. The maximum streamfunction value centered in the northern hemisphere, Ψ_N^*, is a common index to measure the overturning strength (e.g., Oort and Yienger 1996; Quan et al. 2004; Caballero 2007) and corresponds to a critical pressure and latitude, p_N^* and φ_N^*, respectively. Similar coordinates (p_S^* and φ_S^*) can be defined for the minimum streamfunction value, Ψ_S^*, in the southern hemisphere. Streamfunction maxima/minima were limited to coordinates above 800 hPa to avoid contamination by low-level features near the cell edges. The subtropical HC termini, φ_N and φ_S, are defined as the first latitudes poleward of the cell centers (φ_N^* and φ_S^*) in which the 700-400 hPa average value of Ψ equals zero in each hemisphere, using linear interpolation. Previous studies have used either the value of Ψ at 500 hPa (Frierson et al. 2007; Lu et al. 2007, 2008) or the 600-400 hPa average (Hu and Fu 2007; Johanson and Fu 2009); the width results are generally not sensitive to using either a single level or a vertical average (e.g., Johanson and Fu 2009). Finally, the HC width ($\Delta\varphi$) can be determined as the difference between φ_N and φ_S. These metrics were calculated for each dataset, in addition to those retrieved from an equally-weighted ensemble average of the zonally

averaged meridional streamfunction (rather than a simple arithmetic mean) using all the reanalyses available at any given time.

b. Other Data

Monthly average precipitation estimates were taken from the Global Precipitation Climatology Project (GPCP) dataset, Version 2.1 (Adler et al. 2003). The GPCP data combines numerous precipitation measurements from satellite observations (low-earth orbiting microwave radiances, IR values from geostationary sensors, etc.) with surface rain gauge observations to create a blended multisource precipitation estimate on a global grid that is independent of any numerical models or physical parameterizations. Monthly precipitation data is available at a 2.5° x 2.5° horizontal resolution and was interpolated to match the coordinates of the reanalysis products used in this study.

Finally, the Climate Prediction Center (CPC) Oceanic Niño Index (ONI) is used as a source of SST anomalies and identification of ENSO phase. The ONI classifies an event as El Niño (La Niña) if the average SST anomaly in the Niño 3.4 region (5°N-5°S, 120°-170°W) is +0.5 °C (-0.5 °C) during a three month running average for at least five consecutive months, compared to the 1971-2000 base period. The CPC ONI uses the NOAA Extended Reconstructed SST (ERSST) version 2 dataset, details of which can be found in Smith and Reynolds (2004). The ENSO classifications for individual months were extended to seasonal or yearly periods if more than half of the months comprising the period of interest were identified as a particular ENSO phase.

3. Results

The following analysis presents an intercomparison of reanalyses for January 1979 – December 2008. The majority of the reanalyses are limited to the satellite era (most datasets begin at or after 1979; Table A-1), with only three datasets (ERA40, NNRP, and 20CR) initiating prior to the satellite epoch. Some discussion is included regarding the long-term trends (1958-2008) in these reanalyses.

a. HC Climatology and Ensemble Variability

The annual average, zonal mean meridional mass streamfunction for each reanalysis dataset is shown in Fig. A-1. All of the reanalyses reveal the expected structure of a roughly symmetric two-cell pattern with the mutual ascending branch located slightly north of the equator, in agreement with the annual average position of the ITCZ. The corresponding circulations for JJA and DJF are shown in Figs. A-2 and A-3, respectively; the MAM and SON streamfunction values are similar to the annual average. Each dataset demonstrates a transition towards a dominant one-cell pattern with ascent in the summer hemisphere and descent in the winter hemisphere during the solsticial seasons, as previously identified in reanalyses (e.g., Dima and Wallace 2003) and observations (e.g., Oort and Rasmusson 1970).

Though the solutions appear similar, notable differences exist among the reanalysis ensemble. Low-level (below 800 hPa) eddies appear in the subtropics for all datasets, with the exception of the ERA40. Despite having identical native vertical resolution and data output on similar pressure levels as the next-generation ECMWF

reanalysis (ERAINT), the subtropical eddy feature is absent from the ERA40 solutions during all seasons and for the annual average. The 20CR data has a poleward displacement of the $\Psi = 0$ boundary throughout the 1000-600 hPa layer which is not seen in the annual average for the other reanalyses (Fig. A-1h). The 20CR boundary anomalies are more pronounced for the southern hemispheric cell during JJA (Fig. A-2h) than the northern cell in DJF (Fig. A-3h). These edge effects are likely attributed to the difference in the data assimilation strategy between the 20CR and the remaining reanalyses; the 20CR does not assimilate upper-air or satellite data and thus should be more error prone in the southern hemisphere where the number of observations over land is greatly reduced. Finally, the NNRP meridional overturning is significantly weaker than the remaining datasets, particularly for the southern hemispheric cell during the boreal summer (Fig. A-2d).

The multi-reanalysis ensemble average streamfunction for the annual average HC is shown in Fig. A-4. With the exception of the previously identified edge effects, the ensemble average (ENS, hereafter) is most similar in both magnitude and structure to the 20CR. Whereas the 20CR data may not be expected to verify for individual events (given the reduced number of available observations used in the data assimilation scheme), the ability to best simulate the ENS streamfunction potentially justifies its use in tropical and subtropical climate studies.

The annual mean streamfunction values, level of maximum overturning, and HC width for each dataset are listed in Table A-2. The annual average ENS streamfunction has a long-term mean of 10.46×10^{10} kg s^{-1} and -13.10×10^{10} kg s^{-1} for the northern and

southern hemispheric cells, respectively. These values are smaller in magnitude than the arithmetic mean of the individual members because the ENS quantities are derived from the equally-weighted, zonally averaged meridional streamfunction, which accounts for differences in the vertical structure among datasets. The individual values of Ψ_N^* range from 9.39 x 10^{10} kg s^{-1} (NNRP) to 12.84 x 10^{10} kg s^{-1} (ERA40), while the corresponding values of Ψ_S^* vary from -10.38 x 10^{10} kg s^{-1} (NNRP) to -15.45 x 10^{10} kg s^{-1} (CFSR), indicating an ensemble variability of 33.2% and 38.7% for the northern and southern cells relative to the ENS mean. The ensemble variability is amplified (e.g., in excess of 40%) during the solsticial seasons with larger percent differences relative to the ensemble mean (not shown). The ERA40 has the strongest overturning for the northern cell, while the MERRA and NNRP contain the weakest circulations. The ERA40 is again amongst the strongest circulations for the southern hemisphere, with the CFSR producing similarly large values. The NNRP is a more obvious weak outlier for the southern cell.

The climatological ensemble variability in HC streamfunction magnitude is corroborated by the annual average, zonal mean total precipitation rate produced by each reanalysis (Fig. A-5). All of the datasets overpredict the average total precipitation rate relative to GPCP throughout the entire tropics and most of the subtropics with the most significant differences centered near 7.5° N and 5° S. Zonal mean precipitation rates along the ITCZ vary from 5.7 mm day^{-1} (NNRP) to 8.9 mm day^{-1} (ERA40). The ERA40 produces the most tropical precipitation, whereas the MERRA and NNRP have the least rainfall, in agreement with those datasets identified in the previous analysis containing

the largest and smallest streamfunction values. Although the coupled reanalysis (CFSR) produces the strongest annual average Ψ_S^*, it falls in the middle to lower portion of the distribution for tropical rainfall and resides in the upper portion for subtropical precipitation rates. The CFSR also overpredicts precipitation in excess of 2.0 mm day^{-1} (relative to GPCP) along the tropical peak, despite previous work indicating that the CFSR is more skilled than former NCEP reanalyses in the mid-latitudes (e.g., Higgins et al. 2010).

Table A-2 also shows that the JRA and NNRP have higher circulation centers, p_N^* *and* p_S^*, than the remaining reanalyses. Although the total amount of dry air mass in the HC is identical for similar values of the streamfunction regardless of the central pressure level, the height of the circulation center could have significant effects upon the resulting estimates of cross-equatorial water vapor transport, as done for the NNRP in Cohen et al. (2000) and Sohn and Park (2010). Whereas a higher circulation center may be explained by the presence of more organized convection and elevated latent heat release, it is not possible to determine these properties from the reanalyses. A common region of anomalous northward velocities (~1.5-2.0 m s^{-1}) was identified for the JRA and CFSR during JJA and for the annual average (not shown), located across much of the eastern equatorial Pacific at 400 hPa. The northward anomalies contribute to a weakening of the zonally averaged mass flux and streamfunction values at these heights and higher circulation centers in these datasets (although the circulation center for the CFSR is within reasonable agreement of the remaining datasets, it experiences a local minimum at ~450 hPa during JJA; Fig. A 2f). A similar region (and similar magnitude)

of northward anomalies was present in the NNRP data at 700 hPa, resulting in weaker low-level overturning and a higher circulation center. A common region of anomalous southward velocities was not identified for the northern cell during DJF, however, and further investigation is necessary to identify the root causes of the anomalous meridional winds.

The annual average HC width (Table A-2) has a long-term ENS average of 65.3°, varying from 62.4° (CFSR) to 67.5° (JRA). The range of the width estimates is 7.8% relative to the ensemble mean, which is significantly smaller than the relative ensemble spread for HC intensity. Curiously, there is no direct correspondence between intensity and width in the reanalysis datasets. The JRA (a relatively strong HC) might be expected to have the narrowest circulation based upon conservation of mass; the MERRA (a relatively weak HC) might likewise have a larger width. The JRA has the widest circulation of all the reanalyses, however, with the MERRA producing a relatively narrow HC. Clearly, HC intensity in the reanalyses is controlled by factors other than the width alone.

b. Trends in HC Intensity and Width

Time series of the annual average HC intensity (Ψ_N^* and Ψ_S^*) and width ($\Delta\varphi$) are shown for each reanalysis dataset and the ensemble average in Figs. A-6 and A-7. Trends of the regression lines fit to the annual average quantities from 1979-2008 for each of the above variables are documented in Table A-3. Longer trend values for 1958-2008 are shown when available. All of the reanalyses show a strengthening of the

northern cell with time (Fig. A-6a), with significant trends at 95% ranging from 0.37 x 10^{10} kg s^{-1} $decade^{-1}$ to 1.43 x 10^{10} kg s^{-1} $decade^{-1}$ (Table A-3). Three of the reanalyses (ERAINT, NDRP, and 20CR) show weak and non-significant trends. The intensification trends for the ERA40 and NNRP during 1958-2008 are somewhat smaller than those for 1979-2008, suggesting a more rapid intensification during the later period. The 20CR, which should minimize any artificial long-term trends potentially introduced by the evolution and assimilation of different satellite datastreams, demonstrates a weak (though statistically significant) intensification rate of 0.09 x 10^{10} kg s^{-1} $decade^{-1}$ for 1958-2008, noticeably smaller than estimates from the previous datasets. All of the reanalyses demonstrate larger intensification trends during the DJF season (with the exception of the NDRP), with the ERA40 as high as 2.68 x 10^{10} kg s^{-1} $decade^{-1}$ (not shown). Overall, the decadal trends of all the reanalyses fall within the range documented in previous research. Mitas and Clement (2005) found significant intensification in the ERA40 and NNRP, no significant trend with the NDRP (or reconstructed atmospheres from global radiosonde networks), and only a slight increase with GCMs, consistent with the estimates above.

Fig. A-6b shows more variations in trends for Ψ_S^*. Table A-3 indicates that only three reanalyses have a statistically significant intensification of the southern hemispheric cell from 1979-2008 (i.e., ERA40, NNRP, and MERRA). The JRA and CFSR illustrate a statistically significant weakening trend, with a more pronounced weakening of 1.69 x 10^{10} kg s^{-1} $decade^{-1}$ and 1.30 x 10^{10} kg s^{-1} $decade^{-1}$ during JJA (not shown). These two reanalyses employ chemical models for ozone production (in

addition to the 20CR, which has a weak strengthening of the southern cell that is not statistically significant) instead of using directly assimilated observations or climatological profiles, suggesting that the different representation of stratospheric ozone (and associated radiative and dynamic feedbacks) may play a role in HC trends. Polvani and Kushner (2002) showed that polar stratospheric cooling (a consequence of long-term ozone reduction in the southern hemisphere) may significantly alter the meridional temperature gradient, with a resulting poleward displacement of the upper-tropospheric jets and widening (and weakening) of the tropical circulation. The NDRP and MERRA also indicate a statistically significant weakening trend in excess of 0.50 x 10^{10} kg s^{-1} $decade^{-1}$ during JJA (not shown). These results cast doubt on the actual qualitative trends (i.e., strengthening or weakening) of the southern hemispheric cell during this period. The ERA40 and NNRP demonstrate much smaller intensification rates for the 1958-2008 period, suggesting again a more rapid intensification during recent decades. The corresponding 20CR long-term trend indicates only a slight (though statistically significant) intensification.

Trends in the HC width, $\Delta\varphi$, are shown in Fig. A-7 and indicate a general widening with time of the annual average HC. Five of the reanalyses suggest a statistically significant widening (Table A-3). The widening trends for 1979-2008 (significant values ranging from 0.78° $decade^{-1}$ to 1.48° $decade^{-1}$) are broadly consistent with those determined by Hu and Fu (2007) for the ERA40, NNRP, and NDRP of ~1.1° $decade^{-1}$ over the 1979-2002/2005 period. The long-term trend (1958-2008) for the NNRP is similar, while the 20CR exhibits a more modest rate of cell expansion. The

ERA40 actually suggests a weak narrowing during the 1958-2008 period, casting some doubt on the certainty of the long-term trends. Moreover, the amplitude of the annual average widening for the ERA40 during 1979-2008 is also smaller than previously reported (0.41° decade^{-1}, not statistically significant). The trend becomes slightly more comparable to Hu and Fu (2007) when using their criteria for HC width (averaging the streamfunction throughout the 600-400 hPa layer in place of the 700-400 hPa as done here), producing a statistically significant widening of 0.54° decade^{-1}. Differences in the exact values of the ERA40 widening trends might arise from the use of different data resolutions and the regridding methods described in section 2, though these hypotheses require further investigation.

Comparison of the HC trends reveals no clear relationship between intensity and width. The JRA, which has the second largest intensification rate for the annual average Ψ_N^*, also has the greatest widening trend (Table A-3). Consequently, there is no simple correspondence of either mean state intensity and width or related HC trends (i.e., conservation of mass alone would predict a narrowing trend with HC intensification) in some of the reanalysis datasets. Finally, it is worth noting that although the range in estimates of the HC width increase among the reanalysis ensemble during the second half of the 1979-2008 period (Fig. A-7), five of the reanalyses converge near the ENS value by 2008. The increase in ensemble variability is therefore attributed to just a few datasets which become more pronounced outliers near the end of the period.

c. Interannual Variability and Connections to ENSO

As previously identified, it remains a topic of debate as to how ocean-atmospheric interactions might modulate the long-term and interannual variability of the HC through connections with ENSO anomalies. Although Oort and Yienger (1996) found a significant correlation between their time series of HC streamfunction and eastern equatorial Pacific SST, equal amplitude SST perturbations did not generate equal streamfunction anomalies and several points appear anti-correlated in their data, suggesting something other than ENSO must be contributing to the variability on yearly time scales. Caballero (2007) found that non-ENSO variability accounted for more than 70% of the detrended streamfunction variance in the ERA40, with the increased cell strength balanced by greater extratropical wave fluxes impinging upon the tropics. The subtropical jets are thought to shift equatorward in response to an increased eddy stress, resulting in a narrower and thus more intense (given the constraint of mass conservation) overturning circulation.

To better determine the contributions to interannual HC intensity, yearly and seasonally averaged values were calculated for Ψ_N^* and Ψ_S^* with the long-term trend removed and further categorized by ENSO phase (either as a warm, neutral, or cold event) for each dataset using the ONI (see section 2b). The interannual variability among the detrended datasets (defined as the difference of the streamfunction value for the maximum and minimum seasons divided by the long-term average) before ENSO subsetting ranged from 21% – 29% (ENS value of 27%) for the northern cell during DJF, with the notable exception of the ERA40. The ERA40 contained anomalously large

values of Ψ_N^* during strong overturning events, with a corresponding interannual variability of 43% relative to the dataset mean. Interannual variability estimates for the southern cell during JJA ranged from 16% – 27% (ENS 12%).

Detrended streamfunction values are shown for the northern hemispheric cell during DJF in Fig. A-8 (i.e., when ENSO is most active), with each ENSO phase color coded. The corresponding sample means for each phase are summarized in Table A- 4. Overall, the distributions show a weak clustering of the streamfunction values by ENSO phase for the northern (winter) cell, with El Niño events generally accounting for most of the occurrences above the 75th percentile and neutral and La Niña events representing weaker streamfunction values. Although the variances for individual ENSO categories may occasionally be large and contain overlap with other phases, a simple t-test statistic revealed that the sample means were almost always significantly different (at 95%) for warm-neutral and/or warm-cold comparisons during DJF for most reanalyses (Table A-4). The separation between neutral and cold events was more ambiguous, however, as substantial overlap in the distributions resulted in only one of the reanalyses (ERAINT) being able to identify a statistically significant difference in the sample means for the northern cell. Similar significance patterns were identified for a special long-term (1958-2008) dataset (ENS50), comprising streamfunction values (and corresponding ENSO classifications) from an equally-weighted, restricted ensemble average containing only those datasets with extended coverage (ERA40, NNRP, and 20CR). Considerable overlap exists for those ENSO neutral and La Niña events in the ENS50 dataset (Fig. A-8), with identical phase means (18.30×10^{10} kg s^{-1}, Table A-4). A larger sample size is

therefore considered not necessary in order to sufficiently determine statistical significance in the remaining datasets.

The ENSO clustering for the southern (winter) cell during JJA is less evident than the corresponding northern hemisphere winter cell (cf., Tables A-4 and A-5). Only four of the reanalyses indicate a statistically significant difference in the mean values of Ψ_S^* for warm-neutral and/or warm-cold conditions; all eight datasets demonstrated an ENSO dependency for Ψ_N^* during the local hemispheric winter. Furthermore, the long-term ensemble average (ENS50) contains no statistically significant values (Table A-5).

Although the average ENSO SST anomalies are generally weaker in JJA than those observed during DJF, the different behavior between the northern and southern winter cells may be partially controlled by stratospheric ozone. Recent studies have suggested variability on interannual timescales linking ENSO and polar stratospheric temperatures in the southern hemisphere (Hitchman and Rogal 2010; Hurwitz et al. 2011). Polar stratospheric temperatures are generally warmer during El Niño events, resulting in a weaker polar vortex. The relaxation of the meridional temperature gradient results in a reduced jet intensity and a presumably more narrow (and thus stronger) HC given the absence of any significant poleward jet contraction. The polar stratospheric feedbacks on HC intensity are thus the same sign as the expected ENSO effects inside the tropics, suggesting the overturning values should be more significant (i.e., compensating for the weaker SST anomalies during JJA) when categorized by ENSO phase. Those reanalyses using a chemical model and include ozone radiative feedbacks (JRA, CFSR, and 20CR) demonstrate a statistically significant difference for Ψ_S^* for

warm-neutral or warm-cold comparisons during JJA, suggesting these reanalyses contain the appropriate polar stratospheric feedbacks on HC intensity and width. Those reanalyses using directly assimilated observations or indirect climatological ozone profiles may have different levels of ozone forcing and stratospheric temperature response (e.g., the ERAINT and ERA40 datasets may overestimate polar stratospheric ozone in winter by up to 40%; Dragani 2011), thereby limiting the ability of some reanalyses to identify unique ENSO phase means for the southern hemisphere winter cell.

The sensitivity to ENSO phase is nearly non-existent during DJF or JJA for the corresponding summer hemisphere cells, with ENSO neutral or La Niña seasons responsible for the strongest overturning event in each the JRA, NNRP, NDRP, and CFSR datasets for the southern cell (not shown). Consequently, only a few of the mean values for a given phase demonstrate a statistically significant difference, telltale that other mechanisms beyond tropical SSTs must be in control of the interannual variability for the summer cell in the reanalysis datasets.

Statistics regarding the detrended annual average HC width and ENSO phase are presented in Table A-6. Whereas the width distributions display a similar weak ENSO phase clustering with occasional overlap (not shown) analogous to Ψ_N^* in DJF, half of the reanalyses (including the ENS) show a statistically significant difference for warm/neutral and cold events, irrespective of an overall small sample size. El Niño events account for the narrowest average HC, with La Niña years generally corresponding to the widest circulations. For example, values for the CFSR were 62.0°

and 63.6° for warm and cold ENSO conditions, respectively, consistent with the expectations of Seager et al. (2003). A smaller range was observed for the estimates of interannual variability, with HC width varying from 5% – 11% (ENS 7%) among datasets.

While the above results (i.e., narrower circulations during El Niño and wider cells during La Niña) are generally true for longer time periods, almost none of the reanalyses demonstrate a statistically significant difference from the other ENSO phase means for individual seasons (not shown). While the width calculations are often noisy during the solsticial seasons due to fluctuations in the poleward terminus of the summer (and weak amplitude) cell, similar null results were obtained during MAM and SON when the width retrievals become more stable. Calculations using the width of the individual cells (in place of the entire tropical width, $\Delta\varphi$) demonstrated some ENSO dependence, but not to the degree of significance identified for the cell intensities on seasonal time-scales (e.g., DJF, Table A-4). As such, it is possible that different mechanisms (and time scales) affect the HC intensity and width. At the onset of a warm ENSO event, the circulation intensity may increase (particularly in the dominant cell) as a result of warmer boundary conditions driving an increase in near-equatorial clouds and precipitation while maintaining a similar HC width. The effects of the SST anomalies may propagate to the upper tropical troposphere with a maximum correlated response lagging by 1-2 seasons (e.g., Newell and Weare 1976; Pan and Oort 1983; Yulaeva and Wallace 1994). These anomalies eventually alter the meridional temperature gradient and contract the subtropical jets (as outlined in Seager et al. 2003), resulting in a

narrower tropical circulation. The long-term narrowing (in response to SSTs) would eventually result in an additional intensification of the HC, attributed to conservation of mass, separate from the initial strengthening owing to the amplified convective mass flux. The ENSO metric used in this study, nevertheless, requires the presence of a persistent SST anomaly for five months prior to the period being classified as an ENSO event, thereby perhaps allowing a sufficient time for the subtropical jets to contract and result in a narrower HC for the seasonal periods in question.

4. Summary and Discussion

Previous studies using observations and reanalyses suggest an intensification and poleward expansion of the tropical Hadley circulation throughout the twentieth century. Although the rates of intensification and expansion vary by study (or may occasionally be absent as in many GCMs), the climatological representation of the HC and decadal trends were previously undocumented for many of the newest reanalyses currently being produced by several meteorological centers worldwide.

Significant ensemble variability was found in the mean-state variables describing the HC intensity. Differences in the range of climatological mean values for the annual average meridional mass streamfunction among datasets was upwards of 33.2% and 38.7% of the mean ensemble average for the northern and southern cells, with higher relative differences observed for shorter (i.e., seasonal) periods. The ERA40, JRA, and CFSR produced the strongest meridional overturning, whereas the MERRA and NNRP were consistently the weakest. Mean state ensemble variability was consistent with the

zonal average total precipitation rate and mid-level vertical velocity amongst datasets. Although differences of a few degrees were identified in the reanalysis ensemble for the annual average tropical width, the range of ensemble variability was only 7.8% of the mean ENS width.

The NNRP, perhaps the most widely used atmospheric reanalysis, produced anomalously low streamfunction amplitudes for the southern hemispheric cell during JJA, in addition to the annual average. Moreover, the NNRP and JRA both produced a higher circulation center compared to other reanalyses, leading to possible biases in cross-equatorial vapor transport and other moisture quantities used to indirectly assess the strength of the tropical circulation in these datasets.

The 20CR best matched the multi-reanalysis ensemble average HC with the exception of a poleward shift in the low-level subtropical terminus, likely attributed to the differences in data assimilation and lack of land-based observations over the subtropics, particularly in the southern hemisphere. While the 20CR may not validate for individual events, it nevertheless produced a realistic HC structure and intensity similar to the average of seven other reanalyses, all which include countless more observations in their data assimilation (including upper-air and satellite data), thereby justifying its use in potential future tropical and subtropical climate studies. Long-term (1958-2008) trends in the 20CR dataset suggest a weak intensification (0.12×10^{10} kg s^{-1} $decade^{-1}$ average for both cells) and a modest widening ($0.62°$ $decade^{-1}$) of the tropical circulation, with slope values smaller than that of previous studies using reanalysis datasets (e.g., Mitas and Clement 2005; Hu and Fu 2007).

The latest reanalyses generally fall within the previous ensemble spread for mean state HC strength with larger uncertainty in the tropical width owing to a few outliers during the most recent years. Some discrepant trends emerged among newer datasets. The JRA and the CFSR both indicated a statistically significant weakening of the southern hemispheric cell, unlike the remainder of the reanalyses. The coupled reanalysis (CFSR) produced the smallest positive trend for HC widening in the annual average during the 1979-2008 period, though was not statistically significant. The JRA produced the strongest widening trend over the period of interest (~1.5° decade^{-1}), which was larger than previous trends using reanalysis data (Hu and Fu 2007) but smaller than those widening estimates derived from observations (e.g., Hudson et al. 2006; Seidel and Randel 2007). Furthermore, the sign of the widening trend is discrepant with Birner (2010), in which the JRA was the only dataset to suggest a narrowing of the HC when using tropical tropopause statistics derived from multiple reanalyses.

Large ranges were identified in the relative variability of HC intensity among the detrended datasets, with interannual variability estimates of 21% – 43% and 16% – 27% for the northern and southern hemispheric winter cells, respectively. Interannual variability of the annual average HC width varied from 5% – 11%. Previous HC interannual variability was thought to be highly influenced by ENSO cycles. Dynamical theories predicting the HC extent (and intensity) fall into two main categories: those that determine the tropical width as a function of 1) "interior" diabatic forcing under the assumption of upper-tropospheric angular momentum conservation (e.g., Held and Hou 1980), or 2) "exterior" forcing mechanisms including the role of momentum fluxes by

midlatitude baroclinic eddies (e.g., Held 2000) and subtropical stability (Frierson et al. 2007; Lu et al. 2007; Korty and Schneider 2008) or baroclinicity (Lu et al. 2008). Certain regions of the HC are thought to be better represented by different theories. The dominant cross-hemispheric winter cell may be more controlled by diabatic forcing whereas the weaker summer cell is likely highly influenced by eddies (e.g., Caballero 2007). Separation of the seasonally averaged streamfunction magnitudes by ENSO phase revealed a weak clustering and statistically significant difference between the mean values for El Niño and ENSO neutral or La Niña events in almost all the reanalysis for the winter cell intensity, with little difference for the summer cell. The reanalysis results give credence to the above ideas, suggesting that ENSO cycles and diabatic forcing from SST anomalies dominate the variability of the winter cell, whereas other factors must exert an important influence on the summer cell. Clustering by ENSO phase was less evident for the southern hemispheric winter cell during JJA and may be related to other physical mechanisms including stratospheric ozone. The statistical significance of ENSO phase was only identified for the annual average HC width, despite exerting a significant influence on the HC intensity at seasonal timescales. A potential explanation focusing on the response times of convective mass fluxes versus the contraction of the subtropical jet was provided in section 3, though this hypothesis requires more evaluation.

Although this research aims to provide an intercomparison of reanalysis solutions regarding the tropical Hadley circulation, it remains a topic of debate whether reanalysis data can be used to identify long-term dynamical and physical climate trends given the nature of discontinuous data assimilation and the uncertainty associated with analysis

fields prior to the age of global satellite coverage (e.g., Thorne and Vose 2010). While reanalysis data provides some information about modeled clouds (generally restricted to fractional cloud coverage over three discrete atmospheric layers), reanalysis itself does not explicitly predict cloud type. Future work will use reanalysis data to simulate observed cloud regimes/weather states, as sometimes done for GCM output (e.g., Zhang et al. 2005; Williams and Tselioudis 2007; Williams and Webb 2008). The ability (or lack thereof) to simulate specific cloud regimes among different reanalyses could be paramount to understanding differences in the mean state representation or long-term HC trends in the multi-reanalysis ensemble (e.g., Song and Zhang 2007).

CHAPTER III

TOTAL HEATING CHARACTERISTICS OF THE ISCCP TROPICAL AND SUBTROPICAL CLOUD REGIMES

1. Introduction

It is well known that clouds play an important role in controlling the daily weather, yet the aggregate effects and associated climate feedbacks of cloud systems remain less understood. These feedbacks are especially relevant in the tropics, where the total diabatic heating produced by clouds and precipitating systems directly couples these phenomena to the large-scale circulation. Variations in the magnitude and spatial distribution of heating from tropical cloud clusters elicit a different dynamical response in numerical models at both regional and global scales (e.g., Hartmann et al. 1984; Lin et al. 2004; Schumacher et al. 2004; Lappen and Schumacher 2012). Determining an accurate horizontal and vertical distribution of tropical heating is therefore paramount to better understanding and predicting climate variability in general circulation models (GCMs).

A large number of studies have focused on the calculation of apparent diabatic heating from cloud systems (comprising latent heating associated with phase changes of water, radiative processes, and eddy sensible heat fluxes) using data from intensive observation periods in tropical field campaigns (e.g., Yanai et al. 1973; Johnson 1976; Thompson et al. 1979; Lin and Johnson 1996; Zhang et al. 2001; Johnson et al. 2010). These studies typically rely on network measurements of temperature and wind across a

large-scale domain (on the order of 100,000 km^2) and are inherently restricted to the cloud characteristics of a specific region during periods of active sampling. Datasets including gridded model output (e.g., Nigam et al. 2000) and reanalyses (Sardeshmukh 1993), which are strongly influenced by cumulus parameterizations – a source of model infidelity, can be used for the above calculations, though the derivative profiles often contain significant variability among datasets and large heating differences compared to observations (e.g., Chan and Nigam 2009; Jiang et al. 2011). Other studies using direct measurements of cloud systems including precipitation radars (e.g., Houze 1982; 1989) and special ground-based radiation measurements (e.g., Li et al. 2013) are also limited to single points and may not be representative of the general cloud population across a larger domain.

Recent improvements in diabatic heating estimates from the Tropical Rainfall Measuring Mission (TRMM) satellite show significant promise for real-time, global monitoring (Tao et al. 2006; L'Ecuyer and McGarragh 2010). A number of algorithms use observations from the TRMM satellite (e.g., Tao et al. 2001; L'Ecuyer and Stephens 2003; Shige et al. 2004; Olson et al. 2006) along with reference profiles mostly derived from cloud-resolving models to estimate grid-averaged latent and radiative heating profiles across the tropics. These techniques, however, face certain limitations. First, they rely on model output as the basis of their look-up tables so include any model errors in their estimates. In addition, the retrievals struggle with areas of weak intensity clouds (including shallow convection and stratiform cloud) because of the footprint resolution and sensitivity of the satellite instruments. In particular, the redistribution of low-level

latent heating from nonprecipitating cumulus clouds and upper-level radiative heating associated with anvil cloud are both necessary components of the total heating in order to achieve a more realistic large-scale response in GCMs (e.g., Schumacher et al. 2004). TRMM heating has also been observed to be too weak compared to observations (Chan and Nigam 2009), although improvements have been made in this regard (Tao et al. 2010). Finally, the TRMM retrievals are limited in space and time resolution by the sampling of the satellite.

This study presents a method based solely on observations for determining the four-dimensional total diabatic heating field at up to 3-hr resolution by compositing profiles from numerous tropical and subtropical field campaigns and matching to cloud regimes or "weather states" (Jakob and Tselioudis 2003; Jakob et al. 2005; Rossow et al. 2005) from a 25-year subset of the International Satellite Cloud Climatology Project (ISCCP, Schiffer and Rossow 1983). The ISCCP weather states represent a statistical set of physically identifiable and recurring cloud mixtures over a large area (~280 km x 280 km) with populations ranging from large mesoscale convective systems (MCSs) to nonprecipitating, boundary layer cumulus. Previous studies have examined the latent and radiative heating characteristics of the ISCCP cloud regimes (Jakob et al. 2005; Jakob and Schumacher 2008; Oreopoulos and Rossow 2011; Li et al. 2013); this study is the first to investigate the total diabatic heating associated with each weather state. Compositing the diabatic heating profiles by ISCCP regime provides the added benefit of determining which mixture of cloud types has the greatest impact upon tropical variations in diabatic heating (i.e., the ability to identify what phenomena comprise the

mean heating), a subject that has received significantly less attention in the literature (e.g., Schumacher et al. 2008). Furthermore, many GCMs now include an ISCCP simulator (Klein and Jakob 1999) and the ability to diagnose unique heating profiles separated by cloud type provides a new observational metric for the verification of modeled clouds as sorted by regime (e.g., Webb et al. 2001; Williams and Webb 2009).

This study advances the idea proposed by Jakob et al. (2005) to extend point measurements of the ISCCP weather states to other regions of the globe based on average cloud properties and their relative frequency of occurrence. As such, we first determine average heating rates for the tropical and subtropical cloud regimes based on a large database of nearly 3000 sounding budget profiles from field campaigns and then evaluate the feasibility of reconstructing global heating patterns using this data. Section 2 describes the data and details of the compositing used in this study. The resulting heating profiles are presented in section 3, with a strong emphasis on the ensemble average in lieu of discussing individual field campaigns. Section 4 demonstrates two potential applications for studying tropical and subtropical clouds and precipitation using the heating reconstructions. Section 5 closes with a summary of key results and identifies avenues for continued work.

2. Data and Methods

a. ISCCP Weather States

The ISCCP D1 dataset (Rossow and Schiffer 1999) contains a global climatology of cloud properties (including cloud amount, cloud-top pressure, cloud optical thickness,

among others) derived from visible and infrared radiances observed by geostationary and polar-orbiting satellites. Jakob and Tselioudis (2003) and Rossow et al. (2005) supported the idea that the appearance of commonly recurring cloud regimes (also referred to as weather states) could be used as a proxy for multi-variate dynamical states of the tropical atmosphere. Studies since continue to link the ISCCP weather states to dynamical regimes and synoptic weather phenomena (e.g., Gordon and Norris 2010; Mekonnen and Rossow 2011) in addition to documenting longer-term variability of convectively active and suppressed regimes in the tropics (Tselioudis and Rossow 2011).

In short, the ISCCP weather states use a k-means clustering algorithm (Anderberg 1973) to identify repeating patterns of cloud height and extinction covariations over a large area (~280 km x 280 km) from individual satellite pixels of about 5 km in size. Joint histograms of cloud-top pressure and optical thickness are produced every three hours at each 2.5° x 2.5° gridpoint from July 1983 – June 2008 and sorted into a predefined number of groups (details provided in Rossow et al. 2005).

The subtropical extension of the ISCCP regimes identifies eight distinctive weather states (WS1-WS8) for all longitudes spanning the 35°N-35°S domain. The average centroids (i.e., mean histogram) for each cluster are shown in Fig. B-1. Shading represents the average frequency of occurrence for clouds falling into specific height and extinction bins within each regime. The integral across all bins or cluster cloud fraction (CCF) identifies the average total cloud cover for each cluster. Gridpoints may also be identified as a separate weather state if the entire field of view is clear (WS0) or data is flagged as missing (WS98). The corresponding relative frequency of occurrence (RFO)

for each regime (i.e., the number of counts for a particular weather state divided by the total number of counts for non-missing, daytime data) is listed at the top of each panel. Fig. B-2 shows the spatial distribution of the annual average RFO, along with markers identifying the center of the field campaign heating domains described in the following subsection, for each weather state.

Based on the average cloud properties and geographic distribution in Figs. B-1 and B-2, our interpretation of the weather states is as follows. WS1 comprises a population of tall, optically thick clouds primarily concentrated along the intertropical convergence zone (ITCZ). This weather state describes vigorous, deep convection with extensive cirrostratus and stratiform precipitation (near 100% CCF) normally associated with tropical MCSs. WS2 generally occurs in the same regions as WS1 and has a blend of tall, convective clouds with cirrus anvils of moderate optical thickness (cumulonimbus/cirrostratus). A mix of less vigorous convection and mid-level clouds (cumulonimbus/congestus) is apparent in WS3, though its RFO (17.6%) is significantly higher than WS1 and WS2 (5.9% and 8.3%, respectively). WS4 occurs over land and ocean domains, primarily containing thin cirrus with tall heights and low optical thickness. WS5 and WS6 represent moderately thick, low clouds principally found over the ocean, characteristic of marine boundary layer stratocumulus and stratus, respectively. These regimes have low RFOs (6.7% and 4.5%) and are typically restricted to areas of cold sea surface temperatures (SSTs) west of the continents. WS7 represents a transition state with low cloud tops and low to moderate optical thickness typical of broken stratocumulus and cumulus clouds (CCF of 59.7% compared to 84.7% and

74.5% for WS5 and WS6, respectively). WS7 occurs mainly over the oceans, yet has a stronger coastal influence than the previous two regimes. Finally, WS8 contains low cloud tops and small values of optical thickness (i.e., populations of mostly nonprecipitating cumulus) and has the largest domain average RFO of all the weather states (35.0%). WS8 also has significant cloud-free area (CCF of 24.1%) due to the expansiveness of this regime and its convective organization (e.g., cloud streets, open and closed cells).

It is worth repeating that the ISCCP weather states represent mixtures of clouds within the larger 2.5° x 2.5° area, hence the distribution of cloud properties shown in Fig. B-1. While the preceding classifications describe the predominant cloud type within the grid domain, there is likely overlap in the distributions between weather states (e.g., WS4 will contain low-level clouds and WS8 will include some cumulus congestus). Nevertheless, previous studies have shown that the ISCCP weather states have unique thermodynamic and precipitation characteristics (Jakob et al. 2005; Lee et al. 2013) in addition to different latent heating and radiative properties (Jakob and Schumacher 2008; Oreopoulos and Rossow 2011; Li et al. 2013). The total diabatic heating profiles should likewise vary significantly among regimes.

Finally, one caveat of the ISCCP weather states is that the classifications are only available during daytime hours when passive satellite instruments can determine visible optical thickness. A major goal of this work is the ability to reconstruct global diabatic heating fields for future studies of tropical climate dynamics (section 4), so we extend the first and last regime classifications for every day and gridpoint backward and

forward six hours, respectively. Jakob et al. (2005) showed that the tropical weather states have persistence on the order of a day. Furthermore, we note that the average six-hour persistence for individual regimes during daytime hours using the dates and locations of the field campaigns in this study is 47.6%. Persistence rates significantly increase when grouping weather states considered convectively active or suppressed (e.g., Tselioudis and Rossow 2011), and we find many instances in our data where the same regime is identified for a given field campaign uninterrupted for multiple days. Although this assumption may blur some of the results, the shapes of the individual composites tend to be mostly similar to those calculated using daytime-only data. As will be shown, the derived heating profiles have distinct differences among weather states, suggesting the persistence assumption remains effective for determining the relative heating contribution from each cloud regime.

b. Large-scale Budget Data

The presence of diabatic processes results in changes to the dry static energy, s, which is equal to the sum of the enthalpy and potential energy ($s = c_pT + gz$). The apparent heat source, Q_1, represents the net heating due to the ensemble of convection within a region (e.g., a sounding network) including a correlation term resulting from unresolved eddies. Yanai et al. (1973) defined the apparent heat source as follows:

$$Q_1 = \frac{\partial \bar{s}}{\partial t} + \overline{\nabla \cdot (s\mathbf{V})} + \frac{\partial (\bar{s}\bar{\omega})}{\partial p} \qquad \text{(III-1)}$$

$$= Q_R + L(c - e) - \frac{\partial (\overline{s'\omega'})}{\partial p} \qquad \text{(III-2)}$$

where Q_R is the radiative heating or cooling or the atmosphere, $L(c\text{-}e)$ is the contribution of latent heating or cooling from associated phase changes of water, and $\overline{s'\omega'}$ is the vertical transport of sensible heat by small-scale eddies. Overbar quantities represent horizontal means across the averaging area and primes indicate small-scale deviations. A similar equation can be written following moisture conservation. Yanai et al. (1973) define the apparent moisture sink, Q_2, as

$$Q_2 = -L\left(\frac{\partial \overline{q}}{\partial t} + \overline{\nabla \cdot (q\mathbf{V})} + \frac{\partial(\overline{q}\,\overline{\omega})}{\partial p}\right) \qquad \text{(III-3)}$$

$$= L(c-e) + L\frac{\partial\left(\overline{q'\omega'}\right)}{\partial p}, \qquad \text{(III-4)}$$

where q is the specific humidity.

Calculations of Q_1 and Q_2 can be made using equations (III-1) and (III-3) as the residual quantities of sounding network measurements of temperature, wind, and moisture (Yanai et al. 1973; Johnson 1976; Thompson et al. 1979; among others). Traditional budget studies are adversely affected by instrumental errors in radiosonde measurements and random sampling errors that alias small-scale variations in the winds and state variables on to larger scales (e.g., Mapes et al. 2003). In an effort to minimize these errors, Zhang and Lin (1997) developed a variational analysis technique that adjusts sounding observations within the range of measurement and instrument uncertainties to satisfy column-integrated budgets of mass, energy, and moisture. Though only the smallest possible adjustments are made, significant differences may appear in the resultant Q_1 and Q_2 profiles. More information on the variational analysis

technique and comparison to traditional budget method is reviewed in Zhang et al. (2001).

Profiles of the apparent heat source and moisture sink from field experiments overlapping the 25 years of weather state data are used in this study. Campaigns (listed in chronological order) include the Atlantic Stratocumulus Transition Experiment (ASTEX), Tropical Ocean Global Atmosphere (TOGA) Coupled Ocean-Atmosphere Response Experiment (COARE), South China Sea Monsoon Experiment (SCSMEX), TRMM-Large-Scale Biosphere-Atmosphere (LBA) Experiment, Kwajalein Experiment (KWAJEX), North American Monsoon Experiment (NAME), Tropical Warm Pool International Cloud Experiment (TWP-ICE), African Monsoon Multidisciplinary Analysis (AMMA), *Mirai* Indian Ocean Cruise for the Study of the MJO Onset (MISMO), and the Terrain-Induced Monsoon Rainfall Experiment (TIMREX). The average campaign Q_1 profiles (including an equally weighted ensemble average) are provided for context in Fig. B-3 and demonstrate the innate variability among domains prior to subsetting by weather state. Data availability, domain details, and references for the initial budget calculations (including discussion of the campaign average profiles) are summarized in Table B-1.

Data from ASTEX, TOGA, SCSMEX, NAME, AMMA, MISMO and TIMREX use traditional budget techniques relying solely on observations. Several of the projects have subdomains with profiles available for geographically different regions. These include separate basins over the northern and southern South China Sea (SCSMEX-N and SCSMEX-S), northern and southern regions of inland and coastal West Africa

(AMMA-N and AMMA-S), and land and ocean areas surrounding Taiwan (TIMREX-L and TIMREX-O). Variational analysis was used to determine the profiles from TRMM-LBA, KWAJEX and TWP-ICE. Additional budget calculations using variational analysis were available for TOGA and the SCSMEX-N domains. The corresponding Q_1 and Q_2 profiles for these regions were averaged with the estimates using the traditional budget approach for matching times before compositing by ISCCP regime. Although there were notable differences in the magnitude of heating between the traditional budgets and variational datasets (largely attributed to differences in the domain size), the shapes of the profiles were similar and both datasets were used in an effort to create a more realistic consensus.

Fig. B-2 shows the centers of the budget domains for each of the experiments listed in Table B-1, along with the annual average RFO for each of the ISCCP weather states. Many of the project domains are well placed to study the full range of ISCCP regimes, though reliable data for WS5, WS6 and WS7 are limited to the ASTEX region (i.e., open ocean areas northwest of Africa). While the ISCCP cloud properties may vary by region and show some seasonality, the budget studies range across a wide array of tropical and subtropical locations and include sampling from all times of the year. In addition, the compositing technique should eliminate any regional or seasonal bias, thereby producing a profile representative of the annual average, mean global cloud regime.

Special processing was necessary for the ASTEX dataset, which only contained Q_1 and Q_2 estimates from the surface to 4 km. As the ASTEX region is dominated by

shallow, marine boundary layer clouds, the total diabatic heating should be well represented by the radiative component in mid- and upper-levels. Consequently, we supplement the original Q_1 data above 4 km with the climatological values of Q_R over the ASTEX region during June using TRMM data from 1998-2010 following L'Ecuyer and Stephens (2003) and L'Ecuyer and McGarragh (2010).

All profiles were linearly interpolated to a constant pressure grid ranging from 1000-100 hPa in 25 hPa increments. Data at pressure levels below the surface were ignored. Most datasets include Q_1 and Q_2 calculations four times daily (at 0000, 0600, 1200, and 1800 UTC) and only those times were used when compositing with the ISCCP data. The Q_1 and Q_2 profiles were available every three hours for ASTEX and TWP-ICE with the compositing technique using all available profiles from these projects. Campaigns with less than 16 occurrences of a particular regime (including nighttime hours assigned their daytime adjacent classification) were disregarded based on subjective estimates of profile noise and overall representativeness. The numbers of samples for each experiment and ISCCP classification are provided in Table B-2. Although the budget domains occasionally span large regions with multiple ISCCP gridpoints, only the classifications nearest the center of the domain are used in the compositing technique.

No additional averaging was performed for the individual field campaigns. Equally weighted ensemble average profiles were calculated for each regime over mostly-land (TRMM-LBA, NAME, TWP-ICE, AMMA-N, AMMA-S, and TIMREX-L), mostly-ocean (ASTEX, TOGA, SCSMEX-N, SCSMEX-S, KWAJEX, MISMO, and

TIMREX-O), and all domains. Additional experiments calculating the ensemble mean with a weighted average (e.g., by number of observations) produced similar results as the equally weighted technique when using a minimum threshold filter.

c. Other Data

A 24-year control simulation was performed as a reference for global diabatic heating using the Community Atmosphere Model version 4 (CAM4). The model framework is identical to that utilized by Lappen and Schumacher (2012), with a time step of 1800 s, 26 vertical levels, and horizontal resolution of 1.9° latitude x 2.5° longitude using prescribed SSTs. A modified Zhang and McFarlane (1995) convective parameterization was used, in addition to boundary layer physics from Holtslag and Boville (1993), and a shallow convection scheme following Hack (1994). Monthly output of the total diabatic heating (and individual components) were produced from 1984-2007 and regridded to match the 2.5° x 2.5° ISCCP domain using an areal conservative remapping function.

Finally, the Wheeler and Hendon (2004) index is used to monitor the magnitude and phase of the Madden-Julian Oscillation (MJO, Madden and Julian 1994) during November – April of 1983-2008. Strong MJO events were identified as those days with a total Real-time Multivariate MJO (RMM) amplitude greater than or equal to one. Heating anomalies for strong events were calculated by MJO phase for each of the ISCCP regimes relative to the climatological background heating. Results from the modeling and MJO components of this study are presented in section 4.

3. Results

a. Q_1 Profiles

Composite profiles of the apparent heat source for each project meeting the minimum sample threshold and the ensemble average for all domains are shown in Fig. B-4. It is clear that WS1 (MCSs) has the largest ensemble average heating rate of all the regimes. Maximum heating occurs near 450 hPa and peaks near 8 K day^{-1}, more than twice the heating maxima from any other regime. The result is not surprising, however, as latent heating from precipitation production is the dominant component of the total diabatic field. WS1, which has the greatest average precipitation rate (~19 mm day^{-1}, Lee et al. 2013), would thus be expected to have the strongest latent component and total heating for the ISCCP regimes. The profile shape is top-heavy and likely explained by the presence of a significantly high stratiform rain fraction. Houze (1982; 1989) showed that higher stratiform rain fractions lead to stronger heating in the upper-levels of the atmosphere due to particle growth by deposition, with regions of cooling (and melting) below. Moreover, the result is in agreement with Jakob and Schumacher (2008) who found the analogous WS1 for a separate weather state study over the tropical west Pacific had stratiform rain fractions ranging from 50-70%. In addition, there is significant anvil radiative heating for WS1 (Li et al. 2013) contributing to the overall profile shape. The presence of deep heating throughout the entire troposphere (Fig. B-4a) also suggests that areas of convective rain (with heating maxima in the mid-troposphere) are present alongside the stratiform rain area. Although WS1 comprises the widest distribution of shortwave, longwave, and net cloud radiative forcing when

compared to the other weather states (Oreopoulos and Rossow 2011), the substantial variability among field campaigns is best explained by the differences in rain rate. For example, a single nocturnal event with extreme rain rates (in excess of 8 mm hr^{-1}) during TWP-ICE resulted in the anomalously large average value for this campaign and the mean profile becomes similar to the ensemble average when excluding this event.

The profile for WS2 has a similar shape to WS1, though peak heating for the ensemble average only reaches 3 K day^{-1} (note the scale difference for Fig. B-4a). This is in agreement with its significantly smaller average rain rate (~5 mm day^{-1}, Lee et al. 2013) and fewer clouds with large optical thickness (c.f. Fig B-1a, b). The peak heating occurs at 400 hPa, slightly higher than WS1. This difference may be explained by a higher percent stratiform rain and nonprecipitating anvil, as a weakening system initially classified as WS1 would produce an extensive stratiform area as it transitions to WS2. Rickenbach (2004) documented that MCSs during TRMM-LBA usually formed along the coast of Brazil and moved westward into the sampling domain well after reaching their convective peak. The extreme stratiform-like profile for TRMM-LBA in Fig. B-4b exemplifies this point, and the number of samples for WS2 in TRMM-LBA is three times as many for WS1 (Table B-2). WS3 also achieves a peak heating of 3 K day^{-1}, but has a broad maximum from 600-400 hPa. The lowering height of the heating maximum is best explained by the mixed and weaker nature of WS3 convection (cumulonimbus and congestus) and a smaller stratiform rain fraction (Jakob and Schumacher 2008). There is also considerable variability among campaigns due in part to differing rain rates.

WS4 represents thin cirrus and has weak heating (less than 1.5 K day^{-1}) for the ensemble average throughout the entire troposphere. Although many of the individual domains have small heating peaks above 200 hPa, the primary heating peaks are in the lower- (950 hPa) and mid- (500-400 hPa) troposphere. The near surface peak is likely attributed to sensible heat fluxes over land domains and the redistribution of this heat by turbulent eddies and shallow cumulus that often accompany tropical cirrus (e.g., Jakob et al. 2005; Schumacher et al. 2008). The mid-level peak may be a result of thin anvil and outflow from tropical convection reaching only moderate heights, consistent with the cloud type heating profiles of Schumacher et al. (2008) derived from visual observations during KWAJEX.

WS5, WS6, and WS7 are responsible for significant cooling throughout most of the atmosphere. WS5 and WS6 have similar profile shapes with weak near surface heating (less than 1 K day^{-1}) up to 950 hPa, with cooling of 5 K day^{-1} and 3 K day^{-1} at 850 hPa, respectively. WS7 has slightly stronger surface heating to 900 hPa and a similar cooling peak (3.5 K day^{-1} at 825 hPa), resulting in a smaller net cooling than the previous two regimes. These results are consistent with the budget calculations and net surface and top of atmosphere longwave cloud radiative effects determined for the ISCCP extended low-latitude weather states by Oreopoulos and Rossow (2011). Although the composites are limited to the ASTEX region, the shapes and magnitude of the Q_1 profiles agree with prior work. For example, Nitta and Esbensen (1974) observed shallow, nonprecipitating stratocumulus clouds in the eastern Caribbean during the Barbados Oceanographic and Meteorological Experiment (BOMEX), with results

similar to ours[1]. The remainder of the profile above 4 km (~650 hPa) is the climatological Q_R derived from TRMM data (see section 2), which resembles typical clear sky radiative cooling with values generally around 1.25 K day^{-1}.

The average profile for WS8 shows a maximum of 1 K day^{-1} at 950 hPa with very weak heating observed throughout the remainder of the troposphere. Although these cloud types are generally nonprecipitating and have zero net latent heating, the convective mass flux is capable of redistributing heating, with low-level warming from eddy transport and condensation in cloud, and cooling above due to evaporation and detrainment (e.g., Nitta and Esbensen 1974). There is significant spread among the individual heating estimates in the mid-levels (up to 7 K day^{-1}) and this uncertainty is discussed in more detail below.

The fidelity of these results was further examined by calculating the ISCCP regime average profiles excluding the Q_1 dataset from a particular field campaign and reconstructing the observed mean heating profile for that field campaign as a function of weather state frequency of occurrence. The predicted reconstructions and sounding-based campaign-average profiles (excluding ASTEX) are shown in Fig. B-5. Generally, most of the predictions have relatively small error compared to the original Q_1 observations. The reconstructed profile for TRMM-LBA (Fig. B-5d) has too little upper-

[1] Sufficient numbers of samples above the minimum threshold were available from AMMA-S for WS5, and AMMA-N for WS6 and WS7. These profiles were omitted from the analysis, however, as they exhibited strong near surface effects and contained heating of several K day^{-1} throughout the entire troposphere. These profiles were deemed unrepresentative of the main WS5, WS6, and WS7 populations, which primarily occur over the oceans (Fig. 2). Similar data were also rejected for WS7 from MISMO that more closely resembled the heating profiles for altocumulus clouds determined by Schumacher et al. (2008).

level heating and is consistent with the previous discussion of observations favoring weakening MCSs and large stratiform rain fractions for this domain. The predicted heating for KWAJEX (Fig. B-5e) is more top-heavy than observed. This difference is a result of notably weaker upper-level heating for WS2 compared to the regime average for all domains (Fig. B-4b) and likely attributed to the frequency of shallow and only moderately deep daytime convection in this region (Schumacher et al. 2007). TWP-ICE has the most heating of any campaign (Fig. B-3) and is the least well reconstructed of any domain (Fig. B-5g). The TWP-ICE average is strongly affected by the anomalously large heating estimates from WS1 (Fig. B-4a) that are dominated by a single extreme rain event (> 8 mm hr^{-1}). The predicted profile better aligns with the TWP-ICE observations when excluding this event from the averaging (not shown). Finally, there are also large differences in the structure of the observed and reconstructed heating over the TIMREX-L domain (Fig. B-5k). Outside of 11 days of heavy rainfall (> 20 mm day^{-1}), the TIMREX-L domain was dominated on the remaining 31 days by shallow afternoon convection and reduced mid- and upper-level relative humidity, which helps explain the bottom-heavy nature of the observed profile (Ruppert et al. 2013). Another possible reason for the poor reconstruction was that the TIMREX-L network was quite small (filling up only 40% of the 2.5° x 2.5° gridbox) and the ISCCP cloud properties over this area are likely dominated by deeper oceanic convection (as in TIMREX-O) giving the impression that the heating is more top-heavy than actually observed.

Differences in the mean profile for regimes 1-4 and 8 over mostly-land and mostly-ocean domains are shown in Fig. B-6. All of the regimes have a tendency for

enhanced heating at low levels (~1 K day^{-1}) over mostly-land domains. Stronger sensible heating and an enhanced diurnal cycle over land likely cause this result. The shape and magnitude of the mean heating profile for WS1 is nearly identical over land and ocean (Fig. B-6a). This result is consistent with previous work, as Lee et al. (2013) documented comparable precipitation rates over both domains when excluding nonprecipitating pixels (i.e., zero rain rate) from their averaging.

The mean profiles for WS2 show enhanced heating over the ocean from 875-550 hPa, with less heating relative to land domains from 550-100 hPa (Fig. B-6b). These differences are likely nonphysical, as the WS2 land composite is strongly influenced by the individual heating profile from TRMM-LBA. As previously mentioned, the TRMM-LBA retrieval is biased towards extreme stratiform rain fractions given the characteristic evolution of South American MCSs developing along the Brazilian coast and moving westward into the analysis domain well after reaching their convective peak.

The profile shapes are similar for WS3 (Fig. B-6c), with the exception of stronger near surface heating identified over land in AMMA-N and AMMA-S (Fig. B-4c). The ocean profile contains slightly more heating in mid-levels relative to land (~1 K day^{-1}) and is likely due to the presumed heavier rain rates for MISMO and TIMREX-O (Fig. B-4c). The land and ocean composites for WS4 (Fig. B-6d) also have similar shapes to the ensemble average, though the heating maxima are 1.5-2.5 K day^{-1} greater over land at both the low- and mid-level peaks. The enhanced sensible heat flux over the AMMA-N and AMMA-S domains likely accounts for the lower peak, though an appropriate reason for differences in the mid-levels is not immediately clear. It is

possible that there is a greater frequency of more dense (i.e., higher optical thickness) cirrus anvils and outflow from convection peaking near 500 hPa over land, though this hypothesis requires further investigation.

The domain differences in Q_1 are most pronounced for WS8 (Fig. B-6e). There is weak heating (< 1 K day^{-1}) over the ocean from the surface to 925 hPa, with weak cooling throughout the rest of the troposphere. This profile matches the expected shape for nonprecipitating, shallow cumulus at low-levels with clear sky radiative cooling above. The land composite meanwhile has peak heating of ~2.5 K day^{-1} between 950-900 hPa with moderate warming (1-2 K day^{-1}) up to 200 hPa. A broad heating maximum exists from 600-400 hPa for the land-only composite, similar to the average profile for WS3 (i.e., cumulonimbus/congestus). Furthermore, all of the individual land domains show heating throughout the entire troposphere, while ocean areas primarily contain cooling above 925 hPa (Fig. B-4h). Oreopoulos and Rossow (2011) identified WS8 as having the smallest mean cloud radiative effect compared to all other regimes, indicating a weak cooling of the atmosphere. The above finding is consistent with our integrated total diabatic heating for ocean domains.

Lee et al. (2013) found the average rain rate for WS8 was greater over land than ocean. Although the mean rain rates for both domains were small (< 1 mm day^{-1}), these totals included areas without any precipitation (i.e., zero rain rates) and 80-90% of their WS8 pixels were nonprecipitating. Those areas where WS8 produced heavier precipitation (coincident with our land domains) had average rain rates of 2-5 mm day^{-1}, comparable to those from WS3 over the same regions.

Given the predominance and persistence of WS8 over the oceans (Fig. B-2h), along with clustering at low heights and weak-to-moderate optical thickness (Fig. B-1h), we expect the cloud field over the ocean domain would be mostly homogenous. A similar "most likely" probability exists for clouds of low height and low thickness over land, but prominent changes in surface use or other heterogeneities could allow certain pixels within the larger population to grow to higher heights or achieve larger values of optical thickness (i.e., the "tails" of the cluster distribution in Fig. B-1h). The joint histograms for these regions might look similar to WS3, excluding the cumulonimbus population in the upper-right (Fig. B-1c), and their overall distribution and lower cloud fraction would result in their being categorized as WS8. The previous scenario, in tandem with the observed increase in precipitation rates, could potentially explain the differences between the Q_1 profiles for our land and ocean domains. Nevertheless, verification of the above hypothesis is beyond the scope of this work.

b. Q_2 Profiles

Composites of the apparent moisture sink for each regime are shown in Fig. B-7. Estimates of Q_2 for individual campaigns generally demonstrate more variability than Q_1 (Lin and Johnson 1996; Johnson and Ciesielski 2000) and the following discussion focuses on relative variability between regimes.

There is strong drying (positive values) throughout the entire depth of the troposphere for WS1 (Fig. B-7a). The profile has two peaks with a maximum of 3.5 K day^{-1} and 5 K day^{-1} at 825 hPa and 475 hPa, respectively. As identified earlier, there is

significant convective and stratiform rain associated with WS1. The dual peak is consistent with Johnson (1984), where low-level drying occurs in convective updrafts and drying at upper-levels is a result of mesoscale lifting within the stratiform region. As with Q_1, the shapes of the drying profile for WS2 and WS3 are similar to WS1, though the peak amplitudes are greatly reduced (1.75 K day^{-1} and 2.5 K day^{-1} for each regime, respectively). WS2 has a top-heavy drying profile due to the increased stratiform rain fraction while the WS3 profile is more bottom-heavy as the convection becomes weaker and contains a lower fraction of stratiform rain (similar to the trends for Q_1). The ensemble average profile for WS4 is near-zero throughout the entire troposphere.

There is primarily moistening (negative values) throughout the lower atmosphere for WS5, WS6, and WS7 (Fig. B-7e, f, g) attributed to surface evaporation and upward transport of water vapor by clouds. Maritime stratus and stratocumulus are persistent across local regions (Fig. B-2e, f) and have average precipitation rates less than 1 mm day^{-1} (Lee et al. 2013). Variations in the magnitude of the low-level moistening among WS 5-7 reflect differences in the balance of evaporation (adding moisture) and precipitation (removing moisture) in these regimes. WS5 has a slightly higher average precipitation rate (Lee et al. 2013) and displays a weaker peak moistening of 4 K day^{-1} compared to the 6 K day^{-1} maximum for WS6 and WS7. The ensemble average drying profile for WS8 is particularly noisy with weak moistening and drying (< 1 K day^{-1}) below and above 600 hPa, respectively.

Fig. B-8 shows the equivalent average drying profiles over land and ocean domains. Low-level moistening is apparent for WS2, WS3, WS4, and WS8 over the

oceans due to increased eddy transport of near surface water vapor. The magnitude and height of the moistening layer vary by regime and are most pronounced for WS8 (Fig. B-8e). Moistening over oceans exceeds 2 K day^{-1} at 875 hPa for the cumulus regime, generally consistent with Schumacher et al. (2008). WS8 has relatively large drying (~3 K day^{-1}) throughout the low-levels over land, consistent with the idea that these regimes precipitate more easily and have larger average rain rates over these domains.

Another common feature of the land and ocean profiles is the enhanced moistening over land areas peaking near 600 hPa for WS1, WS2, WS3, and WS4. This anomaly is best explained by detrainment from enhanced populations of cumulus congestus with cloud tops near the freezing level (e.g., Johnson et al. 1999). It is thus postulated that the ISCCP regimes have a more frequent occurrence of mid-level and congestus clouds over land domains for several of the weather states, consistent with the general findings of Casey et al. (2007), though further investigation is again necessary to prove this hypothesis.

4. Applications

The following section briefly illustrates two potential uses of the total diabatic heating composites derived for the ISCCP regimes. A simple linear combination of the ensemble average heating profile from all domains, weighted by the relative frequency of occurrence at each gridpoint for each weather state, is used to reconstruct a full four-dimensional total heating field. Each of the projects below is the subject of additional

work by the various coauthors and will be explored in more detail in forthcoming publications.

a. Comparisons to CAM4 Heating

The vertical structure of the annual average, zonal mean diabatic heating from 1984-2007 is shown in Fig. B-9 for the ISCCP reconstruction and CAM4 total heating (i.e., the sum of moist processes, vertical diffusion, longwave, and shortwave heating rates) for the simulation described in section 2. Corresponding difference fields (ISCCP-CAM4) are shown in the rightmost panel of Fig. B-9, where warm colors indicate greater heating (or less cooling) for ISCCP. Overall, CAM4 agrees with the magnitude and extent of the ISCCP heating from deep tropical convection (especially within the ITCZ at 7.5°N), though ISCCP produces more heating (or not enough cooling) throughout the mid-troposphere in much of the subtropics.

Representative maps of the annual average, ISCCP-derived and CAM4 heating (not shown) indicate that the ISCCP reconstruction matches the large-scale patterns of heating and cooling predicted by CAM4 at low-levels. Although CAM4 produces excessive heating in regions with high elevations (e.g., east Africa and the Tibetan plateau), large regions of the tropics and subtropics have small differences (< 0.25 K day^{-1}) between the two datasets. Differences in the heating field become more pronounced in the mid-levels and maximize over the marine boundary layer cloud regimes of the east Pacific and subtropical Atlantic oceans. There is also some difference along the northern and southern boundaries of the domain (i.e., 35°N and 35°S) in the

Indian and Pacific oceans. These regions are likely influenced by mid-latitude systems (including nimbostratus clouds associated with warm and cold fronts) that are not accurately depicted in the extended low-latitude ISCCP weather states (e.g., Oreopoulos and Rossow 2011).

The largest inconsistencies between CAM4 and ISCCP generally occur over the regions with the greatest frequency of occurrence for the fair-weather cumulus regime. The notable difference in the average heating profiles for WS8 over land and ocean (Fig. B-6e) suggest it may be appropriate to apply separate profiles during the linear combination over the respective areas in lieu of using the all domain composite, as is done for the other regimes. The WS8 ocean profile has cooling at mid-levels, characteristic of clear sky, and would help offset the differences between CAM4 and ISCCP. Additional reconstructions using separate lookup profiles for WS8 over land and ocean were performed and the peak geographic difference was reduced by approximately 1 K day^{-1} or 50% of the original value (not shown). The improved performance over oceans comes at the expense of larger differences over land, however, as the corresponding WS8 profile has moderately strong heating of 2-3 K day^{-1} at mid-levels. The difference between the realizations using different lookup profiles presents a range of uncertainty for our estimates, and the large-scale sensitivities and dynamical response of GCMs forced with these heating variations is the subject of future work.

b. Heating Anomalies during the MJO

Despite continued advances in modeling, GCMs continue to struggle with reproducing the salient features of the MJO (Zhang et al. 2006; Li et al. 2009; among

others). Changes to the shape and magnitude of the diabatic heating profiles produced by convective parameterizations have a significant effect on a GCM's ability to simulate the MJO. Recent studies have underscored the importance of both horizontal and vertical heating variations, with low-level heating from shallow convection thought to induce large-scale moisture convergence and preconditioning the environment for MJO initiation (e.g., Mu and Zhang 2008; Li et al. 2009; Jia et al. 2010). Lappen and Schumacher (2012) produced better simulations of the MJO in CAM4 when forcing the model with a realistic horizontal and vertical distribution of latent heating derived from the TRMM PR. They speculated their simulations would see continued improvement with the addition of low-level heating anomalies associated with shallow convection and nonprecipitating clouds that the TRMM PR cannot detect.

Maps of the heating anomalies for each weather state were composited by phase during strong MJO events (see section 2) using the Wheeler and Hendon (2004) index. Results for the cumulus regime (WS8) and the corresponding low-level heating anomalies sorted by MJO phase for November-April during 1983-2008 are shown in Fig. B-10. Small areas of weak average positive anomalies (0.05-0.10 K day^{-1}) are evident at 940 hPa over central Africa during phase 4 (Fig. B-10d) and grow in size and strength as they propagate eastward along the equator. The WS8 heating anomalies cover a broad area of the warm pool region during phase 1 and reach their peak intensity of 0.20-0.25 K day^{-1} at that time. They eventually become indistinguishable as the signal propagates over the central Pacific Ocean during phases 3 and 4. The background heating for this regime (regardless of phase) is ~1 K day^{-1}, meaning the associated

anomalies may be as large as 20-25% the mean heating. A strong negative anomaly meanwhile lags the peak heating by 3-4 phases and is centered over the locations usually associated with deep convection for each stage of the MJO. A similar lag and exchange of suppressed clouds leading the convectively active regime was identified in Tromeur and Rossow (2010) using a subset of the tropical ISCCP weather states.

Vertical profiles of the anomalous total heating from all ISCCP regimes during each phase of the MJO are shown in Fig. B-11 for the equatorial eastern Indian Ocean and west Pacific. Upper-level anomalies during the active MJO phases in each region (phases 2 and 3 in the Indian Ocean and phases 5 and 6 in the west Pacific) reach ~1 K day^{-1} at 400 hPa, which is generally consistent with the height and magnitude of MJO heating anomalies diagnosed using TRMM data (Jiang et al. 2011). The vertical structure of the diabatic heating composite is mostly upright (also consistent with TRMM retrievals) and does not show the characteristic westward tilt with height that is commonly identified in reanalysis data (Jiang et al. 2011). Although the ISCCP reconstructions are capable of diagnosing the heating contributions from predominantly shallow, boundary layer clouds (WS8), these anomalies are located far in advance of the deep convective core and appear unattached to the main upper-level heating signature.

Considering the idealized anomalous tilted heating structure of the MJO, one might expect mid-level convection and cumulus congestus (e.g., WS3) to be the principle cloud regime found throughout the east-to-west transition from shallow to deep convection. However, anomalous heating contributions from WS3 do not occur in the transition phases and are located along the northern and southern peripheries of the same

longitudes as the mid- and upper-level heating anomalies from deep convection comprising WS1 and WS2 (not shown). This result is consistent with Tromeur and Rossow (2011) who showed the equivalent WS3 frequency of occurrence was mostly insensitive to MJO phase and Riley et al. (2011) who demonstrated that the cumulus congestus mode was relatively weak and aligned with (rather than preceding) the location of wide, deep precipitating systems using *CloudSat* data. Furthermore, the quick transition from WS8 to WS1 during initiation is consistent with the rapid onset of moistening and upward motion during early development of the MJO (e.g., Tromeur and Rossow 2010). Further evaluation of the MJO response in CAM4 from including the effects of the nonprecipitating regime (WS8) or total heating composites from all weather states will be the subject of future work.

5. Summary and Discussion

This study has created representative profiles of the apparent heat source (Q_1) and moisture sink (Q_2) for a number of unique cloud populations from a 25-year subset of the ISCCP dataset. Profiles were created by compositing calculations of Q_1 and Q_2 derived from field campaign sounding observations across a wide variety of tropical and subtropical domains according to commonly occurring cloud mixtures, or "weather states". While the ISCCP regimes describe populations of clouds occurring within a larger domain (2.5° x 2.5°) and inevitably contain overlap, the composite profiles for each weather state were unique and highlight the importance of considering all

components (latent, radiative, and eddy sensible heating) when determining characteristics of the total diabatic heating.

The heating profiles were well explained by the convective properties and types of clouds within each regime. The weather state characteristic of intense MCSs (WS1) had the strongest heating with a top-heavy profile owing to the large stratiform rain contribution and anvil area observed in previous work. The heating profiles showed a gradual transition to weaker values and lower heights as the convective intensity decreased (e.g., WS2 and WS3). Despite being primarily associated with thin cirrus, WS4 had the largest heating at low- and mid-levels. It was suggested that the low-level feature is a consequence of the redistribution of heat by cumulus clouds commonly observed with cirrus in the tropics (e.g., Jakob et al. 2005; Schumacher et al. 2008), while the mid-level feature may be from anvil clouds that otherwise are classified as WS4 based on their histograms of cloud top pressure and optical thickness. WS5, WS6, and WS7 are all responsible for significant cooling and mainly occur over the eastern ocean basins. The regime describing mostly nonprecipitating, shallow cumulus (WS8) had weak heating near the surface with different estimates of heating or cooling aloft depending on whether the regime was present over land or ocean. Other regimes had similar total heating characteristics for land and ocean domains. The ensemble average Q_1 profiles for each regime were generally consistent with previous work identifying heating for specific cloud types (e.g., Nitta and Esbensen 1974; Schumacher et al. 2008).

Profiles of the apparent moisture sink showed intense drying for WS1, with weaker drying for the remaining convectively active weather states. The marine

boundary layer regimes showed moistening of the lower atmosphere due to vertical eddy transport of near surface water vapor and detrainment aloft without much loss from precipitation. Additional mid-level moistening for WS2 and WS3 was apparent over land, suggesting enhanced detrainment and more frequent mid-level and congestus clouds compared to ocean domains.

Two potential applications of the ISCCP composites were discussed. The first included a comparison and benchmark against diabatic heating produced from a long-term GCM simulation. Though neither the ISCCP nor CAM4 realization can be regarded as the truth, the general consensus among solutions provides some sense of validation for each. Differences in the strength of the heating were more significant at mid- and upper-levels, largely explained by the uncertainties in the heating profile for the cumulus regime (WS8). Future work plans to examine the large-scale response in a GCM to variations in these heating profiles and compare the results with other estimates of the Hadley circulation derived from reanalyses (e.g., Stachnik and Schumacher 2011).

A second application focused on the retrieval of low-level heating associated with shallow convection and the MJO. Although these cloud types are usually nonprecipitating and have a weak net latent heating effect, they produce low-level moistening and a redistribution of heating that may potentially induce large-scale moisture convergence and promote the onset of MJO initiation. Heating anomalies from WS8 were identified well in advance of the locations of deep convection, though the remainder of the regimes had anomalies over the same locations, suggesting a rapid change from shallow to more deep and organized convection. The observed ISCCP

heating (in agreement with previous TRMM results) did not reproduce a vertically-tilted diabatic heating structure, casting some doubt on whether the vertical tilt identified in reanalysis data is as evident in reality.

Finally, the separation of diabatic heating profiles by regime provides a unique metric for the evaluation of implicit cloud properties in climate models. Many GCMs now include an ISCCP simulator, and comparisons of the derived model properties with observations can yield new insights into the potential strengths and weaknesses of convective parameterizations and help quantify those cloud types with the largest uncertainties and potential impacts on tropical climate dynamics.

CHAPTER IV

TROPICAL AND SUBTROPICAL CLOUD REGIMES IN THE MERRA REANALYSIS USING AN ISCCP SIMULATOR

1. Introduction

Reanalyses combine observations with a dynamical model in order to create a gridded numerical product that provides a complete three-dimensional state of the atmosphere throughout the historical data record. Although many atmospheric reanalyses are now available as centers worldwide continue to improve upon and produce new datasets, reanalyses often contain substantial variability at low-latitudes given the lack of observations over the tropical oceans and are largely dependent on the underlying model parameterizations and assumptions in these regions. For example, Stachnik and Schumacher (2011) showed that an ensemble of eight atmospheric reanalyses contained significant variability in the climatological representation of the tropical Hadley circulation (in excess of 30% the ensemble mean), in addition to discrepant long-term trends concerning Hadley cell intensity and width. Futhermore, reanalyses often differ from observations and atmospheric general circulation models (GCMs) regarding the Hadley circulation mean state (e.g., Mitas and Clement 2006; Johanson and Fu 2009) and derived climate trends throughout the twentieth and twenty-first centuries (Hu and Fu 2007; Seidel and Randel 2007; Mantsis and Clement 2009).

It remains a topic of debate as to whether reanalyses can successfully be used to identify long-term physical and dynamical climate trends given discontinuities in the

observational record and analysis uncertainties prior to the global satellite era (e.g., Bengtsson et al. 2004; Thorne and Vose 2010). As with many GCMs, discrepancy among reanalysis solutions in the tropics (including Hadley cell trends) often stems from the representation of clouds and their associated radiative effects (e.g., Song and Zhang 2007). Verification of modeled cloud properties in reanalyses has remained a difficult task, in part due to the limited availability of cloud diagnostics. For example, most reanalyses datasets only contain bulk properties of modeled clouds over three atmospheric layers (low, middle, and high). Furthermore, reanalyses do not explicitly predict cloud type. Understanding what cloud types or cloud regimes contain the greatest error in fractional coverage and corresponding optical properties may be useful for improving cloud parameterizations and reducing overall error and uncertainty of climate sensitivity in models and reanalyses (e.g., Webb et al. 2001; Lin and Zhang 2004; Zhang et al. 2005; Williams and Tselioudis 2007; Williams and Webb 2009).

Numerous GCMs now include a satellite instrument simulator as part of their run-time calculations in order to elucidate implicit properties of modeled clouds and to better facilitate comparisons to observations. One such example includes the International Satellite Cloud Climatology Project (ISCCP, Schiffer and Rossow 1983) simulator that was designed to mimic observed visible and infrared satellite radiances from grid-scale variables of modeled clouds and return a distribution of simulated cloud-top pressure and optical thickness values over a relatively coarse domain. Results from the ISCCP simulator (Klein and Jakob 1999; Webb et al. 2001) can be combined with other ISCCP algorithms that identify recurring cloud regimes or "weather states"

(described in section 2) to determine the ability of a GCM to predict the full range of observed cloud types across a local or global domain. Previous studies using the ISCCP simulator in forecast models and GCMs indicate a variety of biases compared to observed clouds with most models significantly underpredicting the coverage and radiative effects of thin, high clouds (Klein and Jakob 1999; Webb et al. 2001; Zhang et al. 2005; Williams and Webb 2009). Those studies using clustering analysis or regime sorting find a similar lack of high clouds in GCMs (e.g., Chen and Del Genio 2009) and other potential errors in low-level cloud reflectivity (Williams and Tselioudis 2007).

Despite these advances, it remains unknown whether the tropical and subtropical cloud properties in reanalyses benefit from the dynamical constraints of routine data assimilation or if these datasets exhibit the same biases as GCMs due to the lack of *in-situ* low-latitude upper-air observations. This study uses data from the National Aeronautics and Space Administration (NASA) Modern-Era Retrospective Analysis for Research and Applications (MERRA) reanalysis to simulate properties of the observed ISCCP cloud regimes. Posselt et al. (2012) recently examined simulated cloud properties in MERRA using Clouds and the Earth's Radiant Energy System (CERES) measurements onboard the Tropical Rainfall Measuring Mission (TRMM) satellite (Kummerow et al. 1998), though their analysis was restricted to deep convective objects with cloud heights in excess of 10 km over a limited data period.

Our work extends the findings of Posselt et al. (2012) to the entire range of observed tropical and subtropical cloud systems using a 25-year satellite dataset. The ability (or lack thereof) of MERRA to simulate specific cloud regimes could be

paramount to understanding the fidelity of using tropical reanalysis data to quantify long-term climate trends. Furthermore, several observational metrics related to the ISCCP cloud regimes are now available for model verification including the radiative, precipitation, and total diabatic heating characteristics of each regime (Oreopoulos and Rossow 2011; Lee et al. 2013; Stachnik et al. 2013). The separation of reanalysis clouds by predominant cloud type provides the unique opportunity to verify the MERRA data using the above metrics in addition to comparing the large-scale environmental conditions associated with each regime.

2. Data and Methods

a. ISCCP Weather States

The ISCCP cloud regimes or "weather states" (Jakob and Tselioudis 2003; Jakob et al. 2005; Rossow et al. 2005) represent physically meaningful and recurring mixtures of cloud types from individual pixels of about 5 km in size occurring within a larger 2.5° x 2.5° gridbox. Weather states are classified according to repeating patterns of cloud height and extinction covariance taken from the ISCCP D1 dataset (Rossow and Schiffer 1999) using a *k*-means clustering algorithm (Anderberg 1973). Details of the weather state retrieval and initial dataset are described in Rossow et al. (2005).

The extended low-latitude ISCCP weather state data covers the 25-year period from 7/1983 – 6/2008 and is available for download from the NASA Goddard Institute for Space Studies (GISS) website at http://isccp.giss.nasa.gov/etcluster.html. Data cover the entire 35°N-35°S domain and are available at 3-hr resolution for daytime hours only.

The clustering algorithm identifies eight unique weather states (WS1-8) based upon the joint distributions of cloud-top pressure (p_c) and optical thickness (τ). Each gridpoint is assigned the corresponding regime with the minimum Euclidian vector distance to the idealized cluster centroids (i.e., mean p_c-τ histogram). In addition, the ISCCP gridpoints may be classified as a separate weather state (WS0) if the entire field of view is clear. The idealized cluster centroids for each regime are shown in Fig. C-1 and the corresponding geographic relative frequency of occurrence (RFO) is provided for reference in Fig. C-2. The sum of the cloud fraction in each extinction and height bin ("cluster cloud fraction" or CCF) represents the average total cloud cover for each regime and is listed in the top right of each panel in Fig. C-1.

Briefly, the weather states contain cloud mixtures describing mesoscale convective systems (MCSs) with large values of optical thickness and high cloud tops occurring in the deep tropics (WS1, Figs. C-1a and C-2a) and more frequent, though less vigorous convection with generally lower extinction and cloud tops (WS2 and WS3, Figs. C-1b-c and C-2b-c). WS4 represents predominantly cirrus with underlying low clouds (Fig. C-1d) and occurs over both land and ocean (Fig. C-2d). WS5, WS6, and WS7 describe low-level mixtures of stratus and stratocumulus clouds (Figs. C-1e-g) principally found over regions of cold sea surface temperature (Fig. C-2e-g). Finally, WS8 is indicative of fair-weather cumulus with low optical thickness and shallow cloud tops (Fig. C-1h) and has the highest RFO of any regime (Fig. C-2h). The clear weather state (WS0) has the lowest frequency of all the regimes (domain average RFO less than 4.5%) and occurs predominantly over land. Previous studies have shown that the tropical

and subtropical ISCCP weather states have unique radiative and precipitation characteristics (Oreopolous and Rossow 2011; Lee et al. 2013) and a more detailed discussion of the ISCCP cloud properties (in addition to the total diabatic heating profiles for each weather state) is presented in Stachnik et al. 2013.

b. Reanalysis Data

NASA MERRA is used as the reanalysis dataset in this study. The MERRA dataset was specifically designed to improve upon the representation of the hydrological cycle in reanalyses and makes extensive use of satellite radiance data assimilation from both recent and historical observing platforms. A complete overview of MERRA is presented in Rienecker et al. (2011) and the references within; we provide a brief overview of the data and model physics relevant to our study.

MERRA utilizes version 5.2.0 of the Global Modeling and Assimilation Office (GMAO) Global Earth Observing System (GEOS) atmospheric GCM and the corresponding Data Assimilation System (DAS), both of which are documented in Rienecker et al. (2008). Special emphasis is placed on the assimilation of satellite radiances evolving in time, in addition to conventional observations (e.g., radiosondes, aircraft, and surface weather stations). The native model resolution is 1/2° latitude x 2/3° longitude with 72 vertical levels ranging from 1000-0.01 hPa. High-resolution reanalysis output is available on the same horizontal grid at 42 pressure levels with select variables available at up to hourly resolution from January 1979 to present. We retain 30 vertical levels below 10 hPa for our analysis and regrid all surface and upper-air variables to the

ISCCP 2.5° x 2.5° degree grid for all 6-hr time steps overlapping the 25-year weather state dataset.

MERRA is unique in that output variables include tendency terms for the model physics and dynamics, precipitation fluxes, and other cloud diagnostics not normally included in reanalysis output. Similarly, MERRA contains 3-dimensional output of cloud fraction and cloud water (both liquid and ice), whereas most reanalyses only contain discrete cloud fractions for three atmospheric layers (e.g., low, medium, and high). Cloud diagnostics include separate output for condensate from the cumulus parameterization and anvil (i.e., detrained convection) in addition to that from large-scale moistening. MERRA uses the relaxed Arakawa-Schubert convective parameterization (Moorthi and Suarez 1992) and a statistical scheme for moist physics and large-scale clouds based on Bacmeister et al. (2006). Both cloud fraction and mass for large-scale and anvil clouds may experience loss from evaporation, precipitation autoconversion, sedimentation, and accretion and were binned together in our data processing. Separate autoconversion calculations for the convective clouds are done following Sundqvist (1978) and fallout and precipitation are based on statistics of updraft plumes based on Sud and Walker (1999).

Although the global average precipitation rates in MERRA exhibit some discontinuity with the introduction of assimilated satellite radiances from the Special Sensor Microwave Imager (SSM/I) and Advanced Microwave Sounding Unit-A (AMSU-A) in July 1987 and November 1998, respectively, the overall precipitation fields show improvement from previous generations of reanalysis data (Rienecker et al.

2011). Zonal-average precipitation for MERRA best matches the Global Precipitation Climatology Project (GPCP, Adler et al. 2003) estimates of tropical and subtropical rainfall (Stachnik and Schumacher 2011) and the improvement in precipitation spatial distribution and variance is attributed primarily to better predictions over the tropical oceans (Bosilovich et al. 2011). Additional comments regarding the global energy and water budgets in addition to the effects of changing observations are found in Bosilovich et al. (2011) and Robertson et al. (2011).

c. ISCCP Simulator

The Cloud Feedback Model Intercomparison Project (CFMIP) Observation Simulator Package (COSP; Bodas-Salcedo et al. 2011) includes an ISCCP simulator (e.g., Klein and Jakob 1999; Webb et al. 2001) designed to reproduce observed satellite radiances from gridded model output of cloud diagnostics and other state variables. The ISCCP simulator is three-fold. Gridbox mean quantities (including mass and cloud fraction of convective and large-scale condensate) are first passed to the Subgrid Cloud Overlap Profile Sampler (SCOPS), which generates a number of random profiles within the gridbox using either a random (all cloud) or maximum-random (convective and large-scale cloud, respectively) vertical overlap parameterization. The random overlap provides a larger mean total cloud fraction, whereas the maximum option simulates a greater optical depth by assuming convective cloud fraction in adjacent vertical layers are maximally overlapped (e.g., Morcrette and Fouquart 1986; Pincus et al. 2005). Next, the instrument simulator calculates the ISCCP radiances for each subcolumn within the

larger gridbox. Finally, a statistical model is employed that generates the subcolumn distribution of optical depth and cloud-top pressure within the original model gridpoint that can then be compared to the observed ISCCP cloud histograms.

Offline calculations were necessary to convert MERRA cloud water and ice mixing ratios to the required COSP input. Convective cloud condensate in MERRA is not distinguished by phase and was partitioned using a linear transition from ice to liquid water over a temperature range of 258-273 K. The large-scale and anvil cloud types were already separated by phase and the corresponding mixing ratios at every model level were converted into a liquid water or ice water path (LWP and IWP) and visible optical thickness (τ_{vis}, 0.67 μm) according to the following simple relationship,

$$\left.\begin{aligned} LWP &= 6.292\tau_{vis} \\ IWP &= 10.5\tau_{vis} \end{aligned}\right\}, \qquad \text{(IV-1)}$$

where the above coefficients are consistent with the ISCCP D1 series data with an effective particle radius of 10 μm and 30 μm for liquid drops and ice crystals, respectively (Rossow and Schiffer 1999). Corresponding infrared optical depths (τ_{ir}, 10.7 μm) were calculated based on Mie scattering theory and the matching ISCCP D-series coefficients where

$$\left.\begin{aligned} \tau_{ir,liquid} &= \frac{\tau_{vis}}{2.56} \\ \tau_{ir,ice} &= \frac{\tau_{vis}}{2.13} \end{aligned}\right\}. \qquad \text{(IV-2)}$$

Finally, the values of τ_{ir} were converted to an infrared emissivity using a standard Beer's law relationship. Liquid and ice water contributions were summed together in each

model layer to create a total visible optical thickness and infrared emissivity for both convective and large-scale condensate that was then passed to the ISCCP simulator. Additional sensitivity experiments were performed using newer water content and optical depth relationships (e.g., Heymsfield et al 2003), though these resulted in worse comparisons between the simulated and observed ISCCP data.

The ISCCP simulator was run on all 6-hr MERRA data using both the random and maximum-random vertical cloud overlap parameterizations with 200 subcolumns for each 2.5° x 2.5° gridpoint. The model calculates the total cloud optical depth for each subcolumn and a corresponding infrared brightness temperature based on skin temperature and surface emissivity, atmospheric temperature and specific humidity, and cloud longwave emissivity. The simulated cloud-top temperature is assigned a cloud-top pressure using a top-down approach matching to the local temperature profile from the MERRA data. The cloud type frequencies within the standard ISCCP pressure levels and optical thickness bins were determined and the resulting joint histograms are returned for each gridpoint for every time over the entire 25 years of processed data.

Finally, we perform a spatial-temporal matching of the simulator results to the observed ISCCP regime classifications. Composite histograms of the simulated MERRA clouds are generated for each weather state and compared with the observed ISCCP cloud properties. Although the clustering algorithm can be run independently on the simulated clouds (i.e., to determine the implicit distribution and general variability of cloud properties within the reanalysis), we instead employ the observational matching to

better investigate whether MERRA data produce the correct cloud types for the right locations at the right times.

3. Results

a. Evaluation of Simulated MERRA Cloud Regimes

Composite histograms of the MERRA simulated clouds corresponding to the times and locations of the ISCCP observations using a maximum-random vertical cloud overlap parameterization are shown in Fig. C-3. The images are interpreted similarly as the observed clusters (Fig. C-1), with the exception of the simulated regimes containing an extra bin for low values of optical thickness that are not detected by the processed ISCCP data. In addition, the upper-left bin in the observations represents a failure of the ISCCP algorithm to reconcile a cloud-top pressure for very thin clouds (often occurring for cirrus) and any such incidences are included in this bin.

The MERRA simulated regimes (Fig. C-3) qualitatively match the large-scale patterns of cloud properties demonstrated in the ISCCP observations (Fig. C-1). Although there are noticeable differences in the p_c-τ distributions between the simulated and observed regimes (e.g., optically thin, high clouds are missing from the MERRA simulation for all weather states), the simulated histograms of cloud-top pressure and optical thickness correctly predict the overall transitions among the observed weather states and successfully identify whether the regime is convectively active or suppressed. All of the simulated regimes significantly underpredict the observed CCF (Table C-1), consistent with Bosilovich et al. (2011) who found the global MERRA energy budget

contained weak cloud effects and an excess of shortwave radiation reaching the ocean surface due to either low cloud fractions and/or optical thickness.

The simulated deep convective regimes (WS1, WS2, and WS3) show a transition from WS1 containing the tallest and most optically thick clouds with a gradual transition to lower and thinner clouds for WS2 and WS3 (Figs. C-3a-c). There is a similar transition of simulated CCF with total cloud fractions of 35.5% for WS1 and decreasing to 26.4% for WS3. Although the simulated CCFs are well below the observed total cloud fractions (e.g., WS1 has nearly 100% CCF in the ISCCP observations due to the presence of extensive anvil and cirrostratus associated with this regime, Table C-1), the decreasing CCF from WS1 to WS3 is mostly consistent between the ISCCP observations and simulated MERRA clouds. The simulated cloud histograms also significantly under predict the presence of high clouds ($p_c < 310$ hPa) in addition to optically thick clouds ($\tau > 23$) for the deep convective weather states. As such, the simulated MERRA regimes struggle with resolving both high and optically thick clouds for WS1, WS2, and WS3, and predict too few clouds overall (i.e., low CCFs) compared to observations.

The comparison is least favorable for the simulated clouds occurring in those regions identified as WS4 (Fig. C-3d). The observed cloud characteristics of WS4 predominantly include thin cirrus at high heights with underlying low-level clouds (Fig. C-1d). As with WS1-WS3, much of the optically thin, high clouds are missing from the simulated MERRA populations comprising WS4. The simulated regime is somewhat bimodal, with cluster centroids appearing at mid-levels and moderate optical thickness (e.g., cumulus congestus) and a secondary maximum of low-level clouds with low

values of optical thickness that better matches the observed regime. The simulated regime again predicts too few clouds overall compared to observations for WS4 (16.6% and 74.8%, respectively), parallel with the results from WS1-WS3 (Table C-1).

The comparisons become more promising for the marine boundary layer clouds with the simulated cloud properties for WS5, WS6, and WS7 better matching the corresponding ISCCP observations. The MERRA clouds contain cluster centroids at low heights with low to moderate values of optical thickness (Figs. C-3e-g), consistent with ISCCP (Figs. C-1e-g). Transitions among the regimes show similar matching results, with WS5 containing a greater fraction of cloud-top heights between 800-600 hPa and more low-level clouds for WS6 and WS7. The simulated cloud fractions continue to under predict the observed CCF by 35-47% for these regimes (Table C-1). The trend in CCF between the simulated weather states is once more consistent with observations.

The cloud mixtures in WS8 contain the least difference between the MERRA data and ISCCP observations. The simulated MERRA clouds are clustered at low heights and optical thickness (Fig. C-3h), similar to observations. As with all previous regimes, the presence of thin, high clouds is underestimated in the simulation results, though the difference in CCF (24.1% and 17.1% for observations and MERRA, respectively) is relatively small and has the least error of the cloudy regimes. MERRA also does an excellent job with those regions identified as clear in the ISCCP observations, simulating only a few clouds (CCF of 3.0%) with low height and optical thickness throughout these domains (Fig. C-3i).

In an attempt to rectify the low values of cloud cover and CCF simulated using the reanalysis fields as input, we performed the same simulations with MERRA using a random vertical cloud overlap parameterization for both the convectively produced and large-scale condensate. The resulting composite histograms are shown in Fig. C-4.

The simulated regimes using random overlap are generally similar to those from the previous simulation (cf. Figs. C-3 and C-4) and correctly predict the transition of tall, thick clouds for the deep convective weather states to cluster centroids appearing at low-levels and thickness for WS5-WS8. As expected, the random overlap reduced the number of subgrid columns with vertically adjacent cloud mass levels and resulted in an increase in horizontal coverage and CCF. Differences in the CCF increased anywhere from 8.8% (WS4) to 16.5% (WS5). Consequently, the cluster mean optical depth decreased at the expense of the thickest clouds (e.g., those bins with $\tau > 23$), though this change helped fill-in the gap of the previously missing tall, thin clouds from the maximum-random simulation. The width of the cluster distributions also better matches the ISCCP observations using the random overlap assumption in addition to containing an improved representation of the cirrus regime (WS4). Nevertheless, the random overlap clouds still struggle to capture the presence of high clouds in WS1-WS4 and continue to under predict the observed total cloud fraction for each regime with the exception of WS8.

As previously mentioned in section 2, other empirical relationships were used to convert MERRA cloud and ice water mixing ratios to visible optical thickness based on more recent observations of tropical and subtropical clouds (e.g., Heymsfield et al.

2003). These sensitivity tests, however, produced composite histograms with even lower values of optical thickness and are not included in this study.

b. Trends in the Simulated Regimes

Trends in the cloud fractions for each p_c- τ bin were calculated for each weather state across the entire 25-yr of the simulated data in order to investigate any potential physical changes or erroneous shifts in the cloud distributions comprising each regime as an artifact of the evolving satellite radiances used in the MERRA data assimilation and product streams. Figs. C-5 and C-6 show the resulting trends (in % CCF decade^{-1}) for the maximum-random and random overlap parameterizations, respectively. Only those bins with statistical significance greater than 95% (p=0.05) are shown in the respective diagrams.

Most of the bins for the maximum-random overlap (Fig. C-5) have small values (trends less than ±0.1% decade^{-1}) and adjacent bins occasionally suffer from noise. There is a weak signal, however, indicating an overall shift towards larger values of optical thickness (i.e., negative trends for low τ values and increasing trends for moderate-to-high optical thickness) that are best detected for WS2, WS3, WS5, WS6, and WS7. Similar trends are evident for the random overlap parameterization (Fig. C-6), though the left-to-right shift in cloud optical thickness is more well-defined for each of the regimes. The sum of the individual significant bin trends is also indicated for each cluster, suggesting all of the cloudy regimes are becoming more cloudy with time in the maximum-random simulation (especially WS5, WS6, and WS7, Figs. C-5e-g) while

only regimes WS4-WS7 show any appreciable net gains in cloudiness throughout the random overlap simulation (Figs. C-6d-g).

The bins with the largest percent changes of CCF in Figs. C-5 and C-6 contain cloud-top pressure values greater than 680 hPa. The previous statement is particularly true for the marine boundary layer regimes (WS5, WS6, and WS7) and fair-weather cumulus clouds (WS8) in the random overlap simulation shown in Figs. C-6e-h. While this result is consistent with the expected notion of increased shortwave albedo and visible optical thickness as a result of increasing aerosol concentration attributed to anthropogenic activity (e.g., Twomey 1977), the GEOS-5 model uses a climatological aerosol distribution (Rienecker et al. 2011) and these particles are not directly accounted for in the moist physics schemes. It remains possible that the aerosol effect could modify the assimilated brightness temperatures and the corresponding retrievals of specific humidity (which do impact the moist physics parameterizations) though additional trend calculations over multiple periods of the same MERRA processing stream (i.e., years without any significant changes to the assimilated satellite radiances) would be necessary to confirm this hypothesis.

Similar trends along the vertical histogram axis (i.e., cloud-top pressure) are less evident, though there is a suggestion of the simulated cloud heights increasing with time for WS1 and WS3 in the random overlap simulation (Figs. C-6a, c). These changes are consistent with the fixed anvil temperature hypothesis proposed by Hartmann and Larson (2002) in which the level of convective outflow would increase over the period of record in conjunction with observed tropospheric warming. Although many of the

regimes contain positive trends in the upper-troposphere, most of the CCF changes are relatively small and do not occur alongside any corresponding regions of negative trends at low- or mid-levels. The stratocumulus regime (WS5) is the only weather state that has consistent (albeit weak) negative trends at upper-levels for nearly all optical thickness values, with a corresponding increase in the amount of low-level clouds in both the maximum-random and random overlap simulations (Figs. C-5e and C-6e). Given that WS5 predominantly occurs over the subtropical oceans (Fig. C-2e), the lowering of simulated cloud heights could be influenced by enhanced subsidence in the downward branch of the Hadley circulation. Stachnik and Schumacher (2011) found a statistically significant intensification of the Hadley cell in each hemisphere for the MERRA dataset from 1979-2008, which would partially help to explain this cloud result. Whether or not this trend is caused by physical mechanisms or again the result of a changing observation platform requires more evaluation, however, and is outside the scope of the current work.

c. Large-scale Environmental Conditions

To further investigate the driving forces behind the simulated MERRA clouds, we employ the same spatial-temporal matching of the ISCCP observations to the reanalysis data in order to generate regime-average profiles of the vertical velocity, temperature, and moisture for each weather state. The vertical velocity profiles and mean thermodynamic diagrams for each regime are shown in Figs. C-7 and C-8, respectively.

The vertical motions in MERRA match the expected patterns of the observed ISCCP cloud regimes. WS1 has the largest negative values (i.e., upward motion) of vertical velocity exceeding 100 hPa day^{-1} and peaks in the upper-troposphere near 400 hPa (Fig. C-7a). The profile for WS2 displays a similar shape (Fig. C-7b, note the difference in scale), though the overall magnitude is greatly reduced (~45 hPa day^{-1}) and occurs at a slightly higher level in the atmosphere (350 hPa). This transition is expected given the reduced rain rates for the observed ISCCP regimes (Lee et al. 2013) and the more stratiform nature and higher total diabatic heating center associated with WS2 (Stachnik et al. 2013). WS3 has a bottom-heavy velocity profile with upward motion estimates near 25 hPa day^{-1} throughout the 800-600 hPa layer (Fig. C-7c). WS4 also contains weak vertical motion throughout the entire troposphere, with enhanced ascent in excess of 10 hPa day^{-1} near 800 hPa and weaker rising peaking of about 5 hPa day^{-1} at 200 hPa (Fig C-7d). The composite vertical velocity profiles for WS3 and WS4 are again consistent with the observationally derived heating profiles for each regime (Stachnik et al. 2013).

The convectively suppressed regimes (WS5-WS8) demonstrate subsidence throughout most of the tropical and subtropical troposphere with only weak values of ascent (generally less than 5 hPa day^{-1}) near the surface (Figs. C-7e-h). The peak magnitude of the subsidence layer is similar (15-25 hPa day^{-1}) and occurs near 500 hPa for all the regimes. The clear weather state (WS0) has the largest values of downward motion, with peak values in excess of 30 hPa day^{-1} in the mid- and upper-troposphere. The MERRA vertical velocity profiles again match the observed diabatic heating

profiles in Stachnik et al. (2013) for WS5, WS6, and WS7, though the lack of upward motion for WS8 (a regime with weak low-level heating) suggests that MERRA may struggle with the effects of shallow convection and weakly precipitating systems.

The composite soundings for the MERRA data are shown in Fig. C-8. The temperature profiles generally follow that of a moist adiabat given the mostly tropical domain, though there are notable differences with low-level subsidence inversions for the convectively suppressed clouds (WS5-WS8, Figs. C-8e-h). The inversion strength weakens throughout the transition from the stratocumulus to cumulus regimes, and a similar surface-based temperature inversion appears for WS0 (Fig. C-8i), consistent with expectations for the clear weather state.

Fluctuations in the moisture profiles are more noticeable, with tropospheric and near-surface specific humidity decreasing from WS1 to WS4 (Figs. C-8a-d), with relatively dry conditions for WS0 (Fig. C-8i). Estimates of the MERRA low-level buoyancy align with the decreasing convective intensity of WS1, WS2, and WS3. Enhanced low-level moisture for WS1 results in a mean surface-based convective available potential energy (CAPE) in excess of 750 J kg^{-1} and tapers to approximately 300 J kg^{-1} for WS4 (note that several of the regimes have zero mean CAPE). The moisture profiles for the convectively suppressed regimes are much drier than WS1-4 and appear mostly similar (Figs. C-8e-h).

4. Summary and Discussion

This study created composite 2-D histograms of cloud-top pressure and optical thickness in MERRA data using an ISCCP simulator. Cloud simulations were performed using both a maximum-random and random vertical overlap assumption and the resulting cloud properties were highly dependent upon the choice of parameterization. Simulator results were composited using spatial and temporal matching to the observed ISCCP weather states in order to determine whether MERRA is able to reproduce the full population of observed tropical and subtropical clouds.

The simulated histograms of cloud-top pressure and optical thickness showed that the MERRA clouds qualitatively match the observed distributions from the 25 years of ISCCP data. The convectively active regimes (WS1, WS2, and WS3) contained cluster centroids with the greatest percentage of tall clouds and moderate-to-high values of optical thickness. Changes among the simulated regimes corresponded well to the observed ISCCP weather states, with reduced convective intensity (i.e., fewer thick, highs clouds) when transitioning from WS1 to WS3. Similar changes were identified for the total cloud cover, though the MERRA simulations produced a greater CCF for WS3 than for WS2, unlike the ISCCP observations.

Both simulations struggled with reproducing the tallest ($p_c < 310$ hPa) and most optically thick ($\tau > 23$) clouds. In addition, the maximum-random overlap simulation failed to produce many of the observed tall and thin clouds, though this error was improved when using the random cloud overlap for both convectively parameterized and large-scale condensate. As such, the simulator results significantly underestimated the

total cloud cover, with an average difference in CCF of 63% for the convective regimes using the maximum-random scheme. The average CCF difference decreased to 50% when using random overlap, though the improved results for WS1, WS2, and WS3 arose at the expense of simulating fewer clouds with larger values of optical thickness. The lower CCFs in MERRA are consistent with Bosilovich et al. (2011) who found the global MERRA energy budget contained weak cloud effects and an excess of shortwave radiation reaching the ocean surface due to either smaller than observed cloud optical effects. This finding is in agreement with Wu et al. (2012) who noted that other reanalyses also significantly underestimate cloud properties.

However, some of our results are in disagreement with a recent study by Posselt et al. (2012) who found that simulated MERRA clouds contained similar optical depth properties for deep convective elements ($\tau > 10$). Posselt et al. (2012) also noted that that MERRA clouds demonstrated a bias towards higher-than-observed cloud tops, again discrepant with our results. While Posselt et al. (2012) used the same subcolumn generator in COSP as in our study, direct comparisons are not possible as their analysis was limited to clouds with heights in excess of 10 km and used a cloud-top pressure definition based on optical thickness. Furthermore, the downward precipitation fluxes at each model level were considered in their analysis and the addition of the precipitating liquid and ice water masses could have a significant effect upon the resulting calculations of cloud optical depth. Finally, the Posselt et al. (2012) study was limited to the strong El Niño and La Niña events of 1998, a time when many reanalyses produce extremes in the tropical circulation (e.g., Stachnik and Schumacher 2011). An analysis

of the tropical MERRA precipitation data (not shown) indicates that DJF and JJA of 1998 contained the wettest and second driest seasonal precipitation averages, respectively, for the 25 years of MERRA data in this study. Consequently, the cloud properties identified in Posselt et al. (2012) may not be representative of the climatological population. Future work may examine the sensitivity of our results when limited to this period and the effects of incorporating precipitation fluxes into our simulator data.

The predominantly cirrus regime (WS4) was the least well simulated when compared to observations and many of the high-cloud tops were completely missing from the model results. As the ISCCP simulator uses an apparent infrared brightness temperature to assign cloud-top pressure, it remains possible that optically thin clouds with high tops are in fact present in the MERRA data. The occurrence of underlying low clouds (as is common for this regime) with greater optical depth (and infrared emissivity) could result in the higher cloud mass being aliased as a mid-level (i.e., warmer) feature. To test this hypothesis, we performed limited simulator experiments in which the cloud-tops remained unadjusted and were assigned the actual cloud-top pressure in the reanalysis (not shown). These results revealed two primary modes of cloud tops for WS4 (in addition to WS1, WS2, and WS3) with the histograms containing either mid-level ($440 < p_c < 560$ hPa) or upper-level ($p_c < 180$ hPa) clouds. The MERRA data thus contain cloud mass at upper-levels, though the simulator results should be subject to the same aliasing as any multi-layer clouds seen in the observations. This discrepancy could be explained by either MERRA producing too few or too little cloud

mass at upper-levels, or possibly too many multi-layer cloud scenes compared to observations. Our simulator results could also be an artifact of MERRA producing low-level clouds with optical thickness values (and infrared emissivity) greater than observed, though this possibility seems less likely given the good simulation of the low-level cloud regimes identified in this study. Nevertheless, future work should consider the representation of high-level clouds in MERRA (and multi-layer clouds) using other instrument simulators, including the Moderate Resolution Imaging Spectroradiometer (MODIS) and *CloudSat*, both of which are less sensitive to aliasing from the presence of low-level clouds (e.g., Bodas-Salcedo et al. 2011).

Comparisons of the simulated and observed regimes were favorable for the convectively suppressed weather states. The simulated MERRA clouds for WS5, WS6, and WS7 were clustered at low heights and optical thickness in addition to containing the correct cloud-top and cloud fraction trends as the ISCCP observations when transitioning among regimes. A similar model performance was noted for the cumulus regime (WS8) and the simulated clouds had the smallest difference in CCF compared to observations in part due to the convective organization of this regime (e.g., cloud streets, open and closed cells with significant cloud-free area). The simulator produced very few clouds in those regions identified as clear (WS0), indicating the MERRA does an excellent job of simulating large-scale, cloud-free regions.

Trends in the cloud histograms for the maximum-random overlap suggest an increase in cloud fraction for each regime over the 25 years of simulated data. Positive trends were only noted for WS4, WS5, WS6, and WS7 in the random overlap

simulation, with near zero or negative values for the remaining regimes. Both simulations indicated a shift toward more clouds of greater optical thickness. It remains unknown whether this result is a consequence of the changing satellite observations in the data assimilation system or identifies an actual physical change in the cloud climatology due to global warming or increased aerosol concentrations associated with anthropogenic activity.

Similar trends in the cloud-top pressure were less evident, though a lowering of the cloud-heights in the marine stratocumulus regime (WS5) was noted in the simulated MERRA data. This change is consistent with the increasing strength of the Hadley circulation in MERRA (Stachnik and Schumacher 2011) and the increasing subsidence in the downward branch would continue to suppress occasional tall clouds occurring within the stable layer. Zelinka et al. (2012) noted a similar increase in cloud-top pressure (i.e., descending heights) for shallow maritime clouds in response to global warming when using the ISCCP simulator with an ensemble of 11 GCMs, though these changes were better aligned with the regions identified as WS8 rather than the stratocumulus regime. Cloud heights may be increasing with time for WS1 and WS3, though the result was not consistent across both simulations. Regardless, the changing nature of the assimilated satellite radiances again complicates the attribution of any potential cloud-top height changes associated with the observed warming. Analysis over shorter periods with similar data assimilation are needed in order to test the robustness of this result or to determine whether cloud heights are increasing with time, following the fixed anvil temperature hypothesis of Hartmann and Larson (2002).

Finally, the composite profiles of MERRA vertical velocity, temperature, and moisture largely matched the expectations for each regime. The reanalysis vertical motion estimates followed the observed patterns of diabatic heating (Stachnik et al. 2013) with the exception of no low-level upward motion associated with the fair-weather cumulus regime (WS8). The above finding suggests that MERRA may struggle with reproducing the salient cloud properties that accompany shallow and boundary layer convection. The mean thermodynamic profiles were also consistent with expectations, suggesting that MERRA is capable of producing the correct cloud types at the observed locations at the correct times for the right reasons.

In conclusion, we find that NASA MERRA produces realistic sounding profiles and vertical velocity composites for each of the ISCCP weather states that match expectations and previous observations of tropical and subtropical cloud systems. The analysis within suggests that the MERRA reanalysis is properly primed for climate studies, though further refinement is needed on the representation and amount of clouds. Nonetheless, caution is advised when interpreting climate signals from reanalysis given the potential problems associated with energy and moisture budgets (e.g., Trenberth et al. 2011; Bosilovich et al. 2011) in MERRA and other datasets.

CHAPTER V

AN OBSERVATIONAL DECOMPOSITION AND MODEL RECONSTRUCTION OF CLOUDS AND PRECIPITATING SYSTEMS ASSOCIATED WITH THE HADLEY CIRCULATION

1. Introduction

The tropical Hadley circulation (HC) consists of an idealized zone of tropospheric ascent fueled by deep convection near the equator (e.g, Riehl and Malkus 1958; Riehl and Simpson 1979; Fierro et al. 2009), poleward flow aloft, large-scale subsidence in the subtropics, and a low-level return flow within each hemisphere. Tropics-wide observations (including satellite and large-scale, upper-air arrays), atmospheric general circulation models (GCMs), or numerical reanalysis are typically needed in order to successfully study the HC given the global nature of the phenomenon. Nevertheless, the previously listed datasets often indicate significant differences in HC climatology (e.g., Mitas and Clement 2005; Johanson and Fu 2009) and associated long-term climate trends throughout historical period of record (Hu and Fu 2007; Seidel and Randel 2007; Mantsis and Clement 2009).

The HC demonstrates a strong seasonality with a pair of nearly symmetric cells during the spring and autumn with a transition towards a dominant one-cell pattern in the solsticial seasons (e.g., Oort and Rasmusson 1970; Dima and Wallace 2003). The dominant "winter cell" contains rising motion in the summer hemisphere with a corresponding descent in the winter hemisphere, whereas the "summer cell" contains a

narrower region of weak overturning entirely within the summer hemisphere. Recent studies have focused on dynamical theories and the physical mechanisms responsible for potential long-term changes in HC intensity and width using observations and models (Lu et al. 2009; Kang and Polvani 2011, Polvani et al. 2011; Tandon et al. 2013; etc.), though similar theories concerning HC variability on interannual timescales remain less well understood. While previous work has documented that HC interannual variability is strongly dependent upon sea surface temperatures (SSTs) and El Niño-Southern Oscillation (ENSO) cycles (Oort and Yienger 1996; Quan et al. 2004; Ma and Li 2008; Stachnik and Schumacher 2011), others find significant non-ENSO variability and better attribute HC properties to changes in eddy momentum forcing or subtropical stability and the baroclinicity where extratropical wave fluxes begin to impinge upon the outward edges of the HC (e.g., Held 2000; Walker and Schneider 2006; Frierson et al. 2007; Caballero 2007; Lu et al. 2007, 2008; Korty and Schneider 2008). To add further complexity, the summer and winter cells may be differently affected by tropical diabatic heating and mid-latitude wave activity (e.g., Walker and Schneider 2006; Caballero 2007; Bordoni and Schneider 2010) and HC extremes in reanalysis data for the summer cell appear dependent on factors other than ENSO alone (Stachnik and Schumacher 2011).

Although the Hadley cell is defined as a zonal average, it is well known that global rainfall patterns demonstrate significant longitudinal variability. This study uses a phenomenological approach to dissect the global HC based on diabatic heating contributions from different satellite-observed cloud regimes (a proxy for dynamical

atmospheric regimes) from the International Satellite Cloud Climatology Project (ISCCP; Schiffer and Rossow 1983). While SST anomalies may adequately predict HC winter cell intensity on an interannual timescale, no studies currently exist that examine HC variability as a function of observed atmospheric cloud and precipitating systems. As such, we identify those years with the strongest meridional overturning from an ensemble of atmospheric reanalysis data and perform differencing based on frequency of occurrence of the ISCCP cloud regimes weighted by their average total diabatic heating profiles in order to determine the anomalous three-dimensional tropical and subtropical heating structures associated with HC extremes. In addition, a regional and phenomenological decomposition of the tropical circulation may help to elucidate the relative importance of precipitating systems in the deep tropics (i.e., related to dynamic scaling by diabatic forcing) versus those near the HC edges potentially associated with baroclinic eddies that may shape the HC subtropical terminus.

Finally, this study uses a GCM that is forced with the observed distribution of atmospheric diabatic heating derived from the ISCCP data to determine whether the large-scale tropical circulation can be recreated as a function of the ISCCP cloud and precipitating systems. Variations in the horizontal and vertical distributions of tropical and subtropical heating elicit different dynamical responses in numerical models at regional and global scales (e.g., Hartmann et al. 1984; Lin et al. 2004; Schumacher et al. 2004; Lappen and Schumacher 2012) and this work tests the feasibility of future model studies examining the sensitivities and large-scale response of select tropical and subtropical cloud regimes upon the global circulation.

2. Data and Methods

a. Reanalysis Datasets

Atmospheric reanalyses are used herein in place of observations to diagnose the three-dimensional structure and properties of the large-scale tropical circulation. This study comprises the wind and precipitation fields from eight reanalysis datasets including the Japan Meteorological Agency (JMA) 25-year Reanalysis Project (JRA) (Onogi et al. 2007), the European Centre for Medium-Range Weather Forecasts (ECMWF) 40-year Reanalysis (ERA40; Uppala 2005), ECMWF Interim Reanalysis (Dee and Uppala 2009), the National Centers for Environmental Prediction-National Center for Atmospheric Research (NCEP/NCAR) 40-year Reanalysis Project (Kalnay et al. 1996), the National Centers for Environmental Prediction-Department of Energy (NCEP/DOE) Reanalysis Project (Kanamitsu et al. 2002), the NCEP Climate Forecast System Reanalysis (CFSR; Saha et al. 2010), the National Aeronautics and Space Administration (NASA) Modern-Era Retrospective Analysis for Research and Applications (MERRA; Rienecker et al. 2011), and the National Oceanic and Atmospheric Administration-Cooperative Institute for Research in Environmental Sciences (NOAA/CIRES) Twentieth Century Reanalysis Version 2 (20CR; Compo et al. 2011). Details of each dataset are included in the above references. A complete evaluation of the HC mean state, interannual variability, and long-term trends for each reanalysis is presented in Stachnik and Schumacher (2011); this study focuses on the ensemble average results with occasional reference to the maximum and minimum values from the individual members as an estimate of the observed uncertainty.

The meridional mass streamfunction, Ψ, can be calculated at each pressure, p, and latitude, φ, as a function of the downward integrated meridional wind, v. The streamfunction form satisfying the two-dimensional, zonal mean continuity equation in spherical coordinates be expressed as

$$\Psi(p,\varphi) = \frac{2\pi a \cos(\varphi)}{g} \int_{p}^{p_s} [v(p,\varphi)] dp \,, \qquad \text{(V-1)}$$

where a is the planetary radius, g is the gravitational acceleration, and the brackets indicate a zonal average. Using the above streamfunction metric, several quantities can be derived from the latitude-pressure cross-sections in order to determine the average properties of the zonal average HC[1]. The maximum and minimum values in the northern and southern hemisphere (Ψ_N^* and Ψ_S^*, respectively) are commonly used to represent the overturning strength in both cells (e.g., Oort and Yienger 1996; Quan et al 2004; Caballero 2007) and correspond to a set of streamfunction pressure and latitude coordinates. The HC boundaries are defined as the first latitude poleward of the cell centers in which the 700-400 hPa average value of Ψ equals zero in each hemisphere, roughly consistent with the metrics used in previous studies (Frierson et al. 2007; Hu and Fu 2007; Lu et al. 2007, 2008; Johanson and Fu 2009). Finally, a corresponding total HC width ($\Delta\varphi$) can be defined as the difference between the northern and southern edges of the circulation.

[1] For brevity, we drop the term zonal average from our description and simply refer to the two-dimensional overturning as the Hadley circulation (HC) throughout the remainder of the text.

As previously stated, the analysis herein uses the HC metrics derived from an equally-weighted reanalysis ensemble average of the zonally-averaged meridional mass streamfunction (in lieu of a simple arithmetic mean) in order to better account for vertical variations in HC intensity among datasets. The corresponding annual average streamfunction for the 1984-2007 period is shown in Fig. D-1 and illustrates a pair of quasi-symmetric cells with a mutual boundary located slightly north of the equator in accordance with the annual mean position of the Intertropical Convergence Zone (ITCZ). The climatological boundaries of the HC and corresponding cell centers for the reanalysis ensemble are also included for reference. A complete discussion of the annual average HC (including seasonality in the reanalyses) is provided in Stachnik and Schumacher (2011).

b. ISCCP Cloud Regimes

Recent studies using observations from the ISCCP D1 dataset (Rossow and Schiffer 1999) have focused on regime sorting and the identification of physically meaningful and recurring mixtures of cloud types over specified latitude domains. The ISCCP cloud regimes or "weather states" (Jakob and Tseliodis 2003; Jakob et al. 2005; Rossow et al. 2005) use a *k*-means clustering algorithm (Anderburg 1973) in order to identify repeating patterns of cloud height and extinction covariance over a large area (2.5° x 2.5°) from individual satellite pixels of about 5 km in size. The extended low-latitude ISCCP dataset is available from the NASA Goddard Institute for Space Studies (ISCCP) website at http://isccp.giss.nasa.gov/etcluster.html. The regime classifications

include eight unique weather states (WS1-WS8) over the 35°N-35°S domain at 3-hr resolution for the entire 25-year period spanning from July 1983 – June 2008. Additional details of the retrieval algorithm and initial dataset are provided in Rossow et al. (2005). More recent studies examining the radiative, precipitation, and total diabatic heating characteristics of the tropical and subtropical weather states are described in Oreopoulos and Rossow (2011), Lee et al. (2013), and Stachnik et al. (2013).

The geographic distribution of the annual average, relative frequency of occurrence (RFO) for each weather state from 1984-2007 is shown in Fig. D-2. In addition, Fig. D-2 denotes the climatological HC boundaries and cell centers taken from the corresponding reanalyses. The ISCCP weather states include regimes with high cloud tops and large values of optical thickness describing tropical mesoscale convective systems (MCSs, WS1) and mixtures of less vigorous convection and cumulonimbus clouds (WS2) that are principally found along the ITCZ within the ascending branch of the HC (i.e., between the mutual boundary and cell centers shown in Figs. D-2a-b). WS3 represents a convectively active, though weaker regime, with populations of occasional deep convection and mid-level cumulus congestus clouds found throughout most of the tropics and subtropics (Fig. D-2c). The cluster regime describing optically thin, high clouds (WS4) is shown in Fig. D-2d and largely represents cirrus with underlying low-level cumulus clouds. WS5 and WS6 occur mainly over the eastern subtropical oceans in regions of relatively cold sea surface temperatures (SSTs) and correspond to marine boundary layer stratocumulus and stratus, respectively, with low cloud tops and low-to-moderate values of optical thickness (Figs. D-2e-f). A transition regime including

stratocumulus and cumulus (WS7) appears more widespread over the subtropical oceans in the descending branches of the HC (i.e., between the cell center and poleward terminus in each hemisphere), with some frequent occurrence along the tropical continental coasts (Fig. D-2g). Finally, WS8 represents fair-weather cumulus clouds that have the greatest RFO for all the ISCCP regimes (Fig. D-2h) and occur primarily in the descending branches of the HC with the notable exception of the tropical east Pacific and Atlantic Oceans. Areas may also be identified as a separate clear weather state (WS0) in the complete absence of clouds within the ISCCP domain, though this regime is relatively rare and occurs with an average RFO of less than 2.5% for the entire 1984-2007 period (not shown).

Previous studies have demonstrated that the ISCCP regimes have characteristic latent and radiative heating profiles in addition to containing distinctive thermodynamic environments and column vertical velocities (e.g., Jakob et al. 2005; Jakob and Schumacher 2008; Oreopoulos and Rossow 2011; Li et al. 2013; Stachnik and Schumacher 2013). The total diabatic heating profiles (i.e., the sum of the latent, radiative, and sensible heat fluxes from unresolved eddies following Yanai et al. 1973) for each of the extended low-latitude weather states is presented in Stachnik et al. (2013) and reproduced here for reference in Fig. D-3. The ISCCP weather states contain regimes with strong mid-tropospheric and upper-level heating (e.g., WS1, WS2, and WS3) from varying mixtures of deep convection and stratiform rain fractions, in addition to regimes with integrated cooling due to the dominant radiative properties of marine boundary layer clouds (WS5, WS6, and WS7). The remaining regimes (WS4 and WS8)

contain strong heating contributions from shallow cumulus clouds that are capable of enhancing low-level eddy sensible heat fluxes and redistributing heating with condensational warming at low-levels and cooling aloft due to detrainment and evaporation (e.g., Nitta and Esbensen 1974). A linear combination of the total heating profiles for each regime, weighted by the climatological (or anomalous) ISCCP RFOs, is used to determine the contributions to the total observed atmospheric heating that comprise the HC mean state and interannual variability.

c. Model Setup

A 24-year control simulation was performing using the Community Atmosphere Model version 4 (CAM4) as an atmospheric GCM that includes full-physics with a modified Zhang-McFarlane (1995) convective parameterization. Boundary layer physics follow Holtslag and Boville (1993) and a shallow convective scheme uses the methods of Hack (1994). The remainder of the model framework is identical to that used in Lappen and Schumacher (2012), with a horizontal resolution of 1.9° latitude x 2.5° longitude, 26 vertical levels, and a time step of 1800 s.

An additional simulation was performed using CAM4 in which the horizontal and vertical distributions of the ISCCP heating were used to force the GCM in order to determine whether the observed atmospheric heating can sufficiently reproduce the large-scale characteristics and interannual variability of the HC. The user-specified heating is directly implemented into the CAM4 simulation via the model physics package as a function of time and completely replaces the model-derived heating at each

time step (method described in Lappen and Schumacher 2012). We force the model with monthly average heating observations over the entire 24-years of the simulation and then evaluate the resulting dynamic circulation intensity and width, in addition to model precipitation. Both the CAM4 control and forced heating simulation use prescribed SSTs.

3. Observational Decomposition

a. Cloud Regimes associated with HC Extremes

From the 25 years of the reanalysis data, the top five periods (i.e., 20%) were identified with the strongest and weakest streamfunction magnitudes and the corresponding differences in the ISCCP average RFOs were calculated for each weather state. Given the strong seasonality of the HC (e.g., Dima and Wallace 2003), in addition to the expectation that the summer and winter hemisphere cells may be differently affected by tropical versus mid-latitude forcings (Walker and Schneider 2006; Caballero 2007; Bordoni and Schneider 2010; etc.), the analysis is repeated for both the northern hemisphere (NH) and southern hemisphere (SH) cells during DJF and JJA.

Differences in the frequency of occurrence for each of the ISCCP cloudy regimes are shown in Fig. D-4 for the times of HC extremes (strong-weak) for the NH dominant winter cell during DJF. As before, the reanalysis ensemble average NH cell boundaries and centers during this time of year are included on each panel. Although the difference fields are noisy and occasionally contain spurious changes in RFO along longitudinal bands due to issues with data quality (e.g., WS4 and WS8 near 60°-70°E in the central

Indian Ocean, Figs. D-4e, h), there is a pronounced change in the location of the convectively active weather states within the ascending branch of the NH cell. The years with the strongest average values of Ψ_N^* during DJF have a significant change in the RFO (in excess of 16%) for WS1, WS2, and WS3 with a longitudinal shift from the maritime continent towards the central and east Pacific (Figs. D-4a-c). The cirrus regime displays a similar west-to-east shift during strong NH winter cell events, though the latitudinal displacement occurs about 30° E of the convective regimes (Fig. D-4d). This shift relative to the convective weather states suggests that much of the ISCCP cirrus regime is produced through tropical anvil and blow-off from deep convection. The previous result is consistent with the expectation of weak upper-level westerlies associated with the Walker circulation and the advection of detrained cloud condensate downwind.

The increase in the convective weather states primarily comes the expense of the shallow cumulus (WS8, Fig D-4h). A west-to-east dipole in the change of RFO exists for WS8, with suppressed conditions leading to more instances of shallow convection and fair-weather cumulus over the tropical west Pacific, and fewer instances over the central and east Pacific Ocean where the otherwise shallow clouds are allowed to develop into mature, deep convection. WS7 (Fig. D-4g) displays a similar spatial pattern to the cumulus regime, though the change in RFO is smaller for this weather state. There is also an increase in stratocumulus type clouds (WS5) across the subtropical east Pacific in the descending branch of the northern cell, consistent with the enhanced subsidence expected with the stronger overturning circulations (Fig. D-4e). A similar increase in

WS5 is identified near the South American coastline along with a smaller southward displacement of the stratus regime (WS6) in the eastern tropical Pacific (Fig. D-4f). RFO changes elsewhere are relatively small and occur outside the domain of the NH cell.

The above tendencies in the cloud regimes appear to be dominated by the warm phase of ENSO, consistent with the previous work that found HC extremes typically occur during El Niño events (Oort and Yienger 1996; Quan et al. 2004; Ma and Li 2008). Subsetting the streamfunction values by the Climate Prediction Center (CPC) Ocean Niño Index (ONI) indicated that most of the strongest cells occurred during El Niño years, with less separation between the ENSO neutral and La Niña events (Stachnik and Schumacher 2011). Spatial correlations of the streamfunction magnitude (not shown) indicated the ENSO signal was robust across the entire 25 years of the ISCCP data. The RFO differencing was repeated for a subset of years considered ENSO neutral, though the overall results continued to show an eastward shift (albeit weaker) in the location and magnitude of the deep convective weather state anomalies across the equatorial Pacific (not shown).

Fig. D-5 shows the analogous differences in the ISCCP RFOs for the SH dominant winter cell during JJA. Despite the ENSO SST anomalies being minimized during the austral winter, there is once again an eastward shift in the locations of the convective weather states with generally fewer instances over the Indian Ocean and maritime continent and increasing amounts throughout the upward branch of the southern cell across the entire Pacific (Figs. D-5a-d). The maximum increase in RFO is again nearly equal (~10%) for WS1, WS2, and WS3, suggesting no particular regime is

preferred during HC extremes. The exchange of deep convection and suppressed clouds once more appears linked to WS8 (Fig. D-5h). The increase in the RFOs appear much more focused than the general eastward shift in the NH DJF case, suggesting at least part of the stronger overturning is simply attributed to larger vertical mass fluxes associated with a stronger and more well defined ITCZ. Positive anomalies are also identified across the South Pacific Convergence Zone for WS3 (Fig. D-5c). There are also slight increases in the RFO of the marine boundary layer clouds (WS5 and WS7) within the descending branch across the subtropical oceans (Figs. D-5e, g), potentially attributed to enhanced subsidence associated with the stronger overturning as in the NH cell during DJF.

Changes in the ISCCP RFOs corresponding to the NH summer (weak) cell extremes during JJA are shown in Fig. D-6. Although the absolute changes in the RFO are smaller than in the corresponding winter cells (note the contour scale in Fig. D-6 differs from Figs. D-4 and D-5), changes in the cloud distributions across the Pacific Ocean again appear to be a major source of variability associated with the Ψ_N^* extremes. There is a positive band of anomalies for WS1, WS2, and WS3 stretching across the Pacific Ocean centered between 10-15°N with a corresponding negative anomaly located near 5°N. These north-to-south dipoles suggest that a northward shift in the Pacific ITCZ is chiefly responsible for the enhanced overturning. Assuming the latitude of the subtropical terminus does not change, the NH cell strength would be directly linked to the displacement of the ITCZ (i.e., a narrower cell should have stronger overturning due to conservation of mass). Spatial correlations of the ISCCP RFOs and Ψ_N^* during JJA

indicate that the northward positive anomalies were statistically significant (p=0.05) for the entire time series, though most of the negative anomalies (with the exception of the WS3 in the fast east Pacific) were not as robust (not shown).

There are also positive convective nomalies near or within the NH ascending branch along the Indian subcontinent and southeast Asia (in addition to central Africa), coincident with those areas affected by summertime monsoons (Figs. D-6a-c). Although the RFO changes during the extreme events indicate that a stronger monsoon (i.e., enhanced presence of WS1, WS2, and WS3) contributes to a stronger summer hemisphere HC and is consistent with previous work (e.g., Trenberth et al. 2000; Dima and Wallace 2003), the result was also not statistically significant when considered for the entire 25-yr period. Changes in the matching RFOs for the SH summer (weak) cell during DJF indicated a stronger influence of the Australian monsoon (not shown), with a statistically significant correlation and increase in WS1, WS2, and WS3 over northern Australia within the ascending branch of the southern cell.

b. Anomalous Tropical and Subtropical Heating

While the previous analysis demonstrates linkages between certain weather states and HC extremes, it does not directly assign attribution nor determine which cloud regimes are most important for controlling HC interannual variability. As such, we multiply the anomalous frequency of occurrence for each weather state by the corresponding heating profiles presented in Fig. D-3 and perform a linear combination for all regimes in order to examine the three-dimensional structure of the total

atmospheric heating anomalies associated with HC extremes. Longitudinal profiles of the anomalous vertical heating structure within the ascending branch of each cell (in addition to a representative mid-level cross-section at 600 hPa) are shown for the winter and summer hemispheric cells in Figs. D-7 and D-8, respectively.

The NH winter (dominant) cell contains maximum total heating differences in excess of 1.25 K day^{-1} over the central Pacific Ocean at 500-400 hPa with a corresponding cooling anomaly of -0.75 K day^{-1} above the maritime continent (Fig. D-7a). The changes in the distribution of mid- and upper-level heating are also consistent with the expected longitudinal shifts for El Niño events. The heating anomalies stretch towards the east Pacific at upper-levels, though the average heating within the entire ascending branch at low-levels only extends to about 120°W. Plots of the average heating differences for individual regimes indicate that heating anomalies at low-levels are primarily caused by WS3 (not shown). Likewise, the total heating differences at mid- and upper-levels are almost entirely attributed to the increased frequency of WS1 (e.g., Fig. D-4a), with much smaller contributions from the WS2 heating. Despite WS1 having an overall low average RFO across the entire 35°N-35°S domain (less than 6%, Fig. D-2a), the changes in this weather state contribute the greatest amount towards the total diabatic heating anomalies and WS1 likely exhibits the greatest control on the interannual variability of the NH winter Hadley cell. Anomalous heating and cooling centers are also located over eastern equatorial Africa and South America (Fig. D-7c), respectively, again attributed to the RFO changes for WS1 (Fig. D-4a).

The SH winter (dominant) cell shows a stronger increase in the total heating difference at low-levels in the equatorial east Pacific (Fig. D-7b), with the total difference arising from an increase in WS3 and corresponding decrease in WS5 and WS6 in these regions (Figs. D-5c, e-f). The average heating differences within the ascending branch exceed 0.5 K day^{-1} across the Pacific Ocean at 500-400 hPa (Fig. D-7b), again suggesting that the heating from an enhanced ITCZ is the main driver behind SH winter cell extremes. WS1 once more contributes the greatest amount towards the enhanced heating (upwards of 0.5 K day^{-1} across much of the ITCZ) with somewhat smaller contributions (less than 0.25 K day^{-1}) from WS3 (not shown). Heating differences from WS2 were relatively small despite their near-equal increase in RFO (Fig. D-5b). The increase in WS3 over the SPCZ region (Fig. D-5c) did not appear to affect the total heating (Fig. D-7d), as its contributions were mostly balanced by negative heating differences from other regimes during stronger HC events.

The heating differences for the summer hemisphere (weak) cells are less pronounced than the corresponding winter season (note the different scales for Figs. D-7 and D-8). Heating differences for the NH summer cell are again mostly limited to the east Pacific at low-levels (Fig. D-8a) and comprise anomalies from WS3 and WS6 (not shown), with additional low-level heating near 60°E. The northward shift in the ITCZ and convective regimes (Fig. D-6) appears throughout the entire Pacific at 600 hPa (Fig. D-8c), with positive heating differences ranging from 0.1-0.4 K day^{-1}. As before, the heating differences arise primarily from increases in WS1, with smaller contributions (becoming more important in the east Pacific) from WS3 (not shown). WS2 reinforces

the overall pattern of convective heating anomalies, though it once again contains weak magnitudes for the heating differences associated with NH summer cell extremes. Heating differences over the monsoon regions (Fig. D-8c) have weak positive contributions at both low- and mid-levels, though the overall magnitude is generally the same as the observed heating differences across the Pacific Ocean associated with the northward shift of the ITCZ.

The SH summer cell heating differences suggest the strength of the north Australian monsoon affects the resulting HC interannual variability with total heating anomalies of 0.4-0.5 K day^{-1} at mid-levels associated with the cell extremes (Figs D-8b, d). There are also strong heating differences over the eastern Pacific along and north of the equator from the increased fractions of WS1 and WS3 at both low- and mid-levels (e.g., Fig. D-8d). Although this difference occurs within the ascending branch of the northern cell using the HC boundaries in this study, it nevertheless aligns with the expected position of the ITCZ during DJF (i.e., the true boundary between the NH and SH cells) and would thus contribute to the meridional overturning in the southern cell. These results highlight a potential shortcoming of using the zonally-averaged HC metrics when discussing clouds and precipitating systems that demonstrate significant longitudinal variability. The subtropical Atlantic Ocean also contains cooling anomalies of 0.3 K day^{-1} at both low and mid-levels for regions located south of the equator. There is also an anomalously strong region of positive heating differences located off the west coast of South America, though these differences are likely related to the ISCCP data

quality and uncertainties in the regime classifications for the extreme years as the heating difference was not statistically significant for the entire time series.

4. Model Reconstruction

Sensitivities of the large-scale response to tropical and subtropical heating were evaluated by computing HC metrics for a CAM4 control simulation (CAM4-CTRL) and an additional CAM4 simulation forced with the observed three-dimensional atmospheric heating from the ISCCP observations (ISCCP-CTRL). The resulting annual average, zonal mean streamfunction is shown for each simulation in Fig. D-9, along with a reproduction of the reanalysis ensemble HC as shown in Fig. D-1.

Overall, the CAM4-CTRL simulation (Fig. D-9a) closely matches the reanalysis ensemble (Fig. D-9c) with the model producing a similar HC vertical structure, intensity, and width as previously identified in the reanalyses. ISCCP-CTRL (Fig. D-9b) creates a mean circulation that is too strong in each hemisphere compared to the reanalysis ensemble. The CAM4-CTRL and ISCCP-CTRL simulations have similar locations for the mutual boundary between the NH and SH cells (i.e., the mean position of the ITCZ), though ISCCP-CTRL produces a subtropical terminus in each hemisphere that extends beyond the reanalysis, especially in the NH. The stronger circulation in ISCCP-CTRL is somewhat surprising as the positive differences in the ISCCP-derived and CAM4 heating maximize in the subtropics (Stachnik et al. 2013), suggesting a weakening of the low-latitude heating gradient. As such, the additional heating might be thought to reduce the circulation strength and interfere with the large-scale subsidence in the subtropics,

though the overall finding of a stronger circulation is consistent with the notion of adding extra energy to the modeled atmosphere.

Time series of the annual average streamfunction intensity for each hemisphere (Ψ_N^* and Ψ_S^*) and HC total width ($\Delta\varphi$) for the CAM4-CTRL and ISCCP-CTRL simulations are shown in Fig. D-10, along with the reanalysis ensemble average. The shading indicates the range of uncertainty in each variable from individual reanalyses. As with the 24-yr mean state, the HC intensity from CAM-CTRL matches the reanalysis ensemble within each hemisphere (Figs. D-10a-b). Likewise, the ISCCP-CTRL simulation overpredicts the range of streamfunction values identified from the reanalyses, with the exception of during 1998-2001 when the ERA40 produced excessively strong values of the tropical circulation (e.g., Stachnik and Schumacher 2011). The range of interannual variability for HC intensity is slightly smaller in CAM4-CTRL than the reanalyses, with larger fluctuations for the ISCCP-CTRL simulation. Differences in the HC width between the model simulations are less pronounced than the circulation intensity (Fig. D-10c), though ISCCP-CTRL again overestimates the tropical width throughout nearly the entire period when compared to the reanalyses.

The ISCCP-CTRL simulation does show some improvements over CAM4-CTRL, however, with a circulation center for the southern cell occurring lower in the atmosphere that is more in line with the reanalyses (Fig. D-11a). This improvement is likely attributed to the use of satellites and other observations over the tropical oceans that constrain the reanalysis data, whereas the CAM4-CTRL simulation is entirely dependent upon the underlying convective parameterizations. Although the total amount

of mass transport in the HC is identical for similar values of the streamfunction magnitude regardless of the circulation height, the ability to simulate the correct circulation center could have a significant influence on the GCM estimates of cross-equatorial water vapor transport as done for reanalyses (e.g., Cohen et al. 2000; Sohn and Park 2010).

ISCCP-CTRL also outperforms the CAM4-CTRL simulation at reproducing the observed values of low-latitude precipitation (Fig. D-11b). All of the reanalyses and CAM4-CTRL overestimate tropical precipitation relative to the Global Precipitation Climatology Project (GPCP; Adler et al. 2003) dataset, with zonal average precipitation rate errors approaching 3.5 mm day^{-1} in certain datasets (Stachnik and Schumacher 2011). The ISCCP-CTRL simulation produces similar precipitation results as CAM4-CTRL in the ascending branch of the HC (occasionally better) with more noticeable improvements in the descending branch in each hemisphere (not shown). As such, ISCCP-CTRL produced a better overall representation of the HC precipitation when forcing the model with the observed atmospheric heating.

Trends in the annual average HC intensity in each hemisphere, total width, and precipitation from each simulation and the reanalysis ensemble are summarized in Table D-1. Although the reanalyses indicate a strengthening of the HC in each hemisphere (0.37×10^{10} kg s^{-1} $decade^{-1}$ and -0.23×10^{10} kg s^{-1} $decade^{-1}$ for the NH and SH, respectively), the CAM4-CTRL results suggest almost no trend in either hemisphere over the 24-yr period. This result is consistent with previous studies, as Mitas and Clement (2005, 2006) showed that intensification trends found in reanalyses are often

much weaker or completely absent from GCM simulations. The ISCCP-CTRL trends indicate a somewhat stronger intensification in the SH (-0.13 x 10^{10} kg s^{-1} $decade^{-1}$) that more closely resembles the reanalyses, although the NH cell trend suggests a weakening of the circulation strength unlike the reanalysis ensemble (all but one member indicates a moderate-to-strong intensification during this time).

Both simulations also predict a moderate narrowing of the tropical circulation (-0.62° latitude $decade^{-1}$ and -0.31° latitude $decade^{-1}$ for CAM4-CTRL and ISCCP-CTRL, respectively) whereas the reanalysis ensemble indicates a statistically significant widening of 1.12° latitude $decade^{-1}$. This result is consistent with the discrepancies in widening trends between reanalyses and GCMs presented in Johanson and Fu (2009), though they found weak positive trends for their model simulations unlike the narrowing trends identified in our results. The HC precipitation trends from CAM4-CTRL and ISCCP-CTRL are near-zero and agree well with the GPCP observations.

5. Summary and Discussion

Previous studies of Hadley cell interannual variability relied on large-scale correlations of HC streamfunction magnitude and tropical SSTs, in addition to idealized numerical model experiments. This study is the first to diagnose HC variability and extremes as a function of observed atmospheric clouds and precipitating systems. The zonally-averaged meridional mass streamfunction was calculated from an ensemble of atmospheric reanalyses and used to identify those periods with maximum or minimum overturning in the mean meridional circulation. Although the HC metric in this study

represents a zonal average, we attempt a phenomenological and regional decomposition of the clouds and precipitating systems comprising the mean meridional circulation into its mesoscale components by matching independent observations of cloud mixtures from the ISCCP weather state dataset to the reanalysis streamfunctions.

Differences in the ISCCP weather states between strong and weak HC events typically occurred over oceanic domains, with the largest differences usually located over the Pacific Ocean. The northern hemispheric cell reached its peak intensity during El Niño events, with a corresponding eastward shift in the location of the deep convective weather states (WS1, WS2, and WS3) from the western Pacific and maritime continent to the central and east Pacific Ocean. Changes in the cirrus regime (WS4) mimicked the patterns of WS1, WS2, and WS3, though the maximum shift occurred about 30°E of the deep convective weather states, suggesting that the tropical ISCCP cirrus clouds are primarily generated from convective anvil blow-off caused by weak upper-level westerlies associated with the Walker circulation. Changes in the deep convective weather states were at the expense of the fair-weather cumulus regime (WS8) and the overall enhancements to the NH winter cell intensity were largely consistent with previous studies correlating HC activity to tropical SSTs (e.g., Oort and Yienger 1996; Quan et al. 2004; Ma and Li 2008) and other work linking variations in Pacific SST to anomalous low-latitude atmospheric circulations (e.g., Giese and Carton 1999). A similar response was identified when taking differences between strong and weak overturning events from a subset of those years considered ENSO neutral using the CPC Ocean Niño Index.

Other modes of variability were discovered for the SH winter cell and the summer cell in each hemisphere. A stronger ITCZ with additional vertical mass flux (i.e., positive differences in the RFOs for WS1, WS2, and WS3) was associated with greater overturning years for the SH summer cell in JJA. Likewise, a northward shift in the ITCZ during the boreal summer appears to be related to the maximum overturning intensity for the NH summer cell. This mechanism was explained by the possibility of an enhanced circulation resulting from conservation of mass and a narrowing of the NH cell under the assumption that the subtropical terminus does not change. Reasons behind the latitudinal shift were not provided, though it remains possible that added heating and stronger radiative fluxes in the northern extratropics may result in the ITCZ shifting towards the hemisphere with the most positive differential surface heating (Kang et al. 2009). As such, it cannot be directly determined from the ISCCP observations alone whether the HC extremes for the NH cell during JJA are controlled primarily by tropical diabatic forcing and angular momentum conservation (Held and Hou 1980) or influences from higher latitudes (e.g., Walker and Schneider 2006; Caballero 2007; Korty and Schneider 2007; Lu et al. 2007, 2008). The Indian and southeast Asian monsoons may also affect HC extremes (e.g., Trenberth et al. 2000; Dima and Wallace 2003), though the changes in the deep convective weather states were relatively small and not always statistically significant. The Australian monsoon, however, may play a more significant role in the magnitude of the SH summer cell and demonstrated greater changes in connection to HC intensity extremes.

Although none of the convective regimes seem preferred during strong overturning events (i.e., the increase in RFO was similar for WS1, WS2, and WS3), scaling by the mean vertical diabatic heating profile for each regime indicated that WS1 contributed the greatest amount towards the total anomalous heating associated with stronger overturning. As such, the most vigorous deep convective weather state that comprises tall and widespread optically thick clouds with regime average precipitation rates of 19 mm day^{-1} (Lee et al. 2013) appears to exhibit the greatest control on HC interannual variability, despite having an overall low RFO. The more frequent WS3 (i.e., a mix of cumulus congestus and deeper convective clouds but with less mesoscale organization) also played a contributing role, especially at low-levels and over the eastern Pacific Ocean. This mode of enhanced heating and convection may indicate a similar interannual variability of the shallow overturning circulation identified in this region by Zhang et al. (2004). Additional work is needed with the mean ISCCP cloud properties in order to evaluate this hypothesis and determine whether the WS3 cloud tops in the east Pacific match that of the circulation height identified in Zhang et al. (2004).

A linear combination of the ISCCP heating profiles, weighted by their frequency of occurrence, was used to produce an observationally-derived estimate of the three-dimensional atmospheric total diabatic heating. The HC resulting from a GCM forced by the ISCCP heating distributions was generally too strong and wide compared to the reanalysis ensemble. The use of observations to force the model did lead to some improvements compared to a control run of CAM4, however, with a lower circulation

center for the southern hemispheric cell that better matched the reanalyses and overall reduced HC precipitation that agreed with the GPCP dataset. Long-term HC trends from the CAM4 control simulation did not match the reanalysis (consistent with previous studies), while the simulation forced by the ISCCP heating showed improvement in all categories except for the NH cell intensity.

An implicit assumption in combining the reanalyses and satellite datasets is that the dynamic fields in the reanalysis output are in fact somehow affected by the observed cloud feedbacks and the diabatic heating from the ISCCP weather states (i.e., are reanalysis reproducing the observed HC interannual variability for the right reasons). Although many reanalyses do not have closed energy and moisture budgets (e.g., Trenberth et al. 2011; Bosilovich et al. 2011), a recent study by Stachnik and Schumacher (2013) suggests that the NASA MERRA reanalysis qualitatively matches the observed distributions of cloud-top pressure and optical thickness values using an ISCCP simulator (Klein and Jakob 1999; Webb et al. 2001). The proper representation (or lack thereof) of clouds in reanalyses may be paramount to understanding differences in the climatological representation of the tropical HC or long-term trends in the multi-reanalysis ensemble (e.g., Song and Zhang 2007). As such, the MERRA data may be suitable for use in long-term climate trend studies in addition to examining HC mean-state and interannual variability.

Future work will continue to address the model sensitivities and upscale feedbacks of the heating associated with ISCCP weather states upon the large-scale tropical circulation. Additional simulations forced with observed heating profiles from

specific weather states (e.g., shallow or deep convection) or regional domains (tropics versus subtropics, land versus ocean) may be useful in isolating the dynamic effects of individual cloud regimes over distinct locations. For example, the effects of additive heating from strong NH monsoons can be sequestered in the model to determine their effect on enhancing or suppressing the summer Hadley cell. Additional simulations may test the HC sensitivity to the location of the tropical Pacific heating, consistent with the notion that east Pacific and central Pacific El Niño events may produce a different large-scale atmospheric response (e.g., Feng and Li 2013).

Finally, we are particularly interested in applying the above methods to examine the shallow cumulus humidity throttle proposed by Neggers et al. (2007). The moisture hypothesis indicates the presence of a negative feedback on the tropical climate in which enhanced subtropical shallow convection results in more humid air feeding into the ITCZ. The stronger ITCZ creates enhanced vertical mass fluxes in the deep tropics with compensating subtropical subsidence that suppresses new subtropical convection. Future implementation of the different amounts of observed low-level subtropical heating into CAM4 can produce meaningful results in order to better realize the potential connections between tropical and subtropical clouds and climate.

CHAPTER VI

SUMMARY AND CONCLUSIONS

Previous studies using reanalysis data suggest an intensification and poleward expansion of the tropical Hadley circulation (HC) throughout the twentieth century, yet the HC climatology and trends were undocumented for many of the newest reanalyses. This dissertation presented an intercomparison of eight reanalyses to better elucidate the mean-state variability and trends concerning HC intensity and width. Significant variability between reanalyses was found in the mean HC intensity, with less variability in HC width. Certain reanalyses [e.g., European Centre for Medium-Range Weather Forecasts (ECMWF) 40-year Reanalysis (ERA40) and Climate Forecast System Reanalysis (CFSR)] tend to produce stronger meridional overturning while others [National Centers for Environment Prediction-National Center for Atmospheric Research (NCEP/NCAR) and National Aeronautics and Space Administration (NASA) Modern-Era Retrospective Analysis for Research and Applications (MERRA)] are constantly weaker. The National Oceanic and Atmospheric Administration-Cooperative Institute for Research in Environmental Studies (NOAA/CIRES) Twentieth Century reanalysis best matched the ensemble averages with the exception of a poleward shift in the subtropical terminus.

Ensemble trends regarding HC intensity and width are broadly consistent with previous work indicating a 0.40 (0.07) x 10^{10} kg s^{-1} $decade^{-1}$ intensification in the northern (southern) cell and a 1.1° $decade^{-1}$ widening in the past 30 years, though some

uncertainty remains regarding the intensity of the southern cell. Longer term ensemble trends (i.e., 1958-2008) containing fewer ensemble members suggest a weaker northern cell intensification but stronger southern cell intensification and a more modest widening of the HC (i.e., 0.53° decade^{-1}) compared to the last 30 years. Separation of the seasonally averaged streamfunction magnitudes by El Niño-Southern Oscillation (ENSO) phase revealed a weak clustering and statistically significant strengthening of the mean circulation for El Niño compared to ENSO neutral and La Niña events for the winter cell, with little difference in the summer cell intensity.

Composite profiles of the apparent heat source (Q_1) and moisture sink (Q_2) were calculated for the International Satellite Cloud Climatology Project (ISCCP) cloud regimes or "weather states" using sounding observations from 10 field campaigns comprising both tropical and subtropical domains. Distinct heating profiles were determined for each ISCCP cloud regime, ranging from strong, upper-tropospheric heating for mesoscale convective systems (WS1) to integrated cooling for populations typically associated with marine stratus and stratocumulus clouds (WS5, WS6, and WS7). Despite being primarily associated with thin cirrus, the corresponding regime (WS4) has heating maxima in the lower and mid-troposphere due to the presence of underlying clouds. Regime averaged Q_2 profiles showed similar transitions with strong drying observed for deep convection and low-level moistening for marine boundary layer clouds. The derived profiles were generally similar over land and ocean with the notable exception of the fair-weather cumulus regime (WS8). Additional mid-level

moistening was identified for several weather states over land, suggesting enhanced detrainment and more frequent congestus clouds compared to oceanic domains.

A control simulation using the Community Atmosphere Model version 4 (CAM4) was similar to the large-scale patterns of diabatic heating at low-levels produced by the ISCCP composites. Differences were more pronounced at mid- and upper-levels and were largely attributed to the uncertainty in the heating profiles for the cumulus regime (WS8). Low-level heating anomalies were also calculated for each phase of the Madden-Julian Oscillation (MJO) and precede upper-tropospheric heating from deep convection by 3 to 4 phases.

An instrument simulator was also used to compare low-latitude cloud properties from NASA MERRA with ISCCP observations. Composite histograms of simulated cloud-top pressure (p_c) and optical thickness (τ) were generated from 25 years of reanalysis data for each of the observed ISCCP cloud regimes. The simulated MERRA clouds qualitatively match the observed distributions of cloud-top pressure and optical thickness. The convectively active regimes contained simulated clouds with tall heights and moderate thickness, though the tallest ($p_c < 310$ hPa) and thickest ($\tau > 23$) clouds were missing from the reanalysis. The presence of tall, thin clouds was also unaccounted for in the simulated regimes, though this result was partially improved when using a random vertical cloud overlap parameterization. The convectively suppressed regimes were simulated well in MERRA. However, the reanalysis significantly underpredicted the observed cloud fractions for all the regimes, consistent with previous evaluations of MERRA energy and moisture budgets and cloud properties in other reanalyses.

Trends in the MERRA cloud property histograms suggest an increase in optically thick clouds with overall increasing cloudiness. Cloud-top pressure trends were less evident with only a weak suggestion of lowering heights for the stratocumulus regime. Some of the deep convective cloud regimes may be growing taller in response to observed global warming, though this result was only identified in one of the simulations and it remains unknown whether these shifts are related to changes in the observational retrievals or physical climate trends. Composite profiles of MERRA vertical velocity, temperature, and moisture for each ISCCP regime largely matched expectations and observations from previous studies, suggesting that the dynamic and thermodynamic properties of the cloud regimes are well captured by the reanalysis even if the simulated cloud properties do no fully align with ISCCP observations.

Finally, this study examined HC interannual variability as a function of the observed frequency of tropical and subtropical cloud regimes using the ISCCP dataset. HC metrics were derived from the reanalysis ensemble and the corresponding strongest and weakest overturning events were identified for each hemisphere during the summer and winter seasons. Differences in the matching cloud regimes relative frequency of occurrence (RFO) suggest that the northern hemisphere winter cell is dominated by an El Niño response in the central Pacific Ocean. Other mechanisms for HC intensity change included the intensity and position of the Pacific ITCZ, though the monsoons may play a minor role in altering HC strength.

The anomalous ISCCP RFOs during HC extremes were scaled by the regime-average vertical heating profiles from the earlier work based on a sounding-derived

look-up table in order to determine which cloud mixtures contribute the most towards the anomalous diabatic heating. Although the RFO changes for the three deep convective weather states were similar, the regime describing the most vigorous and organized convection appears to be most important for HC extremes, despite an overall low frequency of occurrence. When used to force an idealized GCM, the three-dimensional heating reconstruction using the ISCCP data produced too strong a HC. However, the forced heating simulation demonstrated some improvement in HC precipitation and the representation of the southern hemispheric cell.

This research has set the stage for a variety of additional low-latitude climate studies. The large-scale circulation is sensitive to the horizontal and vertical distribution of tropical and subtropical heating (e.g., Hartmann et al. 1984; Lin et al. 2004; Schumacher et al. 2004; Lappen and Schumacher 2012) and the three-dimensional heating fields derived for the phases of the MJO provide a new observational constraint for GCMs testing MJO initiation and maintenance hypotheses. Likewise, future work will continue to address the model sensitivities and upscale feedbacks of regional cloud variations upon the large-scale HC. Improved knowledge of these upscale feedbacks and mesoscale-climate interactions may help lead towards improved and/or unified theories of HC dynamics in addition to a better understanding of the HC behavior in present and future climates.

REFERENCES

Adler, R. F., and coauthors, 2003: The version 2 global precipitation climatology project (GPCP) monthly precipitation analysis (1979-present). *J. Hydrometeor.*, **4**, 1147-1167.

Anderberg, M. R., 1973: *Cluster Analysis for Applications*. Academic Press, 359 pp. New York, NY, USA.

Bacmeister, J. T., M. J. Suarez, and F. R. Robertson, 2006: Rain reevaporation, boundary layer–convection interactions, and Pacific rainfall patterns in an AGCM. *J. Atmos. Sci.*, **63**, 3383-3403.

Bengtsson, L., S. Hagemann, and K. I. Hodges, 2004: Can climate trends be calculated from reanalysis data? *J. Geophys. Res.*,**109**, D11111, doi:10.1029/2004JD004536.

Birner, T., 2010: Recent widening of the tropical belt from global tropopause statistics: Sensitivities. *J. Geophys. Res.*, **115**, D23109, doi:10.1029/2010JD014664.

Bodas-Salcedo, and coauthors, 2011: COSP: Satellite simulation software for model assessment. *Bull. Amer. Meteor. Soc.*, **92**, 1023-1043.

Bordoni, S., and T. Schneider, 2010: Regime transitions of steady and time-dependent Hadley circulations: Comparison of axisymmetric and eddy-permitting simulations. *J. Atmos. Sci.*, **67**, 1643-1654.

Bosilovich, M. G., J. Chen, F. R. Robertson, and R. F. Adler, 2008: Evaluation of global precipitation in reanalyses *J. Appl. Meteor. Climatol.*, **47**, 2279-2299.

----------, F. R. Robertson, and J. Chen, 2011: Global energy and water budgets in MERRA. *J. Climate*, **24**, 5721-5739.

Caballero, R., 2007: Role of eddies in the interannual variability of Hadley cell strength. *Geophys. Res. Lett.*, **34**, L2275, doi:10.1029/2007GL030971.

Casey, S. P. F., A. E. Dessler, and C. Schumacher, 2007: Frequency of tropical precipitating clouds as observed by the Tropical Rainfall Measuring Mission Precipitation Radar and ICESat/Geoscience Laser Altimeter System. *J. Geophys. Res.*, **112**, D14215, doi:10.1029/2007JD008468.

Chan, S. C., and S. Nigam, 2009: Residual diagnoses of diabatic heating from ERA-40 and NCEP reanalyses: Intercomparisons with TRMM. *J. Climate*, **22**, 414-428.

Chen, J., B. E. Carlson, and A. D. Genio, 2002: Evidence for strengthening of the tropical general circulation in the 1990s. *Science*, **295**, 838-841.

Chen, Y., and A. D. Del Genio, 2009: Evaluation of tropical clouds regimes in observations and a general circulation model. *Climate Dynam.*, **32**, 355-369.

Ciesielski, P. E., and R. H. Johnson, 2006: Contrasting characteristics of convection over the northern and southern South China Sea during SCSMEX. *Mon. Wea. Rev.*, **134**, 1041-1062.

----------, W. H. Schubert, and R. H. Johnson, 1999: Large-scale heat and moisture budgets over the ASTEX region. *J. Atmos. Sci.*, **56**, 3241-3261.

Cohen, J. L., D. A. Salstein, and R. D. Rosen, 2000: Interannual variability in the meridional transport of water vapor. *J. Hydrometeor.*, **1**, 547-553.

Compo, G. P., and coauthors, 2011: The twentieth century reanalysis project. *Quart. J. Roy. Meteor. Soc.*, **137**, 1-28.

Dee, D. P., and S. Uppala, 2009: Variational bias correction of satellite radiance data in the ERA-Interim reanalysis. *Quart. J. Roy. Meteor. Soc.*, **135**, 1830-1841.

Dima, I., and J. M. Wallace, 2003: On the seasonality of the Hadley cell. *J. Atmos. Sci.*, **60**, 1522-1527.

Dragani, R., 2011: On the quality of the ERA-Interim ozone reanalyses: Comparisons with satellite data. *Quart. J. Roy. Meteor. Soc.*, **137**, 1312-1326.

Feng, J., and J. Li, 2013: Contrasting impacts of two types of ENSO on the boreal spring Hadley circulation. *J. Climate*, in press.

Fierro, A. O., J. Simpson, M. A. LeMone, J. M. Straka, and B. F. Smull, 2009: On how hot towers fuel the Hadley cell: An observational and modeling study of line-organized convection in the equatorial trough from TOGA COARE. *J. Atmos. Sci.*, **66**, 2730-2746.

Frierson, D. M. W., J. Lu, and G. Chen, 2007: Width of the Hadley cell in simple and comprehensive general circulation models. *Geophys. Res. Lett.*, **34**, L18804, doi:19.1029/2007GL031115.

Fu, Q., C. M. Johanson, J. M. Wallace, and T. Reichler, 2006: Enhanced mid-latitude tropospheric warming in satellite measurements. *Science*, **312**, 1179.

Giese, B. S., and J. A. Carton, 1999: Interannual and decadal variability in the tropical and midlatitude Pacific Ocean. *J. Climate*, **12**, 3402-3418.

Gordon, N. D., and J. R. Norris, 2010: Cluster analysis of midlatitude oceanic cloud regimes: Mean properties and temperature sensitivity. *Atmos. Chem. Phys.*, **10**, 6435-6459.

Hack, J. J., 1994: Parameterization of moist convection in the national center for atmospheric research community climate model (CCM2). *J. Geophys. Res.*, **99**, 5551-5568, doi:10.1029/93JD03478.

Hartmann, D. L., H. H. Hendon, and R. A. Houze Jr., 1984: Some implications of the mesoscale circulations in tropical cloud clusters for large-scale dynamics and climate. *J. Atmos. Sci.,* **41,** 113-121.

----------, and K. Larson, 2002: An important constraint on tropical cloud - climate feedback. *Geophys. Res. Lett.*, **29**, doi:10.1029/2002GL015835.

Held, I. M, 2000: The general circulation of the atmosphere. *Proc. Program in Geophysical Fluid Dynamics*. Woods Hole Oceanography Institution, Woods Hole, MA. http://gfd.whoi.edu/proceedings/2000/PDFvol2000.html

----------, and A. Y. Hou, 1980: Nonlinear axially symmetric circulations in a nearly inviscid atmosphere. *J. Atmos. Sci*., **37**, 515-533.

Heymsfield, A. J., S. Matrosov, and B. Baum, 2003: Ice water path–optical depth relationships for cirrus and deep stratiform ice cloud layers. *J. Appl. Meteor.*, **42**, 1369-1390.

Higgins, R. W., V. E. Kousky, V. B. S. Silva, E. Becker, and P. Xie, 2010: Intercomparison of daily precipitation statistics over the United States in observations and in NCEP reanalysis products. *J. Climate*, **23**, 4637-4650.

Hitchman, M. H., and M. J. Rogal, 2010: ENSO influences on Southern Hemisphere column ozone during the winter to spring transition. *J. Geophys. Res.*, **115**, D20104, doi:10.1029/2009JD012844.

Holtslag, A. A. M., and B. A. Boville, 1993: Local versus nonlocal boundary layer diffusion in global climate models. *J. Climate*, **6**, 396-410.

Houze, R. A. Jr., 1982: Clouds clusters and large-scale vertical motion in the tropics. *J. Meteor. Soc. Japan*, **60**, 396-410.

----------, 1989: Observed structure of mesoscale convective systems and implications for large-scale heating. *Quart. J. Roy. Meteor. Soc.*, **115**, 425-461.

Hu, Y., and Q. Fu, 2007: Observed poleward expansion of the Hadley circulation since 1979. *Atmos. Chem. Phys.*, **7**, 5229-5236.

Hudson, R. D., M. F. Andrade, M. B. Follette, and A. D. Frolov, 2006: The total ozone separated into meteorological regimes – Part II: Northern hemisphere mid-latitude total ozone trends. *Atmos. Chem. Phys.*, **6**, 5183-5191.

Hurwitz, M. M., P. A. Newman, L. D. Oman, and A. M. Molod, 2011: Response of the Antarctic stratosphere to two types of El Niño events. *J. Atmos. Sci.*, **68**, 812-822.

Jakob, C., and C. Schumacher, 2008: Precipitation and latent heating characteristics of the major tropical western pacific cloud regimes. *J. Climate*, **21**, 4348-4364.

----------, and G. Tselioudis, 2003: Objective identification of cloud regimes in the tropical western Pacific. *Geophys. Res. Lett.*, **30**, 2082, doi:10.1029/2003GL018367.

----------, ----------, and T. Hume, 2005: The radiative, clouds, and thermodynamic properties of the major tropical western Pacific clouds regimes. *J. Climate.*, **18**, 1203-1215.

Jia, X., C. Li, N. Zhou, and J. Ling, 2010: The MJO in an AGCM with three different cumulus parameterization schemes. *Dynam. Atmos. Ocean*, **49**, 1141-1163.

Jiang, X., and coauthors, 2011: Vertical diabatic heating structure of the MJO: Intercomparison between recent reanalyses and TRMM estimates. *Mon. Wea. Rev.*, **139**, 3208-3233.

Johanson, C. M., and Q. Fu, 2009: Hadley cell widening: Model simulations versus observations. *J. Climate*, **22**, 2713-2725.

Johnson, R. H., 1976: The role of convective-scale precipitation downdrafts in cumulus and synoptic-scale interactions. *J. Atmos. Sci.,* **33,** 1890-1910.

----------, 1984: Partitioning tropical heat and moisture budgets into cumulus and mesoscale components: Implications for cumulus parameterization. *Mon. Wea. Rev.*, **112**, 1590-1601.

----------, and P. E. Ciesielski, 2000: Rainfall and radiative heating rates from TOGA COARE atmospheric budgets. *J. Atmos. Sci.*, **57**, 1497-1514.

----------, ----------, T. S. L'Ecuyer, and A. J. Newman, 2010: Diurnal cycle of convection during the 2004 North American Monsoon Experiment. *J. Climate*, **23**, 1060-1078.

----------, ----------, B. D. McNoldy, P. J. Rogers, and R. K. Taft, 2007: Multiscale variability of the flow during the North American monsoon experiment. *J. Climate*, **20**, 1628-1648.

----------, T. M. Rickenbach, S. A. Rutledge, P. E. Ciesielski, and W. H. Schubert, 1999: Trimodal characteristics of tropical convection. *J. Climate*, **12**, 2397-2418.

Kang, S. M., D. M. W. Frierson, and I. M. Held, 2009: The tropical response to extratropical thermal forcing in an idealized GCM: The importance of radiative feedbacks and convective parameterization. *J. Atmos. Sci.*, **66**, 2812-2827.

----------, and L. M. Polvani, 2011: The interannual relationship between the eddy-driven jet and the edge of the Hadley cell, *J. Climate*, **24**, 563-568.

Kalnay, E., and coauthors, 1996: The NCEP/NCAR 40-year reanalysis project. *Bull. Amer. Meteor. Soc.*, **77**, 437-471.

Kanamitsu, M. W. Ebisuzaki, J. Woollen, S.-K. Yang, J. J. Hnilo, M. Fiorino, and G. L. Potter, 2002: NCEP/DOE AMIP-II Reanalysis (R-2). *Bull. Amer. Meteor. Soc.*, **83**, 1631-1643.

Katsumata, M., P. E. Ciesielski, and R. H. Johnson, 2011: Evaluation of budget analyses during MISMO. *J. Appl. Meteor. Climatol.*, **50**, 241-254.

Klein, S. A., and C. Jackob, 1999: Validation and sensitivities of frontal clouds simulated by the ECMWF model. *Mon. Wea. Rev.*, **127**, 2514-2531.

Korty, R. L., and T. Schneider, 2008: Extent of Hadley circulations in dry atmospheres. *Geophys. Res. Lett.*, **35**, L23803, doi:10.1029/2008GL035847.

Kummerow, C., W. Barnes, T. Kozu, J. Shiue, and J. Simpson, 1998: The Tropical Rainfall Measuring Mission (TRMM) sensor package. *J. Atmos. Oceanic Technol.*, **15**, 809-817.

Lappen, C.-L., and C. Schumacher, 2012: Heating in the tropical atmosphere: What level of details is critical for accurate MJO simulations in GCMs? *Climate. Dynam.*, **39**, 2547-2568.

L'Ecuyer, T. S., and G. McGarragh, 2010: A 10-Year climatology of tropical radiative heating and its vertical structure from TRMM observations. *J. Climate*, **23**, 519-541.

----------, and G. L. Stephens, 2003: The tropical oceanic energy budget from the TRMM perspective. Part I: Algorithm and uncertainties. *J. Climate*, **16**, 1967-1985.

Lee, D., L. Oreopoulos, G. J. Huffman, W. B. Rossow, and I.-S. Kang, 2013: The precipitation characteristics of ISCCP tropical weather states. *J. Climate*., in press.

Li, C., X. Jia, J. Ling, W. Zhou, and C. Zhang, 2009: Sensitivity of MJO simulations to diabatic heating profiles. *Climate Dynam.*, **32**, 167-187.

Li., W., C. Schumacher, and S. A. McFarlane, 2013: Radiative heating of the ISCCP upper level cloud regimes and its impact on the large-scale tropical circulation. *J. Geophys. Res.*, in press.

Lin, J., B. Mapes, M. Zhang, and M. Newman, 2004: Stratiform precipitation, vertical heating profiles, and the Madden-Julian Oscillation. *J. Atmos. Sci.*, **61**, 296-309.

Lin. W. Y., and M. H. Zhang, 2004: Evaluation of clouds and their radiative effects simulated by the NCAR community atmospheric model against satellite observations. *J. Climate*, **17**, 3302-3318.

Lin, X., and R. H. Johnson, 1996: Heating, moistening and rainfall over the western Pacific during TOGA COARE. *J. Atmos. Sci.,* **53,** 3367-3383.

Lu, J., G. Chen, and D. M. W. Frierson, 2008: Response of the zonal mean atmospheric circulation to El Niño versus global warming. *J. Climate*, **21**, 5835-5851.

----------, C. Deser, and T. Reichler, 2009: Cause of the widening of the tropical belt since 1958. *Geophys. Res. Lett.*, **36**, L03803, doi:10.1029/2008GL036076.

----------, G. A. Vecchi, and T. Reichler, 2007: Expansion of the Hadley cell under global warming. *Geophys. Res. Lett.*, **34**, L06805, doi:10.1029/2006GL028443.

Ma, J., and J. Li, 2008: The principle modes of variability of the boreal winter Hadley cell. *Geophys. Res. Lett.*, **35**, L01808, doi:10.1029/2007GL031883.

Ma, L., T. Zhang, O. W. Frauenfeld, B. Ye, D. Yang and D. Qin, 2009: Evaluation of precipitation from the ERA-40, NCEP-1, and NCEP-2 reanalyses and CMAP-1, CMAP-2, and GPCP-2 with ground-based measurements in China. *J. Geophys. Res.*, **114**, D09105, doi:10.1029/2008JD011178.

Madden, R. A., and P. R. Julian, 1994: Observations of the 40-50-day tropical oscillation – A review. *Mon. Wea. Rev.*, **122**, 814-837.

Mantsis, D. F., and A. C. Clement, 2009: Simulated variability in the mean atmospheric meridional circulation over the 20th century. *Geophys. Res. Lett.*, **36**, L06704, doi:10.1029/2008GL036741.

Mapes, B. E., P. E. Ciesielski, and R. H. Johnson, 2003: Sampling errors in rawinsonde-array budgets. *J. Atmos. Sci.,* **60,** 2697-2714.

Mekonnen, A., and W. B. Rossow, 2011: The interaction between deep convection and easterly waves over tropical north Africa: A weather state perspective. *J. Climate*, **24**, 4276-4294.

Menon, S., J. Hansen, L. Nazarenko, and Y. Luo, 2002: Climate effects of black carbon aerosols in China and India. *Science*, **297**, 2250-2253.

Mitas, C. M., and A. Clement, 2005: Has the Hadley cell been strengthening in recent decades? *Geophys. Res. Lett.*, **32**, L03809, doi:10.1029/2004GL021765.

----------, and ----------, 2006: Recent behavior of the Hadley cell and tropical thermodynamics in climate models and reanalyses. *Geophys. Res. Lett.*, **33**, L01810, doi:10.1029/2005GL024406.

Moorthi, S., and M. J. Suarez, 1992: Relaxed Arakawa-Schubert. A Parameterization of moist convection for general circulation models. *Mon. Wea. Rev.*, **120**, 978-1002.

Morcrette, J.-J., and Y. Fouquart, 1986: The overlapping of cloud layers in shortwave radiation parameterizations. *J. Atmos. Sci.*, **43**, 321-328.

Mu, M., and C. Zhang, 2008: Energetics of Madden-Julian Oscillation in the NCAR CAM3: A composite view. *J. Geophys. Res.*, **113**, D05108, doi:10.1029/2007JD008700.

Neggers, R. A. J., J. D. Neelin, and B. Stevens, 2007: Impact mechanisms of shallow cumulus convection on tropical climate dynamics. *J. Climate*, **20**, 2623-2642.

Newell, R. E., and B. C. Weare, 1976: Ocean temperatures and large scale atmospheric variations. *Nature*, **262**, 40-41.

Nigam, S., C. Chung, and E. DeWeaver, 2000: ENSO diabatic heating in ECMWF and NCEP-NCAR reanalyses, and NCAR CCM3 simulation. *J. Climate*, **13**, 3152-3171.

Nitta, T., and S. Esbensen, 1974: Heat and moisture budget analyses using BOMEX data. *Mon. Wea. Rev.,* **102,** 17-28.

Olson, W. S., and coauthors, 2006: Precipitation and latent heating distributions from satellite passive microwave radiometery. Part I: Improved method and uncertainties. *J. Appl. Meteor. Climatol.*, **45**, 702-720.

Onogi, K., and coauthors, 2007: The JRA-25 reanalysis. *J. Meteor. Soc. Japan*, **85**, 369-432.

Oort, A. H., and E. M. Rasmusson, 1970: On the annual variation of the monthly mean meridional circulation. *Mon. Wea. Rev.*, **98**, 423-442.

----------, and J. J. Yienger, 1996: Observed interannual variability in the Hadley circulation and its connection to ENSO. *J. Climate*, **9**, 2751-2767.

Oreopoulos, L., and W. B. Rossow, 2011: The cloud radiative effects of International Satellite Cloud Climatology Project weather states. *J. Geophy. Res.*, **116**, D12202, doi:10.1029/2010JD015472.

Pan, Y. H., and A. H. Oort, 1983: Global climate variations connected with sea surface temperature anomalies in the eastern equatorial Pacific Ocean for the 1958–73 period. *Mon. Wea. Rev.*, **111**, 1244–1258.

Pincus, R., C. Hannay, S. A. Klein, K.-M. Xu, and R. Hemler, 2005: Overlap assumptions for assumed probability distribution function cloud schemes in large-scale models. *J. Geophys. Res.*, **110**, D15S09, doi:10.1029/2004JD005100.

Polvani, L. M., and P. J. Kushner, 2002: Tropospheric response to stratospheric perturbations in a relatively simple general circulation model. *Geophys. Res. Lett.*, **29**, doi:10.1029/2001GL014284.

----------, D. W. Waugh, G. J. P. Correa, and S.-W. Son, 2011: Stratospheric ozone depletion: The main driver of 20th Century atmospheric circulation changes in the southern hemisphere, *J. Climate*, **24**, 795-812.

Posselt, D. J., A. R. Jongeward, C.-Y. Hsu, and G. L. Potter, 2012: Object-based evaluation of MERRA cloud physical properties and radiative fluxes during the 1998 El Niño–La Niña transition. *J. Climate*, **25**, 7313-7327.

Quan, X.-W., H. F. Diaz, and M. P. Hoerling, 2004: Change of the tropical Hadley cell since 1950. *The Hadley Circulation: Past, Present and Future*. H. F. Diaz and R. S. Bradley, Eds., Cambridge Univ. Press, New York, 85-120.

Quartly, G. D., E. A. Kyte, M. A. Srokosz, and M. N. Tsimplis, 2007: An intercomparison of global oceanic precipitation climatologies. *J. Geophys. Res.*, **112**, D10121, doi:10.1029/2006JD007810.

Rickenbach, T. M., 2004: Nocturnal cloud systems and the diurnal variation of clouds and rainfall in southwestern Amazonia. *Mon. Wea. Rev.*, **132**, 1201-1219.

Riehl, H., and J. S. Malkus, 1958: On the heat balance in the equatorial trough zone. *Geophysica*, **6**, 503-538.

----------, and J. Simpson, 1979: On the heat balance in the equatorial trough zone, revisited. *Contrib. Atmos. Phys.*, **52**, 287-305.

Rienecker, M. M., and coauthors, 2008: The GEOS-5 Data Assimilation System – Documentation of versions 5.0.1 and 5.1.0, and 5.2.0. NASA Tech. Rep. Series on Global Modeling and Data Assimilation, NASA/TM-2008-104606, Vol. 27, 92 pp.

----------, and coauthors, 2011: MERRA - NASA's modern-era retrospective analysis for research and applications. *J. Climate*, **24**, 3624-3648.

Riley, E. M., B. E. Mapes, and S. N. Tulich, 2011: Clouds associated with the Madden–Julian Oscillation: A new perspective from CloudSat. *J. Atmos. Sci.*, **68**, 3032-3051.

Robertson, F. R., M. G. Bosilovich, J. Chen, and T. L. Miller, 2011: The effect of satellite observing system changes on MERRA water and energy fluxes. *J. Climate*, **24**, 5197-5217.

Rossow, W. B., and R. A. Schiffer, 1999: Advances in understanding clouds from ISCCP. *Bull. Amer. Meteor. Soc.*, **80**, 2261-2288.

----------, G. Tselioudis, A. Polak, and C. Jakob, 2005: Tropical climate described as a distribution of weather states indicated by distinct mesoscale cloud property mixtures. *Geophys. Res. Lett.*, **32**, L21812. Doi: 10.1029:2005GL024584.

Ruppert, J. H., R. H. Johnson, and A. K. Rowe, 2013: Diurnal cycle of rainfall in Taiwan during SoWMEX/TiMREX (2008). Submitted to *J. Atmos. Sci.*

Saha, S., and coauthors, 2010: The NCEP climate forecast system reanalysis. *Bull. Amer. Meteor. Soc.*, **91**, 1015-1097.

Sardeshmukh, P. D., 1993: The baroclinic χ problem and its application to the diagnosis of atmospheric heating rates. *J. Atmos. Sci.*, **50**, 1099-1112

Schiffer, R. A., and W. B. Rossow, 1983: The International Satellite Cloud Climatology Project (ISCCP): The first project of the World Climate Research Programme. *Bull. Amer. Meteor. Soc.*, **64**, 779-784.

Schumacher, C., P. E. Ciesielski, and M. H. Zhang, 2008: Tropical cloud heating profiles: Analysis from KWAJEX. *Mon. Wea. Rev.*, **136**, 4289-4300.

----------, R. A. Houze Jr., and I. Kraucunas, 2004: The tropical dynamical response to latent heating estimates derived from the TRMM precipitation radar. *J. Atmos. Sci.*, **61**, 1341-1358.

----------, M. H. Zhang, and P. E. Ciesielski, 2007: Heating structures of the TRMM field campaigns. *J. Atmos. Sci.*, **64**, 2593-2610.

Seager, R., N. Harnik, Y. Kushnir, W. Robinson, and J. Miller, 2003: Mechanisms of hemispherically symmetric climate variability. *J. Climate*, **16**, 2960-2978.

Seidel, D. J., and W. J. Randel, 2007: Recent widening of the tropical belt: Evidence from tropopause observations. *J. Geophys. Res.*, **112**, D20113, doi:10.1029/2007JD008861.

Shige., S., Y. N. Takayabu, W.-K. Tao, and D. E. Johnson, 2004: Spectral retrieval of latent heating profiles from TRMM PR data. Part I: Development of a model-based algorithm. *J. Appl. Meteor.*, **43**, 1095-1113.

Smith, T. M., and R. W. Reynolds, 2004: Improved extended reconstruction of SST (1854-1997). *J. Climate*, **17**, 2466-2477.

Sohn, B. J., and S.-C. Park, 2010: Strengthened tropical circulations in past three decades inferred from water vapor transport. *J. Geophys. Res.*, **115**, D15112, doi:10.1029/2009JD013713.

Song, H, and M. Zhang, 2007: Changes of the boreal winter Hadley circulation in the NCEP-NCAR and ECMWF reanalyses: A comparative study. *J. Climate*, **20**, 5191-5200.

Stachnik, J. P., and C. Schumacher, 2011: A comparison of the Hadley circulation in modern reanalyses. *J. Geophys. Res.*, **116**, D22102, doi:10.1029/2011JD016677.

----------, and ----------, 2013: Tropical and subtropical cloud regimes in the MERRA reanalysis using an ISCCP simulator. *J. Climate*, submitted.

----------, ----------, and P. E. Ciesielski, 2013: Total heating characteristics of the ISCCP tropical and subtropical cloud regimes. *J. Climate*, conditionally accepted.

Sud, Y. C., and G. K. Walker, 1999: Microphysics of clouds with the relaxed Arakawa-Schubert scheme (McRAS). Part I: Design and evaluation with GATE phase III data. *J. Atmos. Sci.*, **56**, 3196-3220.

Sundqvist, H., 1978: A parameterization scheme for non-convective condensation including prediction of cloud water content. *Quart. J. Roy. Meteor. Soc.*, **104**, 677-690.

Tandon, N. F., E. P. Gerber, A. H. Sobel, and L. M. Polvani, 2013: Understanding Hadley cell expansion vs. contraction: Insights from simplified models and implications for recent observations, *J. Climate*, in press.

Tao, W.-K., and coauthors, 2001: Retrieved vertical profiles of latent heat release using TRMM rainfall products for February 1988. *J. Appl. Meteor.*, **40**, 957-982.

----------, and coauthors, 2006: Retrieval of latent heating from TRMM measurements. *Bull. Amer. Meteor. Soc.*, **87**, 1555-1572.

----------, S. Lang, X. Zeng, S. Shige, Y. Takayabu, 2010: Relating convective and stratiform rain to latent heating. *J. Climate.*, **43**, 1874-1893.

Tromeur, E, and W. B. Rossow, 2010: Interaction of tropical deep convection with the large-scale circulation in the MJO. *J. Climate*, **23**, 1837-1853.

Thompson, R. M., Jr., S. W. Payne, E. E. Recker, and R. J. Reed, 1979: Structure and properties of synoptic-scale wave disturbances in the intertropical convergence zone of the eastern Atlantic. *J. Atmos. Sci.,* **36,** 53-72.

Thorne, P. W., and R. S. Vose, 2010: Reanalyses suitable for characterizing long-term trends: Are they really achievable? *Bull. Amer. Meteor. Soc.*, **91**, 353-361.

Trenberth, K. E., 2002: Changes in tropical clouds and radiation. *Science*, **296**, 2095.

----------, J. T. Fasullo, and J. Mackaro, 2011: Atmospheric moisture transports from ocean to land and global energy flows in reanalyses. *J. Climate*, **24**, 4907-4924.

----------, D. P. Stepaniak, and J. M. Caron, 2000: The global monsoon as seen through the divergent atmospheric circulation. *J. Climate*, **13**, 3969-3993.

Tselioudis, G., and W. B. Rossow, 2011: Time scales of variability of the tropical atmosphere derived from cloud-defined weather states. *J. Climate*, **24**, 602-608.

Twomey, S., 1977: The influence of pollution on the shortwave albedo of clouds. *J. Atmos. Sci.*, **34**, 1149-1152.

Uppala, S. M, and coauthors, 2005: The ERA-40 reanalysis. *Quart. J. Roy. Meteor. Soc.*, **612**, 2961-3012.

Walker, C. C., and T. Schneider, 2006: Eddy influences on Hadley circulations: Simulations with an idealized GCM. *J. Atmos. Sci.,* **63**, 3333-3350.

Webb, M., C. Senior, S. Bony, and J.-J. Morcrette, 2001: Combining ERBE and ISCCP data to assess clouds in the Hadley Centre, ECMWF and LMD atmospheric climate models. *Climate Dynam*., **17**, 905-922.

Wheeler, M. C., and H. H. Hendon, 2004: An all-season real-time multivariate MJO index: Development of an index for monitoring and prediction. *Mon. Wea. Rev.*, **132**, 1917-1932.

Williams, K. D., and G. Tselioudis, 2007: GCM intercomparison of global cloud regimes: Present-day evaluation and climate change response. *Climate Dynam.*, **29**, 231-250.

----------, and M. J. Webb, 2009: A quantitative performance assessment of cloud regimes in climate models. *Climate Dynam.*, **33**, 141-157.

Wu, W., Y. Liu, and A. K. Betts, 2012: Observationally based evaluation of NWP reanalyses in modeling cloud properties over the Southern Great Plains, *J. Geophys. Res.*, **117**, D12202, doi:10.1029/2011JD016971.

Xie, S., T. Hume, C. Jakob, S. A. Klein, R. B. McCoy, and M. Zhang, 2010: Observed large-scale structures and diabatic heating and drying profiles during TWP-ICE. *J. Climate*, **23**, 57-79.

Xiping, Z., W.-K. Tao, S. W. Powell, R. A. Houze Jr., P. E. Ciesielski, N. Guy, H. Pierce and T. Matsui, 2013: A comparison of the water budgets between clouds from AMMA and TWP-ICE, *J. Atmos. Sci.*, in press.

Yanai, M., S. Esbensen, and J.-H. Chu, 1973: Determination of bulk heating properties of tropical clouds clusters from large-scale heat and moisture budgets. *J. Atmos. Sci.*, **30**, 611-627.

Yulaeva, E., and J. M. Wallace, 1994: The signature of ENSO in global temperature and precipitation fields derived from the microwave sounding unit. *J. Climate*, **7**, 1719-1736.

Zelinka, M. D., S. A. Klein, and D. L. Hartmann, 2012: Computing and partitioning cloud feedbacks using cloud property histograms. Part II: Attribution to changes in cloud amount, altitude, and optical depth. *J. Climate*, **25**, 3736-3754.

Zhang, C., M. Dong, S. Gualdi, H. H. Henden, E. D. Maloney, A. Marshall, K. R. Sperber, and W. Wang, 2006: Simulations of the Madden-Julian Oscillation in four pairs of coupled and uncoupled models. *Climate Dynam.*, **27**, 573-592.

----------, M. McGauley, and N. A. Bond, 2004: Shallow meridional circulation in the tropical eastern Pacific. *J. Climate*, **17**, 133-139.

Zhang, G. J., and N. A. McFarlane, 1995: Sensitivity of climate simulations to the parameterization of cumulus convection in the Canadian Climate Centre general circulation model. *Atmos.-Ocean*, **33,** 407-446.

Zhang, M. H., and J. L. Lin, 1997: Constrained variational analysis of sounding data based on column-integrated budgets of mass, heat, moisture, and momentum: Approach and application to ARM measurements. *J. Atmos. Sci.,* **54,** 1503-1524.

----------, ----------, R. T. Cederwall, J. J. Yio, and S. C. Xie, 2001: Objective analysis of ARM IOP data: Method and sensitivity. *Mon. Wea. Rev.,* **129,** 295-311.

----------, and coauthors, 2005: Comparing clouds and their seasonal variations in 10 atmospheric general circulation models with satellite measurements. *J. Geophys. Res.*, **110**, D15S02, doi:10.1029/2004JD005021.

APPENDIX A

TABLES AND FIGURES FOR CHAPTER II

Table A-1. Reanalysis datasets used in this study. The analysis output resolution refers to the highest resolution available for each dataset. Some surface variables (e.g., precipitation) for NNRP, NDRP, and 20CR are instead output on a Gaussian grid of ~1.875° x 1.904°. Most output on pressure levels are only available at a reduced resolution of 1.25° x 1.25° for MERRA data, and some variables (e.g., surface diagnostics) are available as 1-hourly output.

				Analysis Output Resolution		
Dataset	Source	Data Range	Resolution	Horizontal	Pressure	Temporal
JRA	JMA	1979-2007	T106L40	1.125° x 1.125°	23 levels	6-hourly
ERAINT	ECMWF	1989-present	T255L60	1.5° x 1.5°	37 levels	6-hourly
ERA40	ECMWF	1957-2002	T159L60	2.5° x 2.5°	23 levels	6-hourly
NNRP	NCEP/NCAR	1958-present	T62L28	2.5° x 2.5°	17 levels	6-hourly
NDRP	NCEP/DOE	1979-2008	T62L28	2.5° x 2.5°	17 levels	6-hourly
CFSR	NCEP	1979-present	T382L64	0.5° x 0.5°	37 levels	1-hourly
MERRA	NASA	1979-present	2/3° x 1/2°, L60	2/3° x 1/2°	42 levels	3-hourly
20CR	NOAA/CIRES	1871-2008	T62L28	2.0° x 2.0°	24 levels	6-hourly

Table A-2. Annual average values of Ψ_N^*, Ψ_S^*, p_N^*, p_S^*, and $\Delta\varphi$ for each reanalysis during the 1979-2008 period. Units for streamfunction magnitude, pressure level, and width are x 10^{10} kg s^{-1}, hPa, and ° latitude, respectively.

Dataset	Ψ_N^*	Ψ_S^*	p_N^*	p_S^*	$\Delta\varphi$
JRA	11.66	417	-14.44	471	67.5
ERAINT	11.66	645	-14.01	646	66.2
ERA40	12.84	558	-14.97	650	63.3
NNRP	9.39	479	-10.38	483	66.1
NDRP	10.96	634	-14.07	720	64.8
CFSR	11.07	668	-15.45	677	62.4
MERRA	9.65	512	-13.28	671	63.5
20CR	11.11	685	-13.31	667	66.1
ENS	10.46	603	-13.10	660	65.3

Table A-3. Yearly trends of annual average quantities from each reanalysis dataset for the 1979-2008 (1958-2008) period. The seasonal cycle is removed from the monthly data prior to determining the long-term trend. Slopes are calculated using all available data in the period of interest except when limited by the data ranges identified in Table A-1. Significant (95%) values are denoted with an asterisk. Units for HC intensity and width trends are x 10^{10} kg s^{-1} $decade^{-1}$ and ° latitude $decade^{-1}$, respectively.

	Ψ_N^*		Ψ_S^*		$\Delta\varphi$	
Dataset	1979-2008	1958-2008	1979-2008	1958-2008	1979-2008	1958-2008
JRA	0.93*		0.54*		1.48*	
ERAINT	0.03		-0.21		0.78*	
ERA40	1.43*	1.18*	-1.39*	-0.50*	0.41	-0.03
NNRP	0.45*	0.37*	-0.50*	-0.11*	0.83*	0.94*
NDRP	0.04		-0.05		1.40*	
CFSR	0.37*		0.46*		0.29	
MERRA	0.62*		-0.20*		0.33	
20CR	0.06	0.09*	-0.02	-0.14*	0.99*	0.62*
ENS	0.40*	0.36*	-0.07	-0.37*	1.10*	0.53*

Table A-4. Mean values and number of occurrences of Ψ_N^* for the 1979-2008 period for each reanalysis categorized by ENSO phase during DJF. Streamfunction units are x 10^{10} kg s^{-1}. Values significantly different (95%) from other ENSO phase means are noted for warm/neutral (*), warm/cold (^), and neutral/cold (+) conditions. ENS50 is for 1958-2008 (see text for description).

Dataset	El Niño	(#)	Neutral	(#)	La Niña	(#)	All	(#)
JRA	21.96*	9	20.62	13	20.55	6	21.04	28
ERAINT	22.08*^	6	20.93+	8	20.15	5	21.09	19
ERA40	25.89*	6	23.03	11	23.28	6	23.84	23
NNRP	17.88*^	9	16.66	13	16.50	7	17.00	29
NDRP	22.67*^	9	20.05	13	20.02	7	20.85	29
CFSR	22.13*^	9	20.62	13	20.03	7	20.95	29
MERRA	18.92*	9	17.49	13	18.03	7	18.06	29
20CR	21.07*^	9	19.49	13	19.07	7	19.88	29
ENS	20.62*^	9	18.99	13	19.00	7	19.50	29
ENS50	19.38*^	16	18.30	19	18.30	15	18.65	50

Table A-5. Same as Table A-4, but for Ψ_S^* during JJA.

Dataset	El Niño	(#)	Neutral	(#)	La Niña	(#)	All	(#)
JRA	-27.67^	8	-26.57+	17	-24.66	4	-26.61	29
ERAINT	-24.42	6	-23.89	12	-23.02	2	-23.96	20
ERA40	-27.69^	7	-27.29	13	-26.09	4	-27.21	24
NNRP	-17.92	8	-18.03	18	-17.22	4	-17.89	30
NDRP	-27.69	8	-27.13	18	-25.91	4	-27.12	30
CFSR	-28.98*	8	-27.91	18	-27.48	4	-28.14	30
MERRA	-23.53	8	-23.50	18	-22.81	4	-23.42	30
20CR	-24.35*^	8	-23.42	18	-22.87	4	-23.59	30
ENS	-24.50*^	8	-23.82	18	-23.14	4	-23.91	30
ENS50	-22.08	11	-21.42	30	-21.42	10	-21.56	51

Table A-6. Same as Table A-4, but for the annual average $\Delta\varphi$. Units are ° latitude.

Dataset	El Niño	(#)	Neutral	(#)	La Niña	(#)	All	(#)
JRA	67.1	9	67.6	16	68.5	4	67.6	29
ERAINT	65.9	6	66.2	12	67.7	2	66.3	20
ERA40	62.5^	7	63.3+	12	64.9	4	63.3	23
NNRP	65.6	9	66.2	17	67.2	4	66.2	30
NDRP	64.0^	9	64.9+	17	66.5	4	64.8	30
CFSR	62.0^	9	62.5+	17	63.6	4	62.5	30
MERRA	63.0^	9	63.5+	17	64.7	4	63.5	30
20CR	65.6	9	66.2	17	66.8	4	66.1	30
ENS	64.7^	9	65.4	17	66.3	4	65.3	30
ENS50	64.8	14	65.4	29	65.3	8	65.2	51

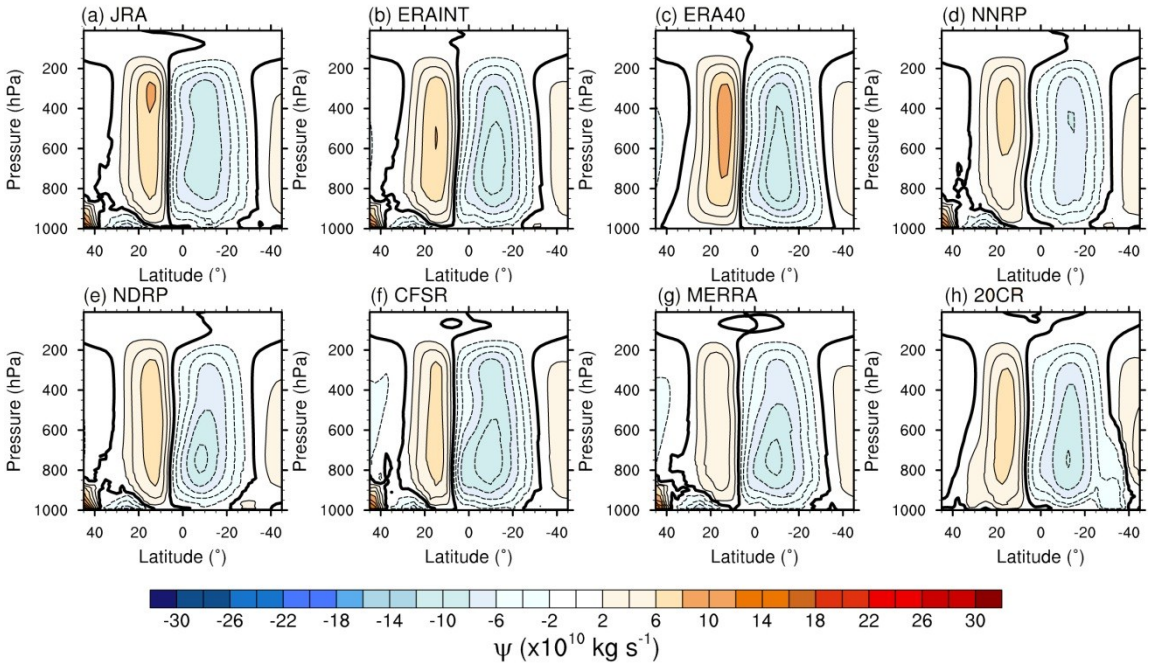

Fig. A-1. Annual average, zonal mean meridional mass streamfunction values for each reanalysis dataset during the 1979-2008 period. Positive (negative) values are indicated with solid (dashed) contours and warm (cold) colors, representing counterclockwise (clockwise) circulations. The thick solid contours correspond to values where $\Psi = 0$. Contour interval for Ψ is 2 x 10^{10} kg s^{-1}.

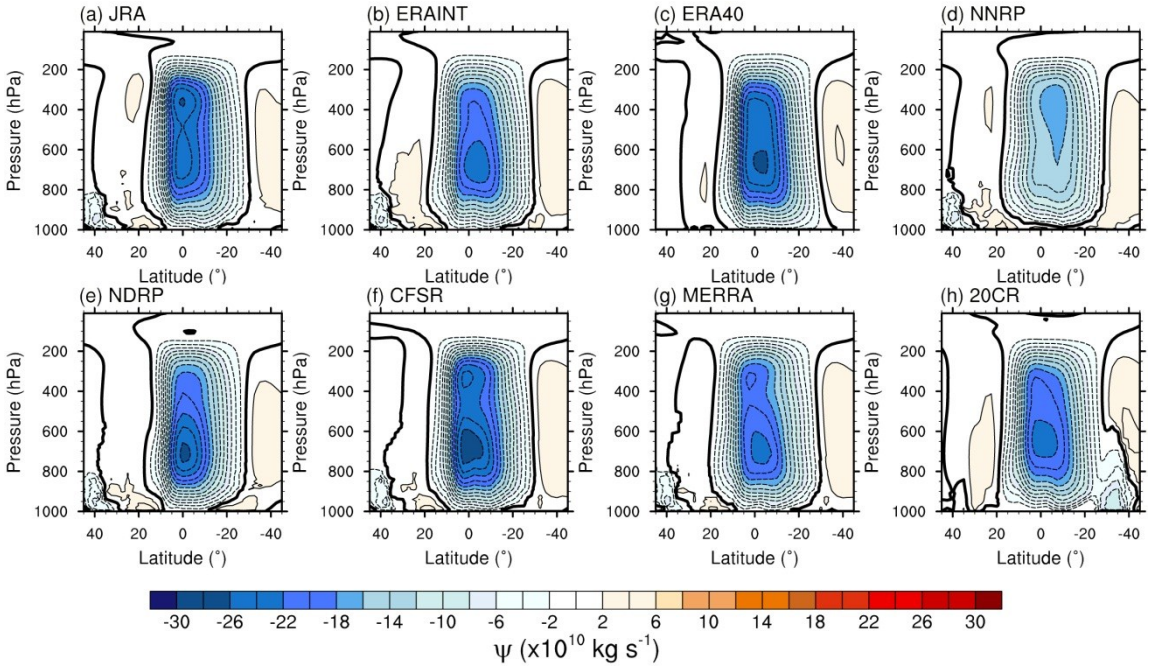

Fig. A-2. Same as Fig. A-1, but for JJA.

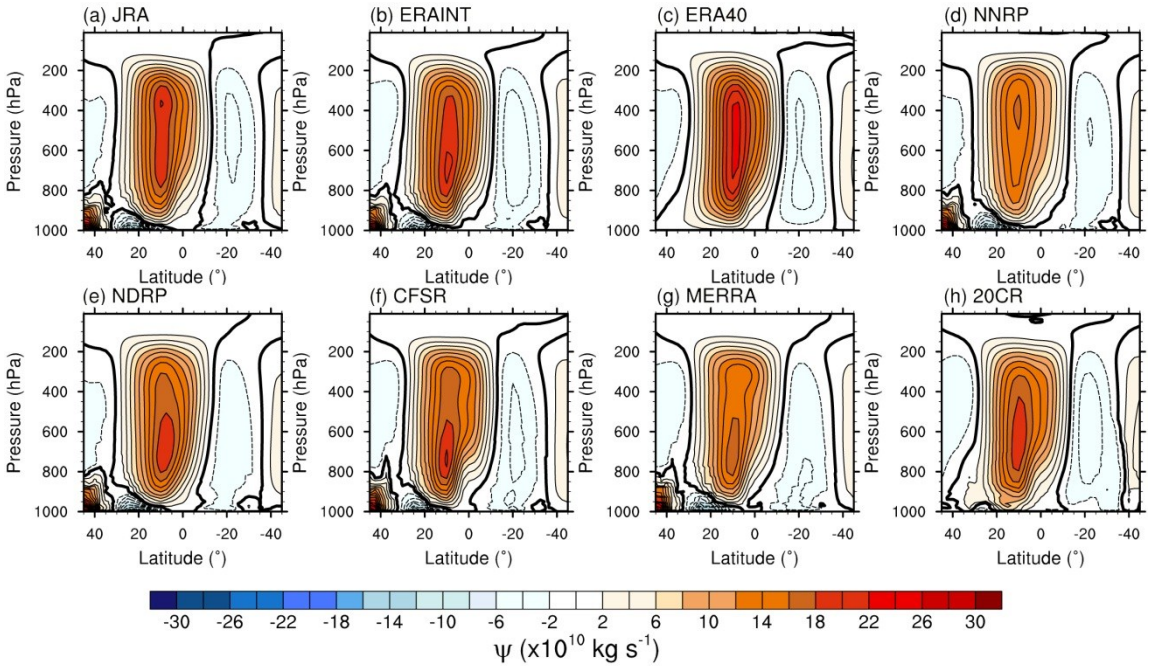

Fig. A-3. Same as Fig. A-1, but for DJF.

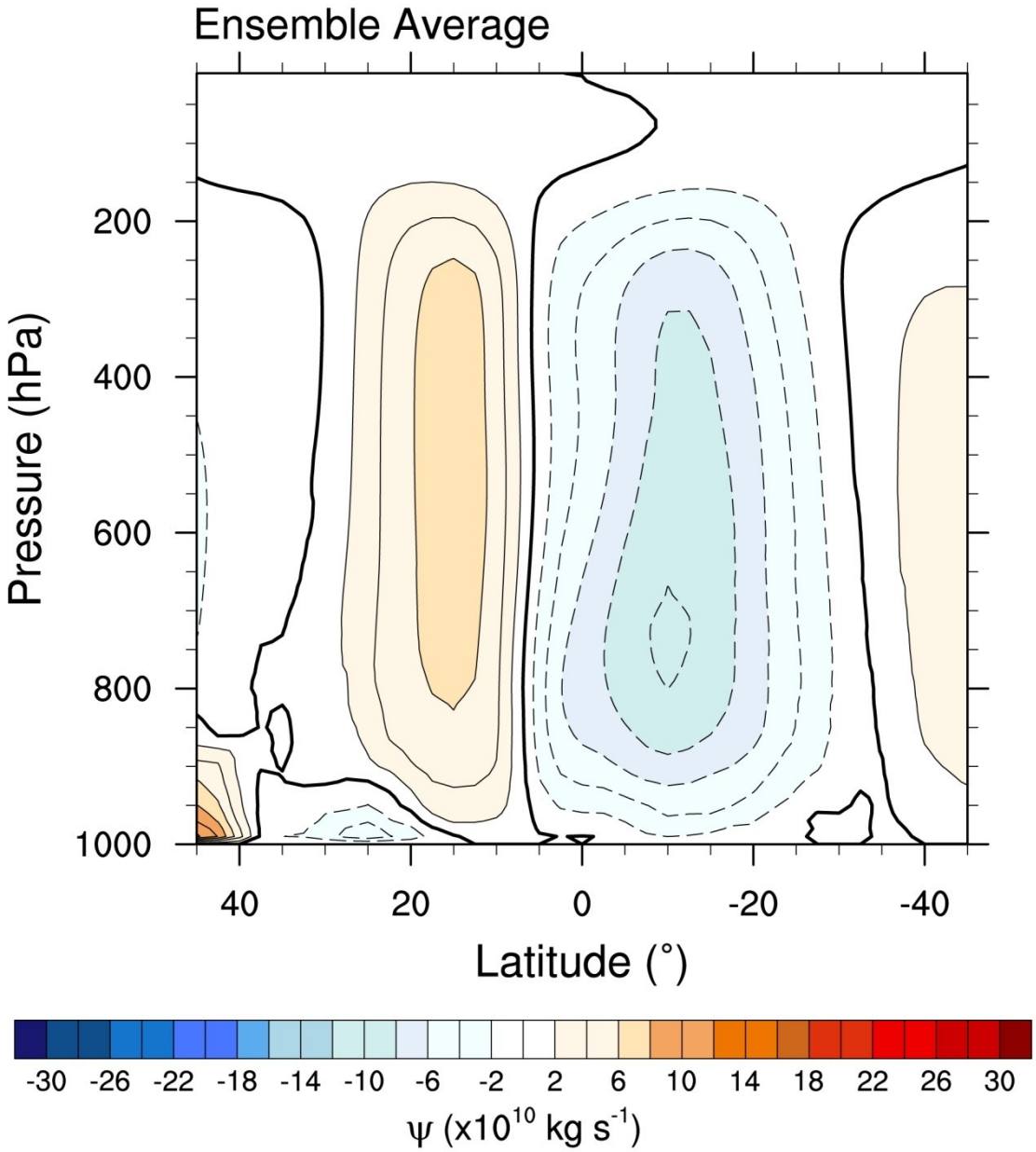

Fig. A-4. Same as Fig. A-1, but for the multi-reanalysis ensemble average.

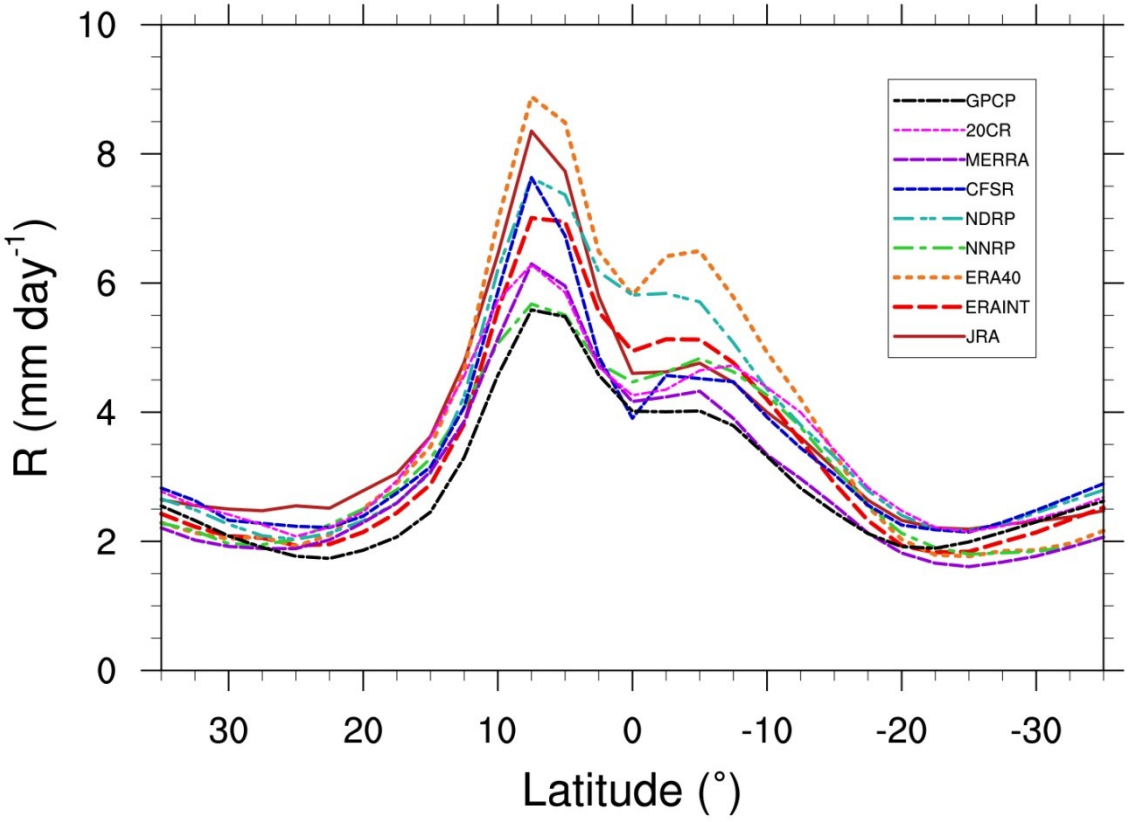

Fig. A-5. Annual average, zonal mean total precipitation rate (mm day^{-1}) for the GPCP and reanalysis datasets during the 1979-2008 period.

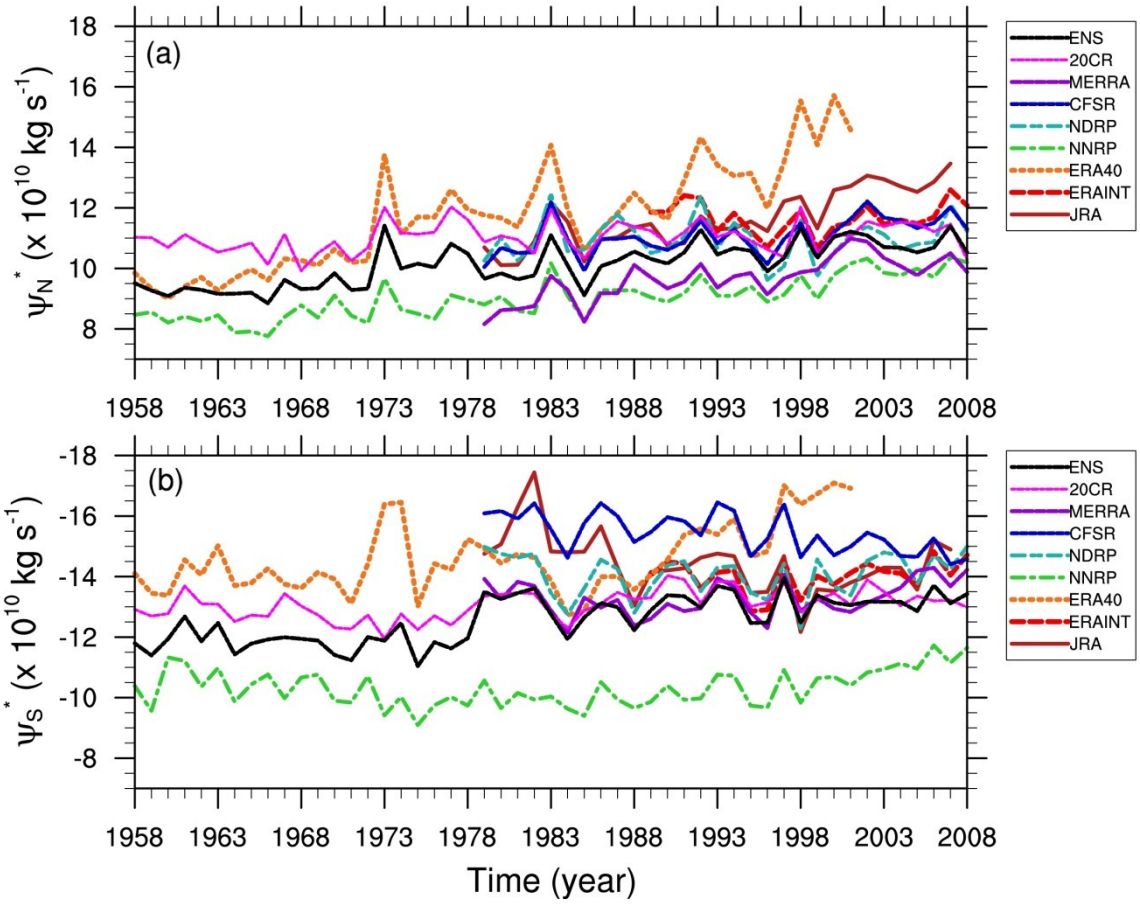

Fig. A-6. Time-series of the annual average, (a) maximum and (b) minimum zonally averaged meridional mass streamfunction, Ψ_N^* and Ψ_S^*, for each reanalysis during the 1958-2008 period.

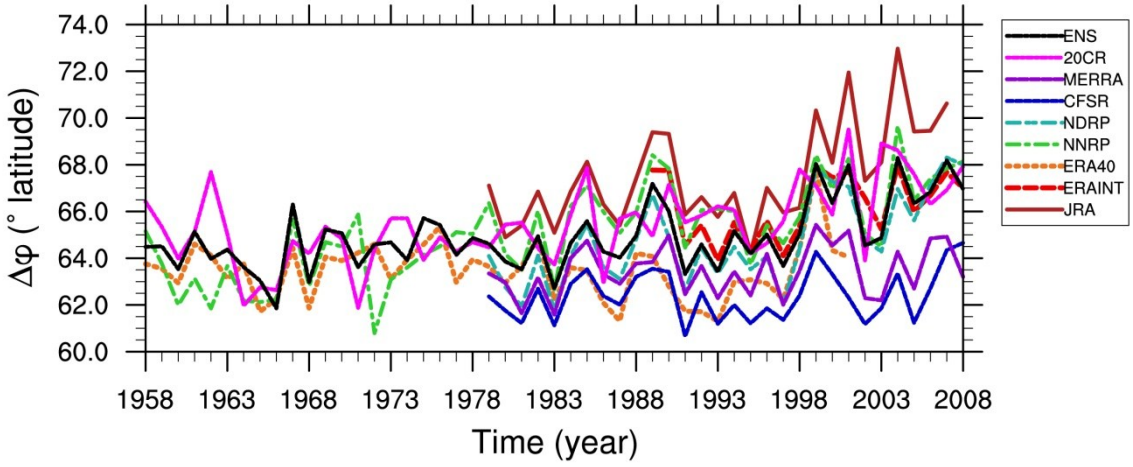

Fig. A-7. Same as Fig. A-6, but for the Hadley cell width, $\Delta\varphi$.

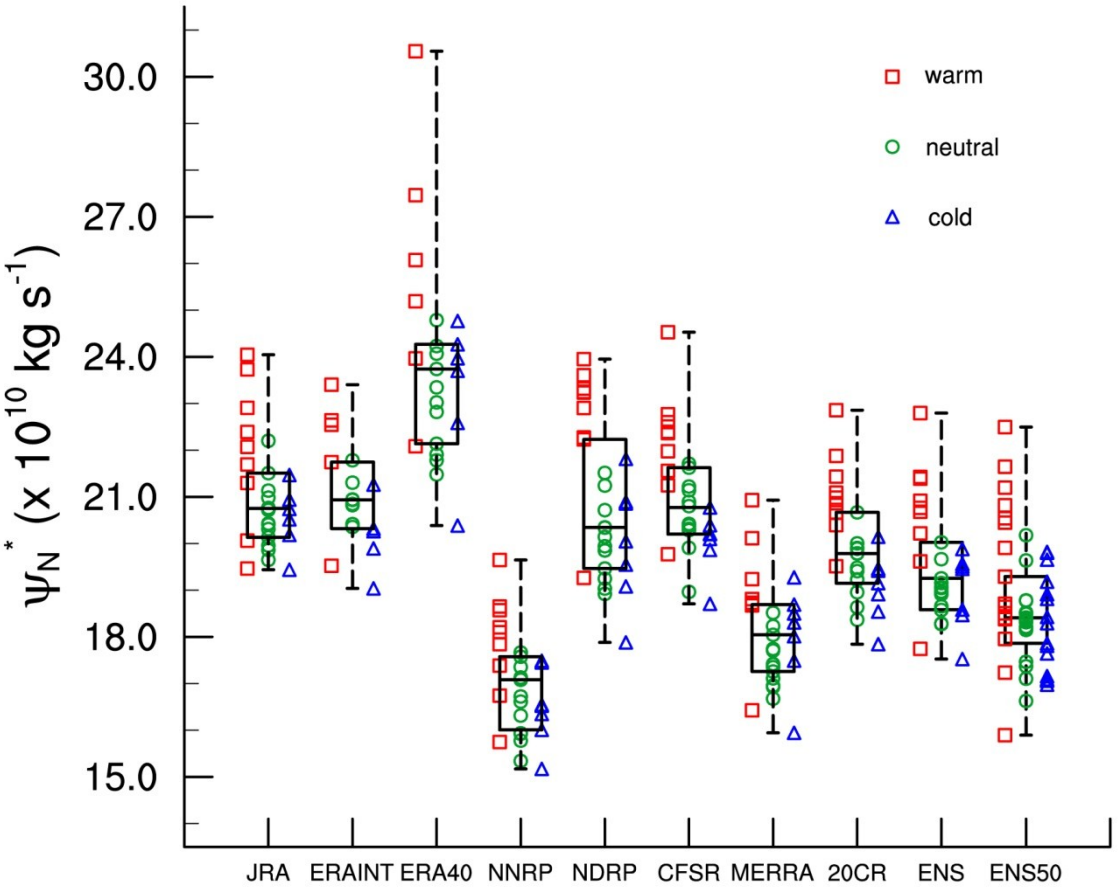

Fig. A-8. Box-whisker diagram of Ψ_N^* for each reanalysis dataset during DJF for the 1979-2008 period. Markers represent critical streamfunction values for individual seasons throughout the period and are categorized by ENSO phase. Box plot boundaries indicate the sample median and 25th/75th percentiles, with whiskers indicating maximum and minimum values. The long-term trend has been removed from the data to focus on interannual variability. The ENS50 contains the long-term (1958-2008) ENSO classifications for the average of selected datasets.

APPENDIX B

TABLES AND FIGURES FOR CHAPTER III

Table B-1. Heating data and field campaigns used in this study.

Project	Data Availability	Samples (#)	Domain Center	Reference
ASTEX	01 Jun 1992 – 15 Jun 1992	161 (3-hr)	33.75°N, 22.25°W	Ciesielski et al. (1999)
TOGA	01 Nov 1992 – 28 Feb 1993	478	1.25°S, 153.75°E	Johnson and Ciesielski (2000)
SCSMEX	06 May 1998 – 20 Jun 1998	182	21.25°N, 116.25°E	Schumacher et al. (2007)
SCSMEX	01 May 1998 – 30 Jun 1998	244	21.25/6.25°N, 116.25/106.25°E	Ciesielski and Johnson (2006)
TRMM-LBA	24 Jan 1999 – 28 Feb 1999	142	11.25°S, 61.25°W	Schumacher et al. (2007)
KWAJEX	24 Jul 1999 – 14 Sep 1999	210	8.75°N, 166.25°E	Schumacher et al. (2007)
NAME	07 Jul 2004 – 15 Aug 2004	160	26.25°N, 106.25°W	Johnson et al. (2007)
TWP-ICE	17 Jan 2006 – 12 Feb 2006	210 (3-hr)	11.25°S, 131.25°E	Xie et al. (2010)
AMMA	01 Jun 2006 – 30 Sep 2006	484	13.75/8.75°N, 6.25/3.75°E	Xiping et al. (2013)
MISMO	31 Oct 2006 – 26 Nov 2006	105	1.25°N, 76.25°E	Katsumata et al. (2011)
TIMREX	15 May 2008 – 26 Jun 2008	169	23.75°N, 121.25/118.75°E	Ruppert et al. (2013)

Table B-2. Number of samples for each project domain categorized by weather state. Campaigns meeting the minimum sample number but not appearing in Figs. B-4 and B-7 are in parentheses.

	Weather State									
Project	WS0	WS1	WS2	WS3	WS4	WS5	WS6	WS7	WS8	Total
ASTEX	0	0	3	5	0	24	23	27	34	116
TOGA	4	82	124	44	126	0	0	0	98	478
SCSMEX-N	2	52	38	53	28	6	0	2	62	243
SCSMEX-S	2	42	58	77	32	0	0	0	32	243
TRMM-LBA	0	16	48	35	4	2	0	0	36	141
KWAJEX	6	35	40	66	18	0	0	0	44	209
NAME	0	33	6	42	20	0	2	0	56	159
TWP-ICE	0	33	50	18	22	0	6	6	78	213
AMMA-N	3	18	33	96	24	6	(24)	(65)	93	362
AMMA-S	0	54	3	174	24	(63)	15	15	14	362
MISMO	0	32	16	19	2	0	6	(16)	12	103
TIMREX-L	0	29	8	40	9	0	0	0	38	124
TIMREX-O	0	34	9	39	15	0	0	2	27	126
Land	3	183	148	405	103	71	47	86	315	1361
Ocean	14	277	288	303	221	30	29	47	309	151
All	17	460	436	708	324	101	76	133	624	2879

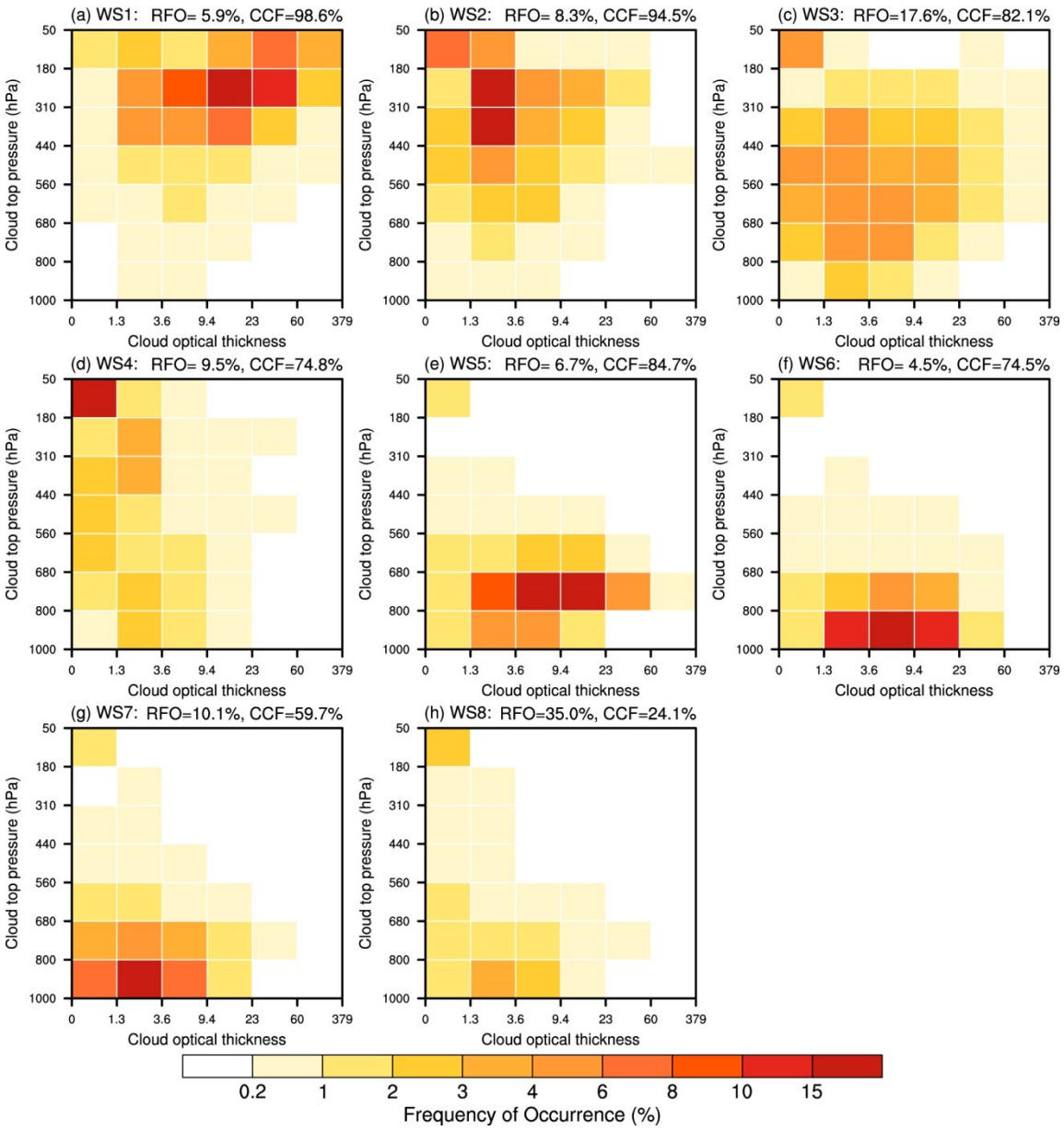

Fig. B-1. Joint histograms of cloud-top pressure and optical thickness corresponding to each of the eight weather states identified for the extended low-latitude ISCCP dataset. Shading represents the percentage of pixels within each bin (i.e., frequency of occurrence) comprising the cluster distribution. The cloud fraction sum (i.e., average total cloud cover) is listed at the top for each regime ("cluster cloud fraction" or CCF), along with the relative frequency of occurrence (RFO) from 1984-2007 over the entire 35°N-35°S domain.

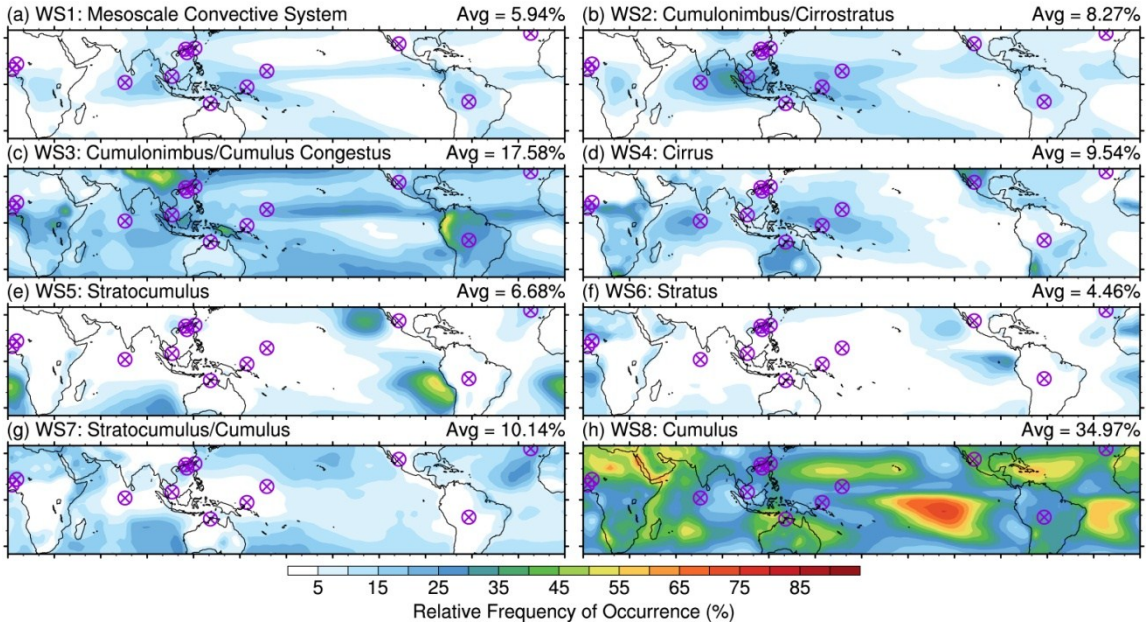

Fig. B-2. Geographic distribution of the annual average, relative frequency of occurrence for each weather state from 1984-2007. Markers indicate the ISCCP gridpoint nearest the center of the budget domain for the field campaigns identified in Table B-1.

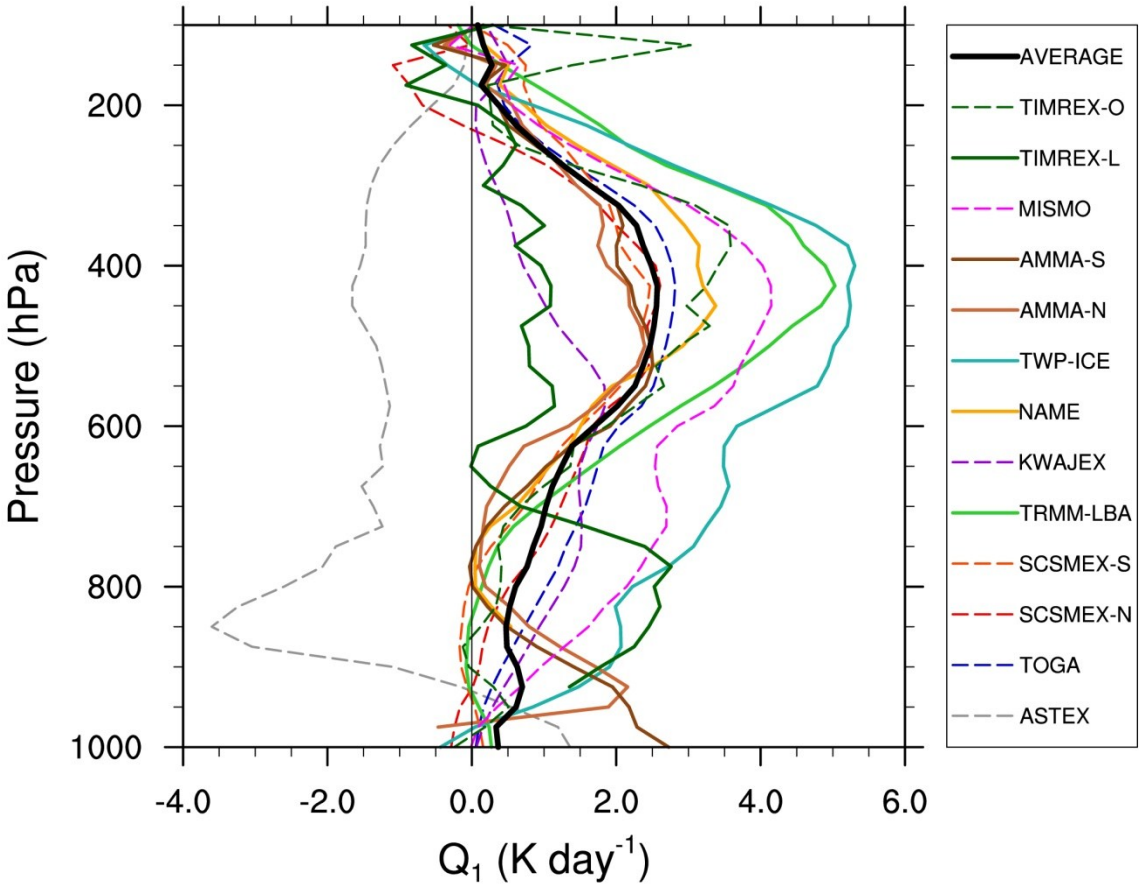

Fig. B-3. Campaign average, total diabatic heating (Q_1) profiles for the domains used in this study. Profiles for individual campaigns over mostly-land and mostly-ocean domains are indicated using solid and dashed lines, respectively. The thick line represents an equally weighted ensemble average for all domains.

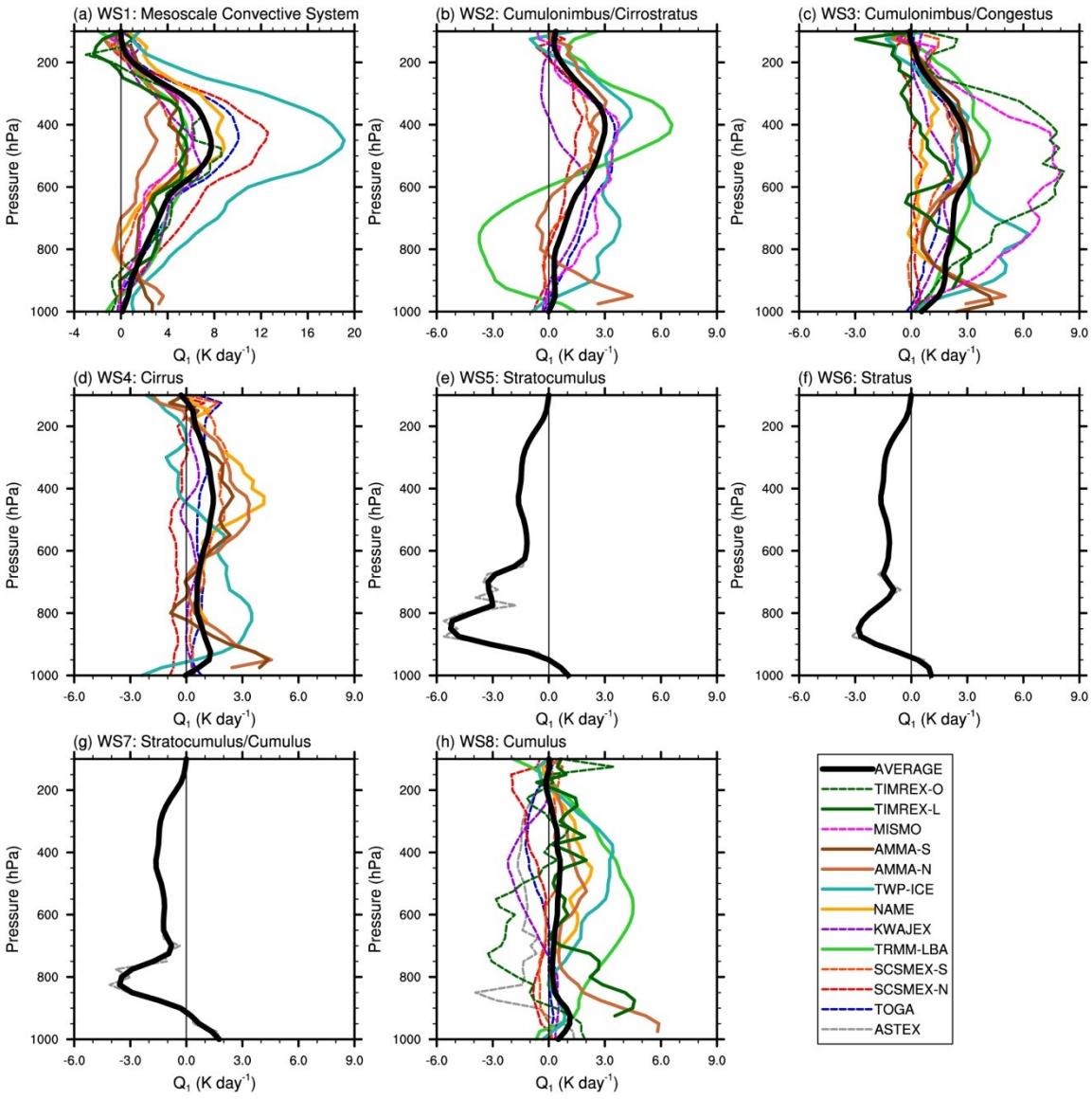

Fig. B-4. Daily average, total diabatic heating (Q_1) composite profiles for the ISCCP cloud regimes. The ensemble average (black line) is smoothed using a 1-2-1 filter. The scale used for WS1 is different from the remaining panels.

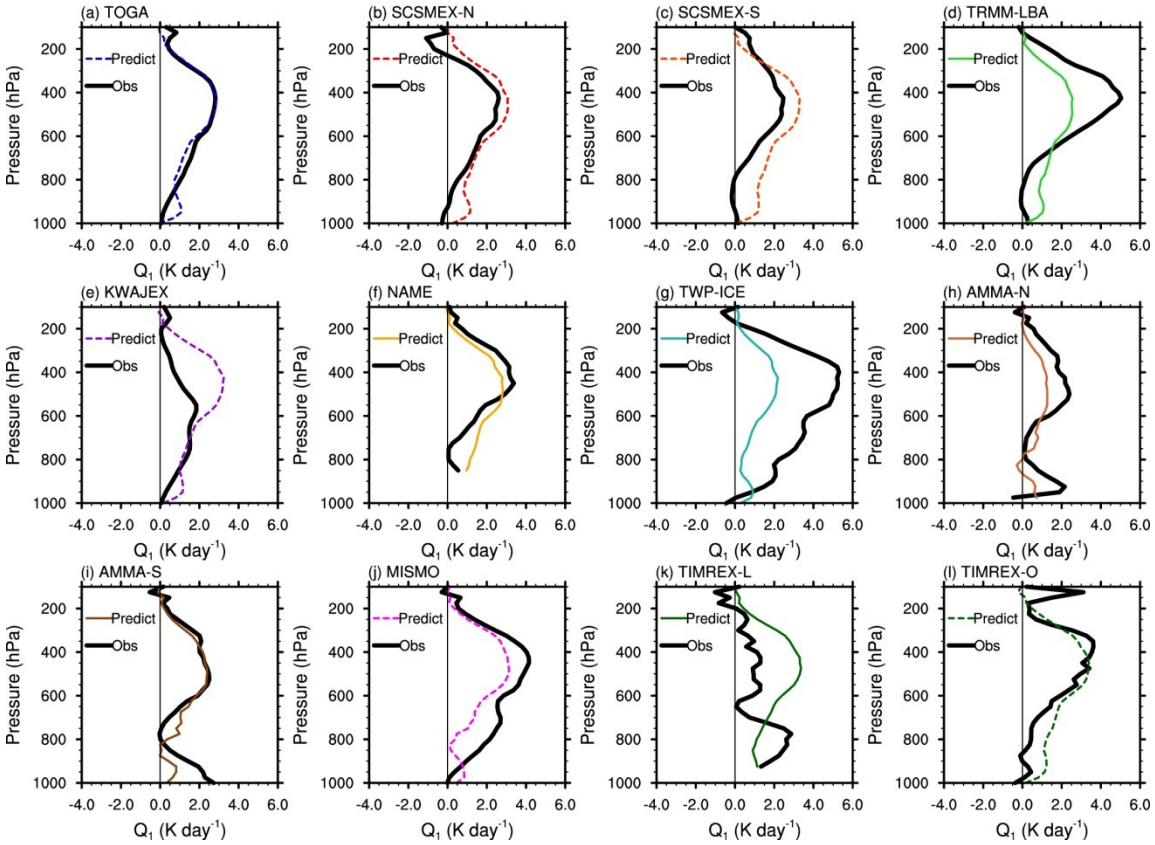

Fig. B-5. Observed total diabatic heating (Q_1) profiles for each domain (thick, black) and predicted reconstructions (thin, colors) using regime averages trained on the remaining field campaign datasets. Solid and dashed lines for the predicted profiles indicate land and ocean domains, respectively.

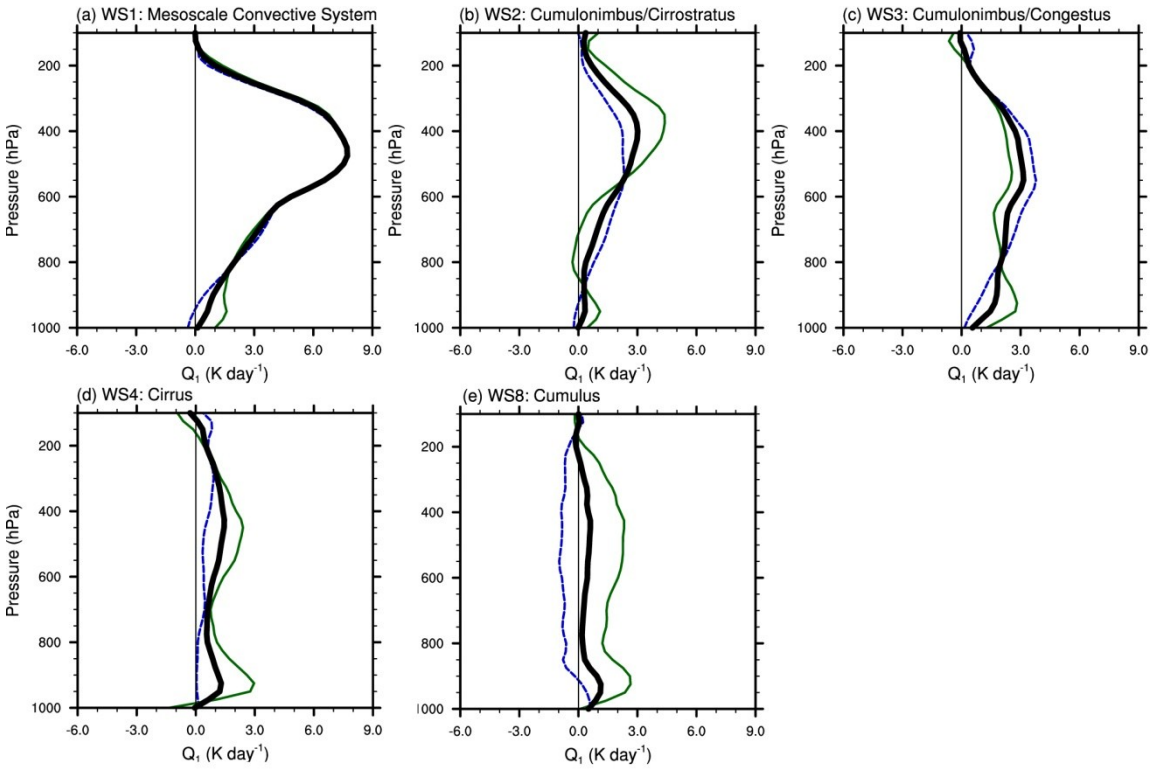

Fig. B-6. Average total heating profiles for each regime over mostly-land (thin, solid) and mostly-ocean (thin, dashed) domains. The thick line represents the equally weighted ensemble average profile for all domains, identical to Fig. B-4. Panels for WS5, WS6, and WS7 are omitted as there is no usable data over land.

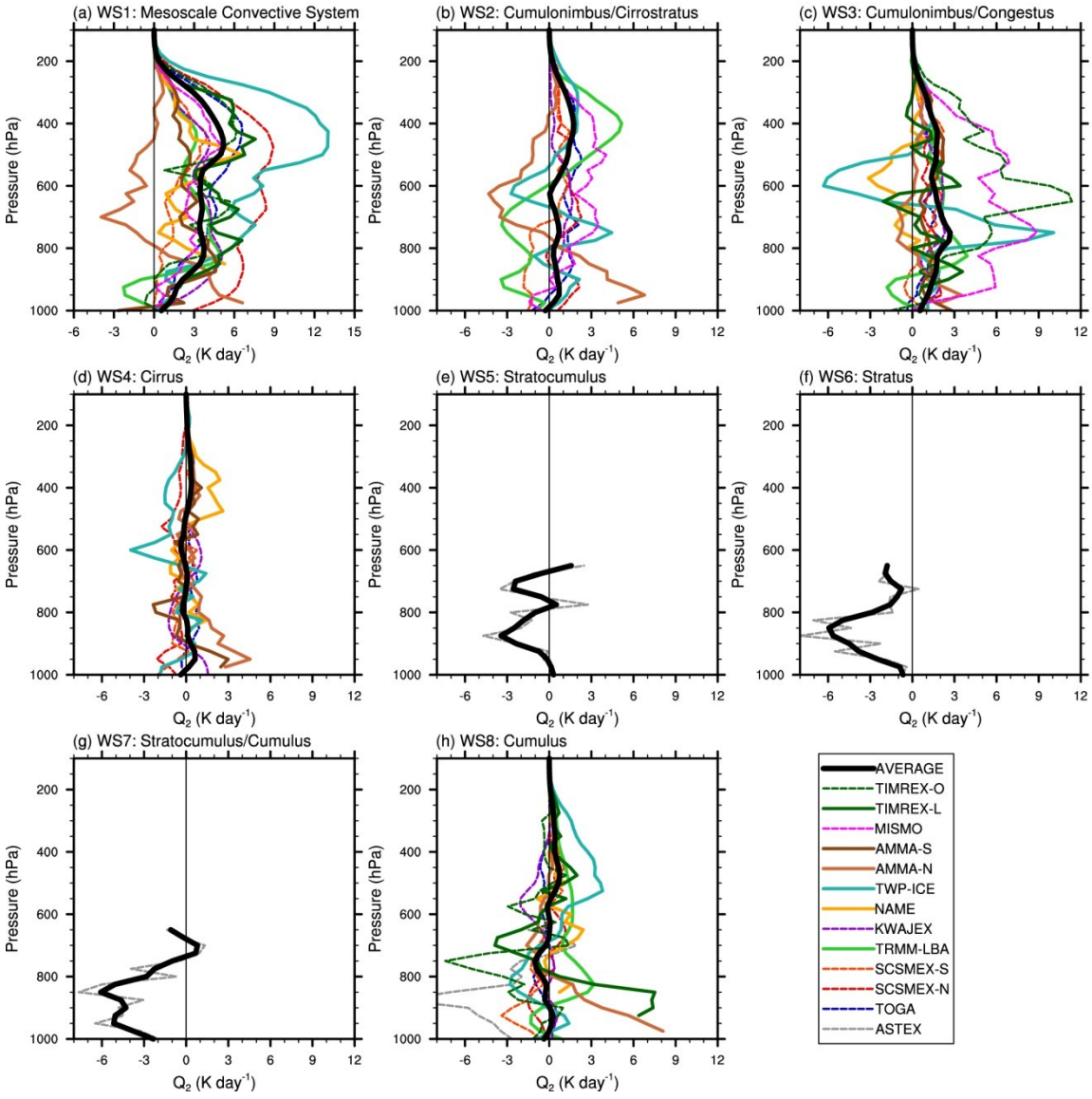

Fig. B-7. Same as Fig. B-4, but for the apparent moisture sink (Q_2).

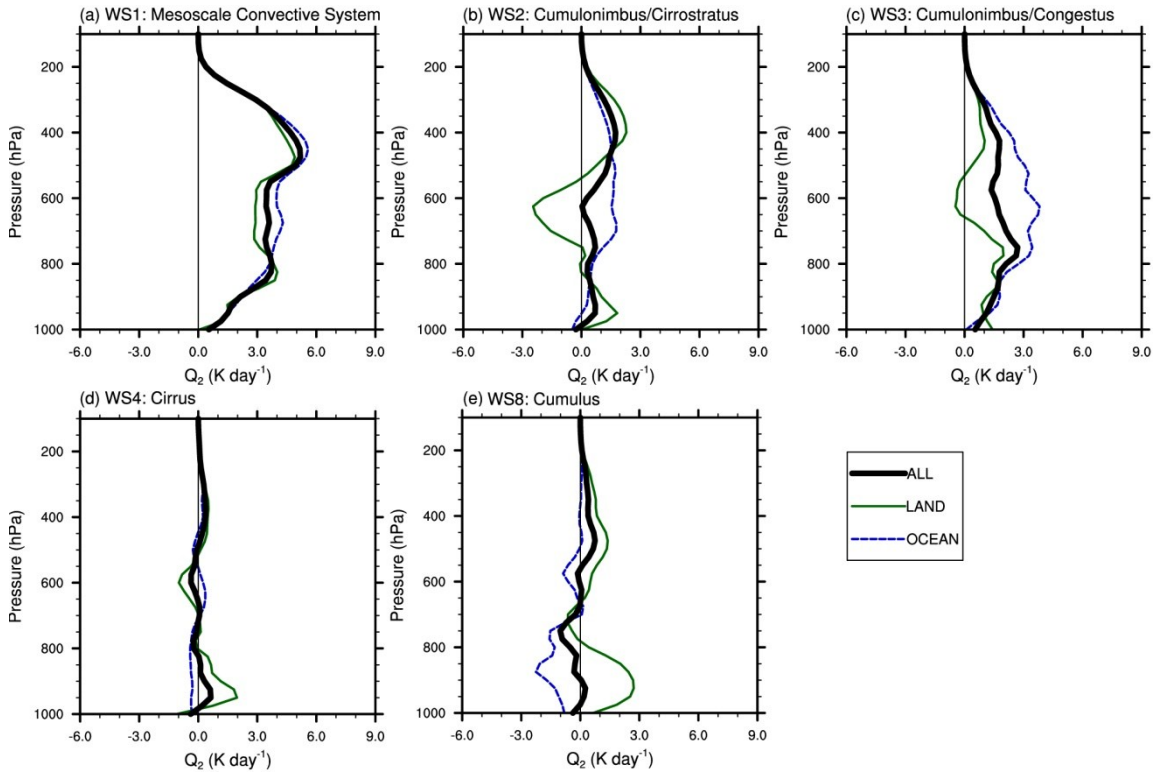

Fig. B-8. Same as Fig. B-6, but for the apparent moisture sink (Q_2).

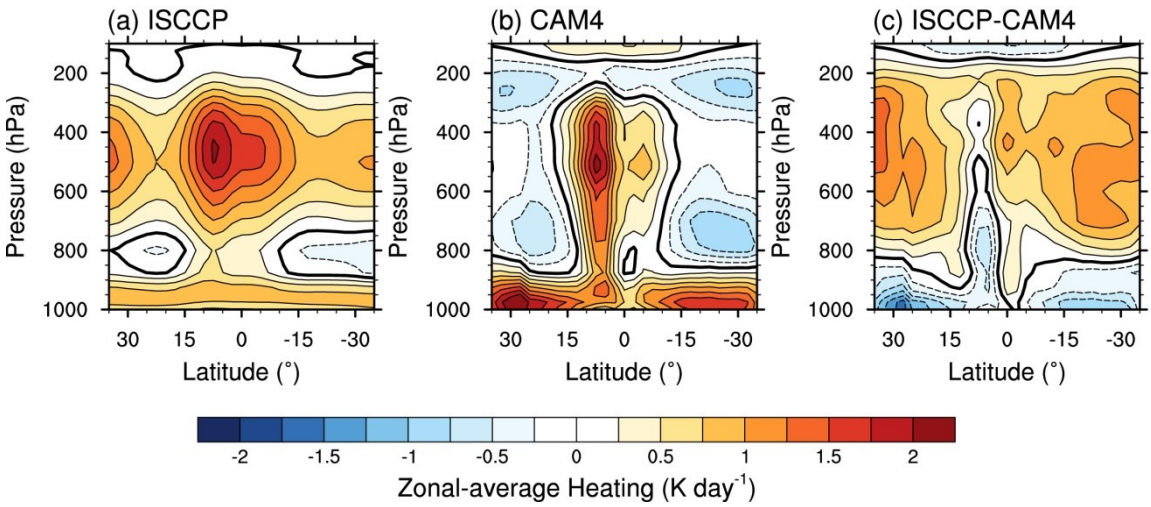

Fig. B-9. Annual average, zonal mean total heating for (a) the ISCCP reconstruction, (b) CAM4 control run, and (c) difference quantities (ISCCP-CAM4) during 1984-2007. Positive (negative) values are indicated with solid (dashed) contours and warm (cold) colors. The thick contour indicates regions where Q_1 equals zero.

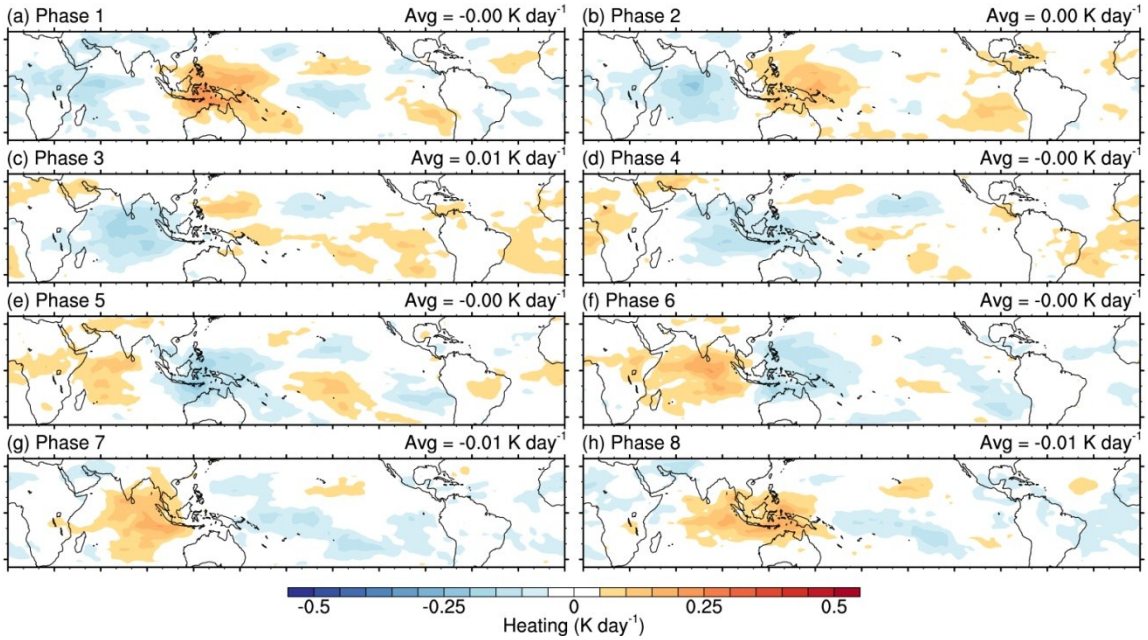

Fig. B-10. ISCCP composite heating anomalies by phase for WS8 (cumulus/shallow convection) at approximately 940 hPa for strong MJO events relative to the six-month (November-April) 1983-2008 mean. Warm (cool) colors indicate greater heating (cooling) during strong MJO events compared to the climatological heating for the regime (regardless of phase).

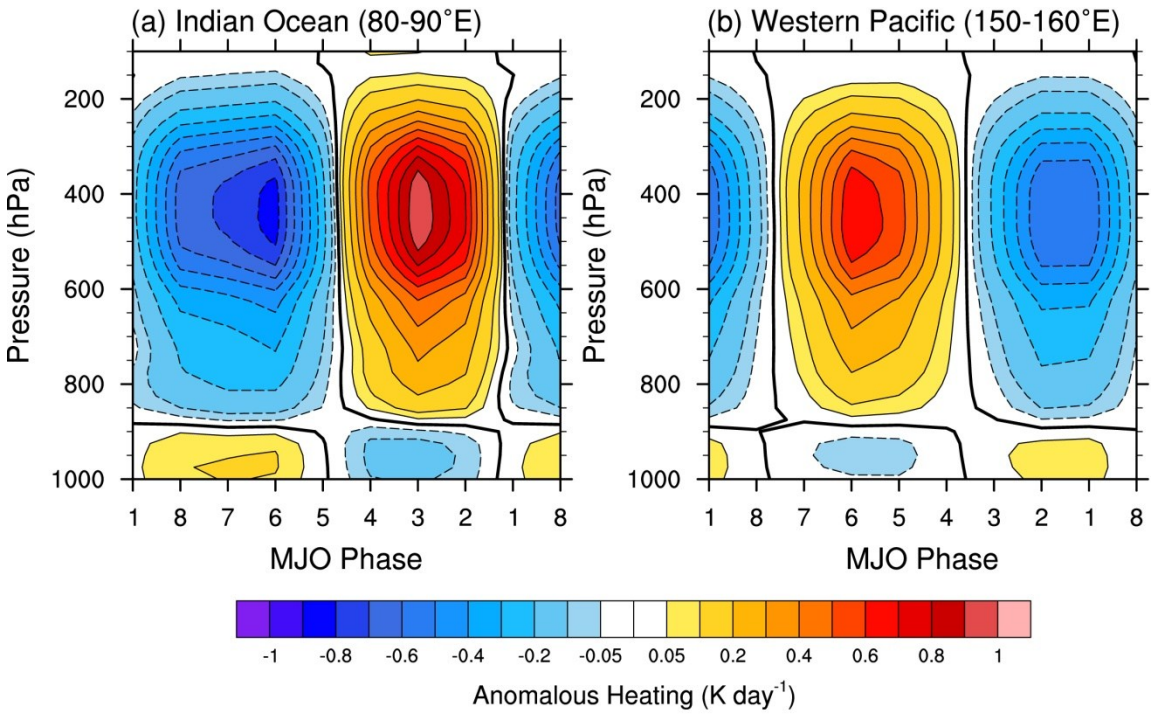

Fig. B-11. Vertical-temporal (MJO phases) evolution of the total ISCCP diabatic heating anomalies for strong MJO events over the (a) Indian Ocean (80°-90°E) and (b) Western Pacific (150°-160°E) throughout November-April, 1983-2008. The Q_1 anomalies are averaged over 5°S-5°N in each domain.

APPENDIX C

TABLES AND FIGURES FOR CHAPTER IV

Table C-1. Cluster Cloud Fraction (CCF) for each weather state from the ISCCP observations and MERRA simulations using a maximum-random and random vertical cloud overlap parameterization.

	Weather State CCF (%)								
Case	WS1	WS2	WS3	WS4	WS5	WS6	WS7	WS8	WS0
Observations	98.6	94.5	82.1	74.8	84.7	74.5	59.7	24.1	0
Maximum-Random	35.5	24.5	26.4	16.6	37.8	29.3	24.8	17.1	3.0
Random	49.0	36.1	40.2	25.4	54.3	42.8	39.8	27.7	4.8

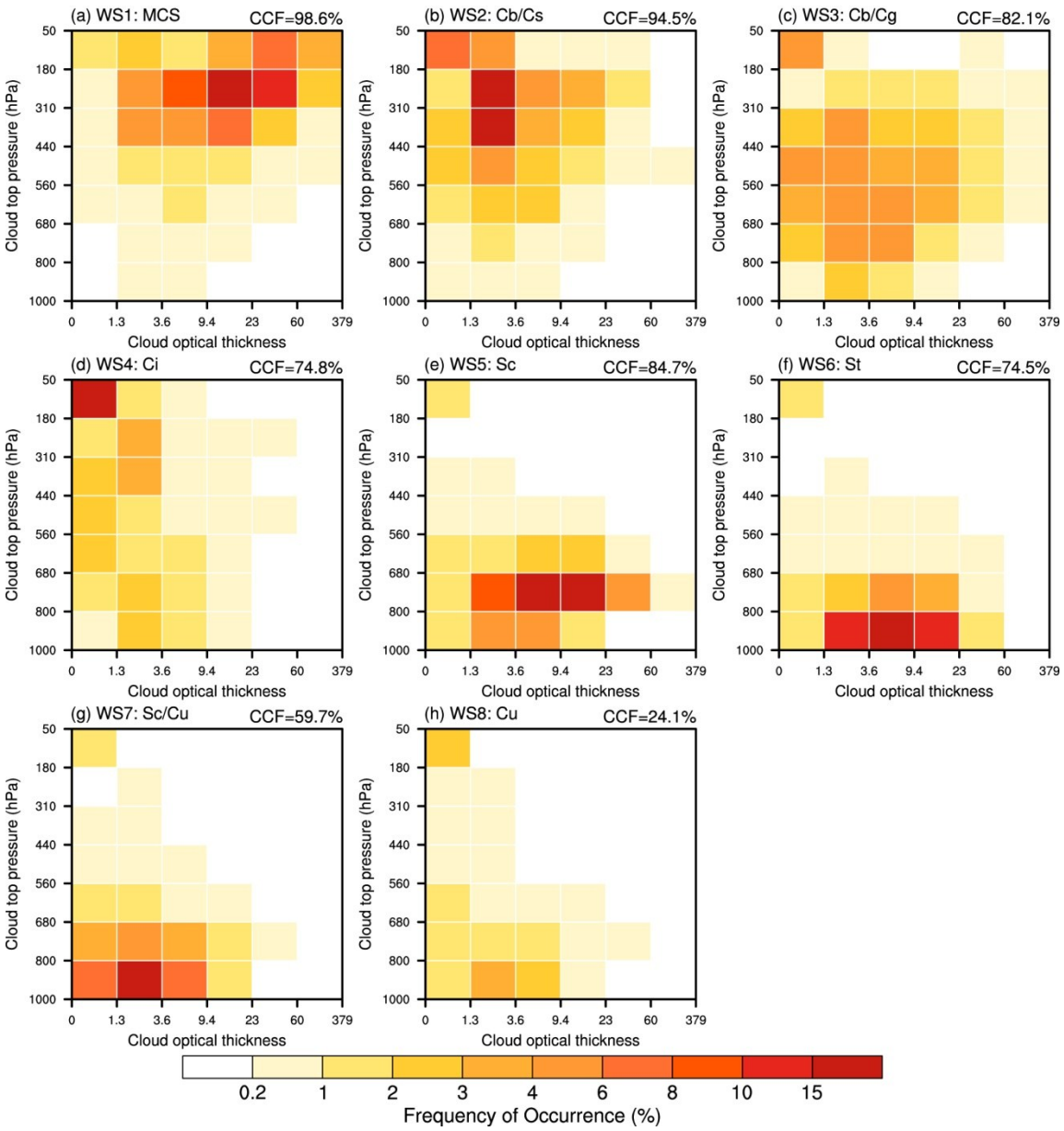

Fig C-1. Joint histograms of cloud-top pressure and optical thickness corresponding to each of the eight cloudy ISCCP weather states for the extended low-latitude dataset. Shading represents the cloud fraction occurring within each bin (i.e., frequency of occurrence) comprising the overall cluster distribution. The cloud fraction sum (i.e., average total cloud cover) is listed at the top for each regime ("cluster cloud fraction" or CCF). A separate weather state (WS0) is not shown and assigned to those ISCCP gridboxes without any cloud cover.

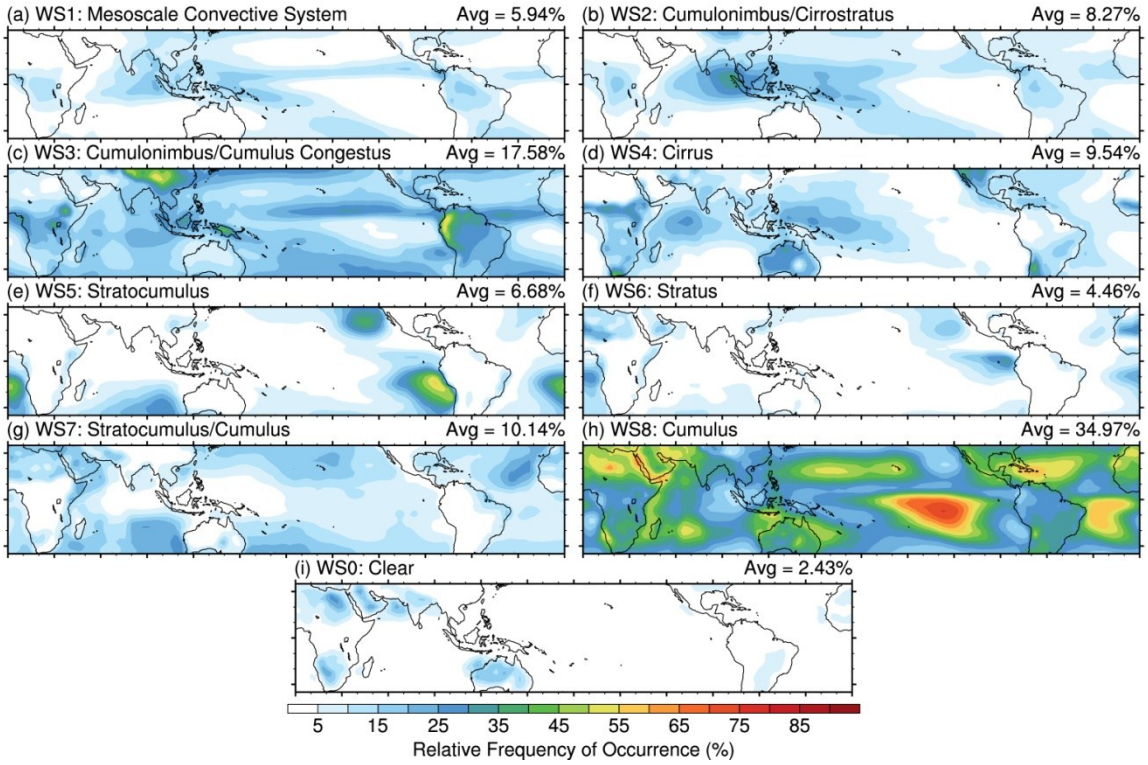

Fig. C-2. Geographic distribution of the annual average, relative frequency of occurrence (RFO) for each ISCCP weather state from 1984-2007. The domain average RFO is listed in the top right for each panel.

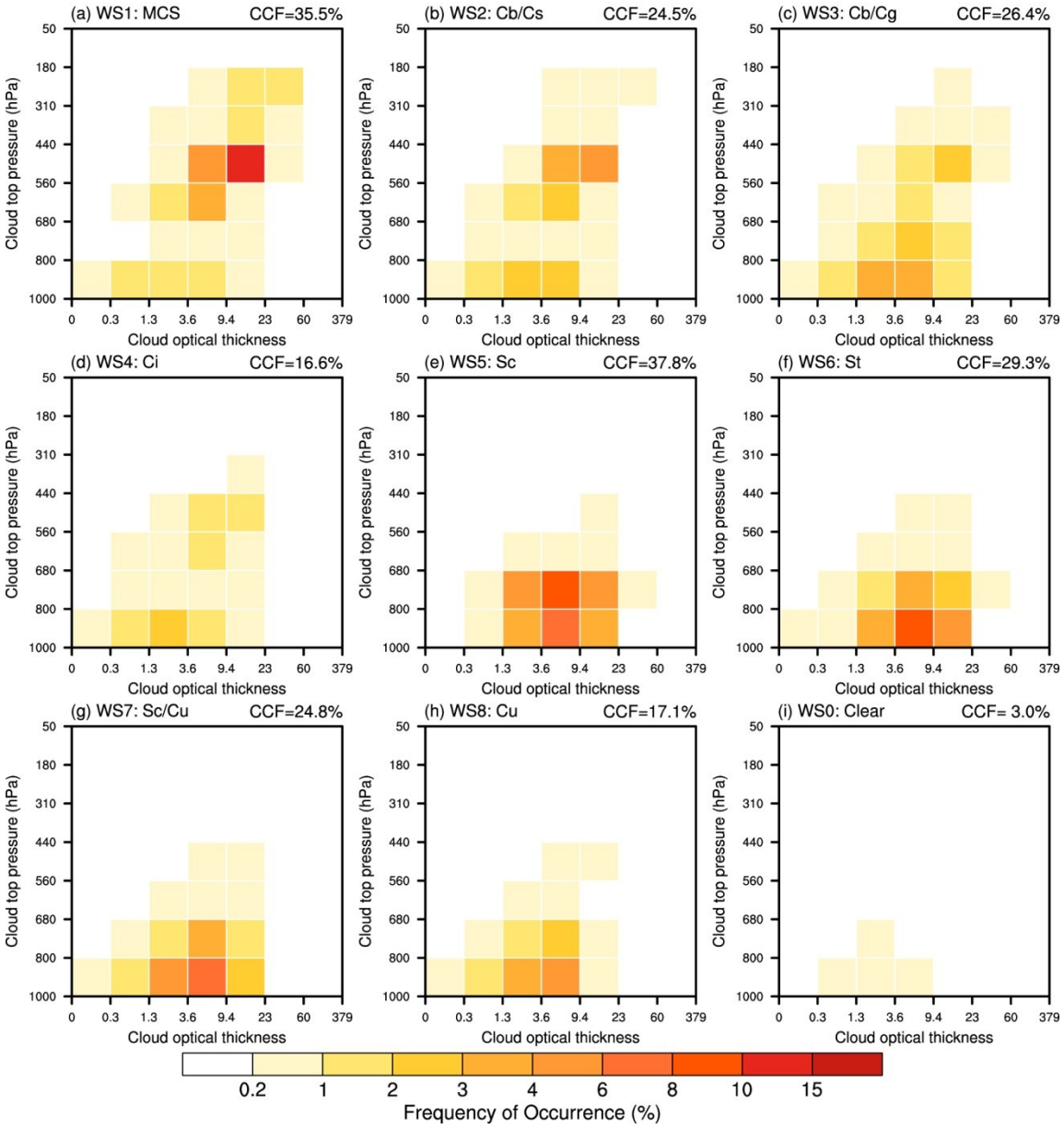

Fig. C-3. Mean histograms of simulated cloud-top pressure and optical thickness corresponding to the observed ISCCP weather states (July 1983-June 2008) using MERRA data and a maximum (convective) and random (large-scale) cloud overlap parameterization. Shading intervals and image interpretation are identical to Fig. C-1.

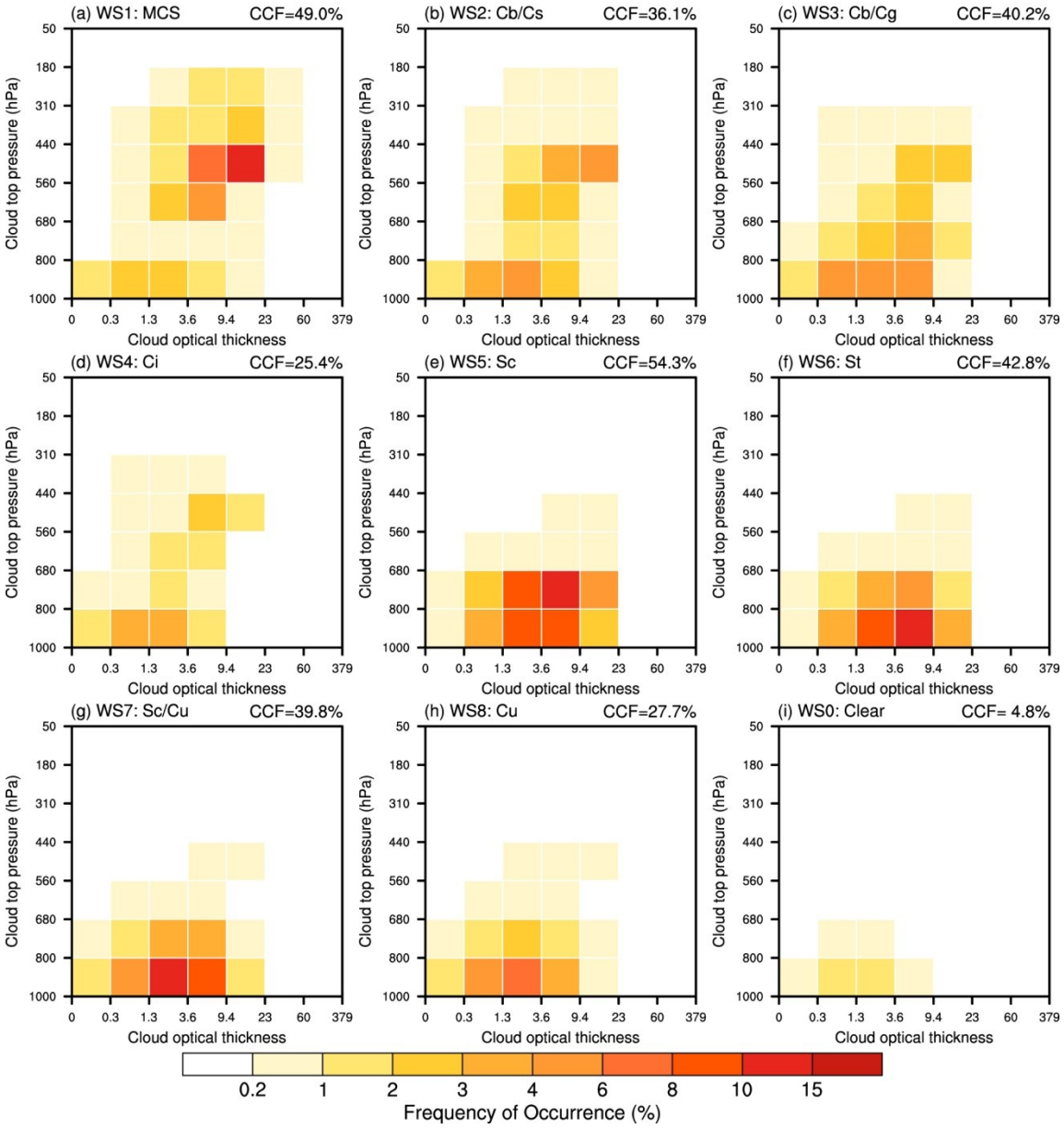

Fig. C-4. Same as Fig. C-3, but using a random (convective and large-scale) vertical cloud overlap parameterization.

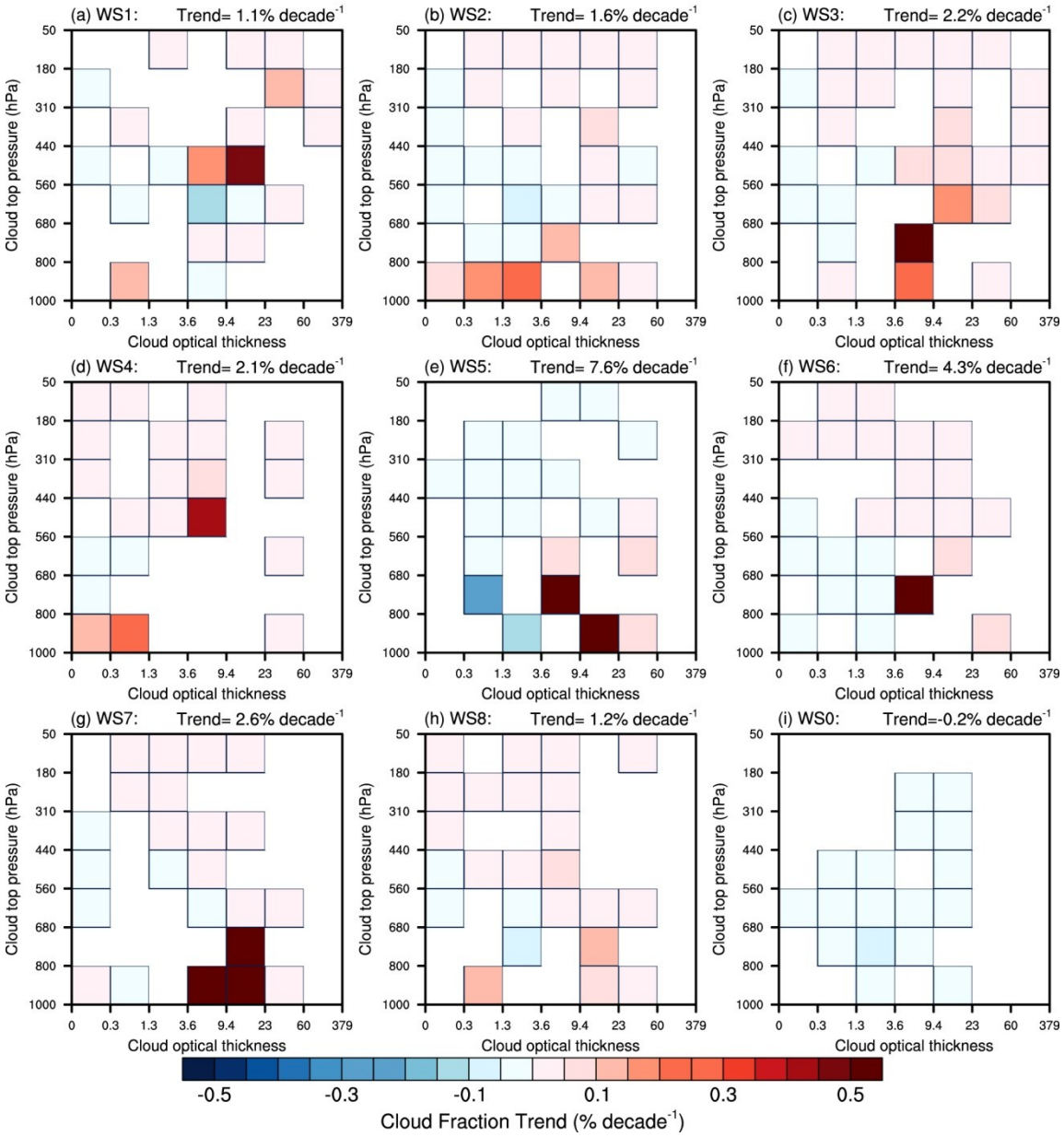

Fig. C-5. Cloud fraction trends for each p_c-τ bin for the entire 25-yr simulation using a maximum-random vertical cloud overlap parameterization. Bins with trends not considered statistically significant (p=0.05) are omitted from the panels. The sum of all statistically significant trends for each regime is included at the top right of each panel (in % decade^{-1}).

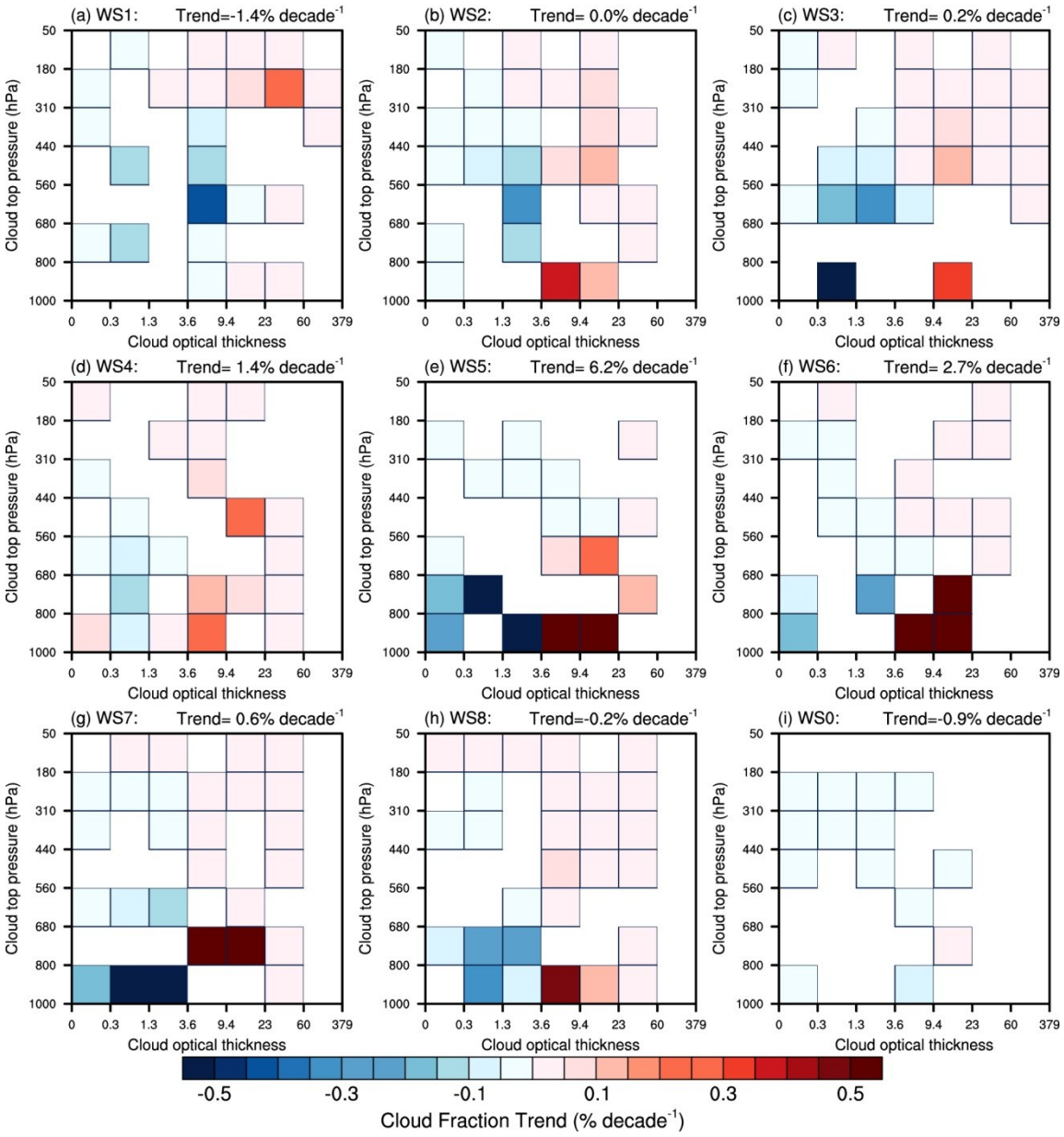

Fig. C-6. Same as Fig. C-5, but for the random vertical cloud overlap parameterization.

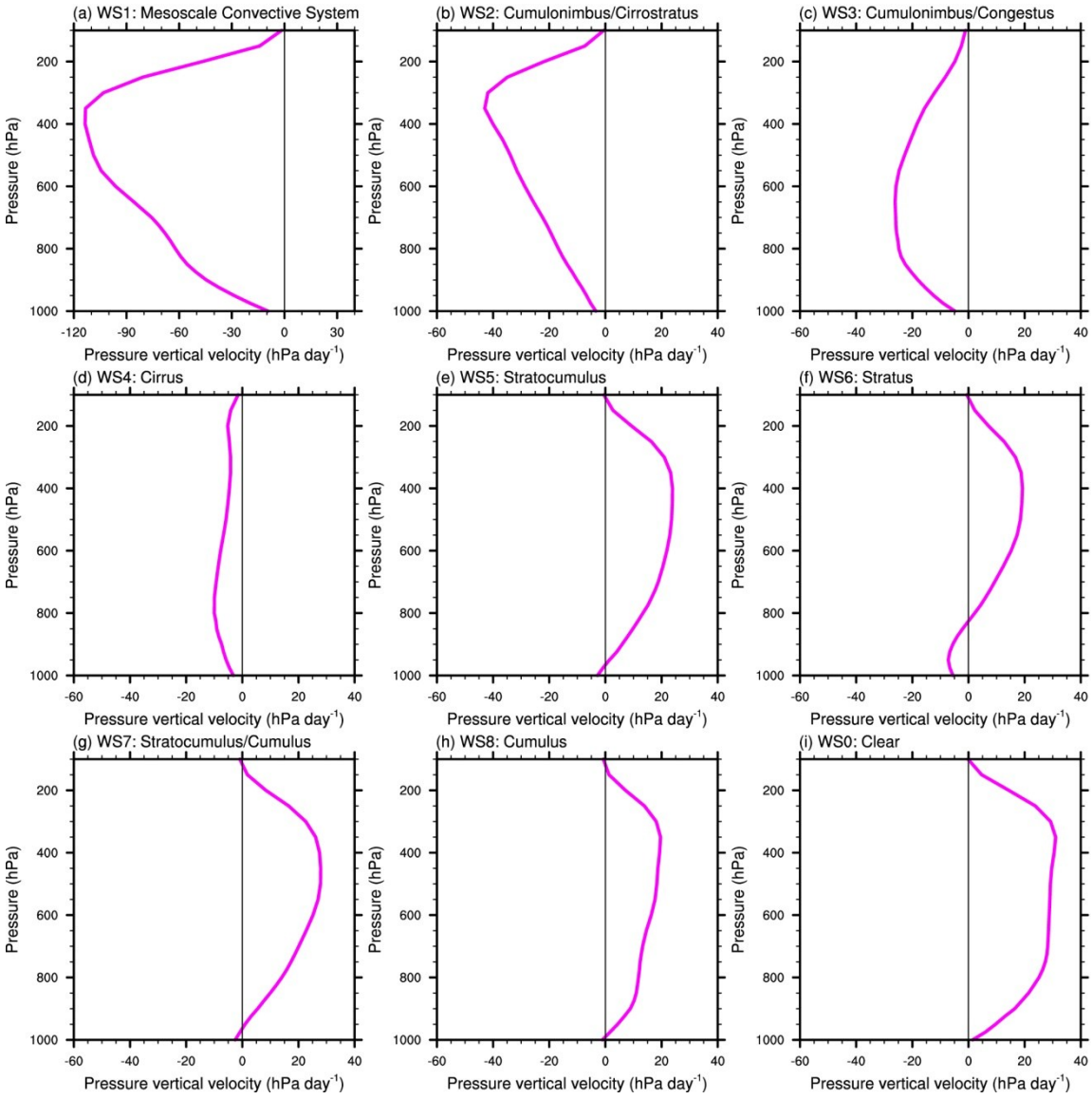

Fig. C-7. Composite pressure vertical velocity profiles (hPa day^{-1}) from MERRA data corresponding to each of the observed ISCCP weather states. The scale used for WS1 is different from the remaining panels.

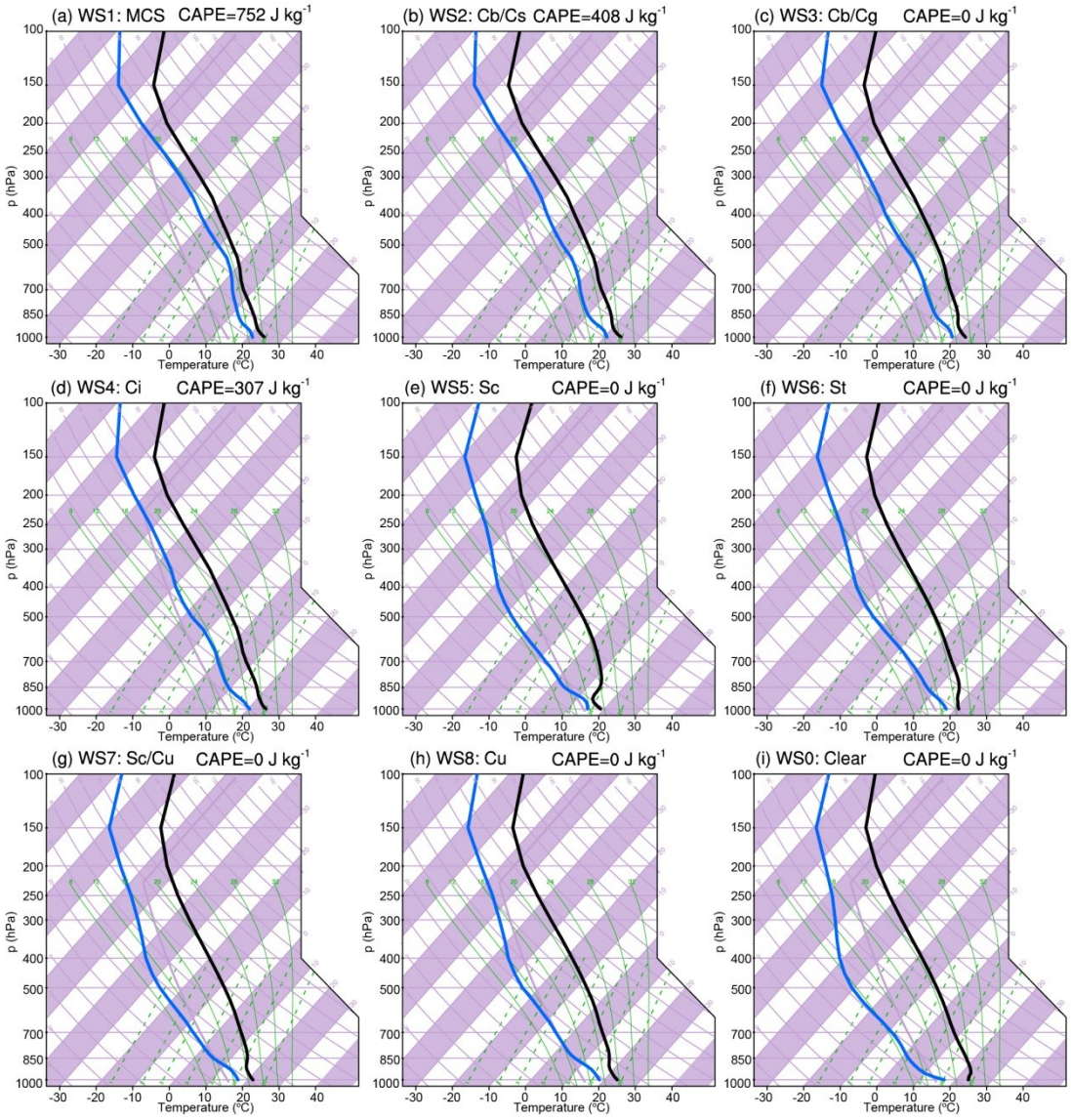

Fig. C-8. Composite soundings from MERRA data corresponding to each of the observed ISCCP weather states.

APPENDIX D

TABLES AND FIGURES FOR CHAPTER V

Table D-1. Trends in annual average quantities from the CAM4 simulations, reanalysis ensemble, and GPCP data for the 1984-2007 period. Units for the streamfunction intensity, HC width, and precipitation are in x 10^{10} kg s^{-1} $decade^{-1}$, ° latitude $decade^{-1}$, and mm day^{-1} $decade^{-1}$, respectively. Significant (95%) values are denoted with an asterisk.

	Realization		
Variable	CAM4-CTRL	ISCCP-CTRL	Reanalysis/GPCP
Ψ_N^*	0.00	-0.23	0.37*
Ψ_S^*	-0.02	-0.13	-0.23
$\Delta\varphi$	-0.62	-0.31	1.12*
HC Precipitation	0.04*	0.01	0.00

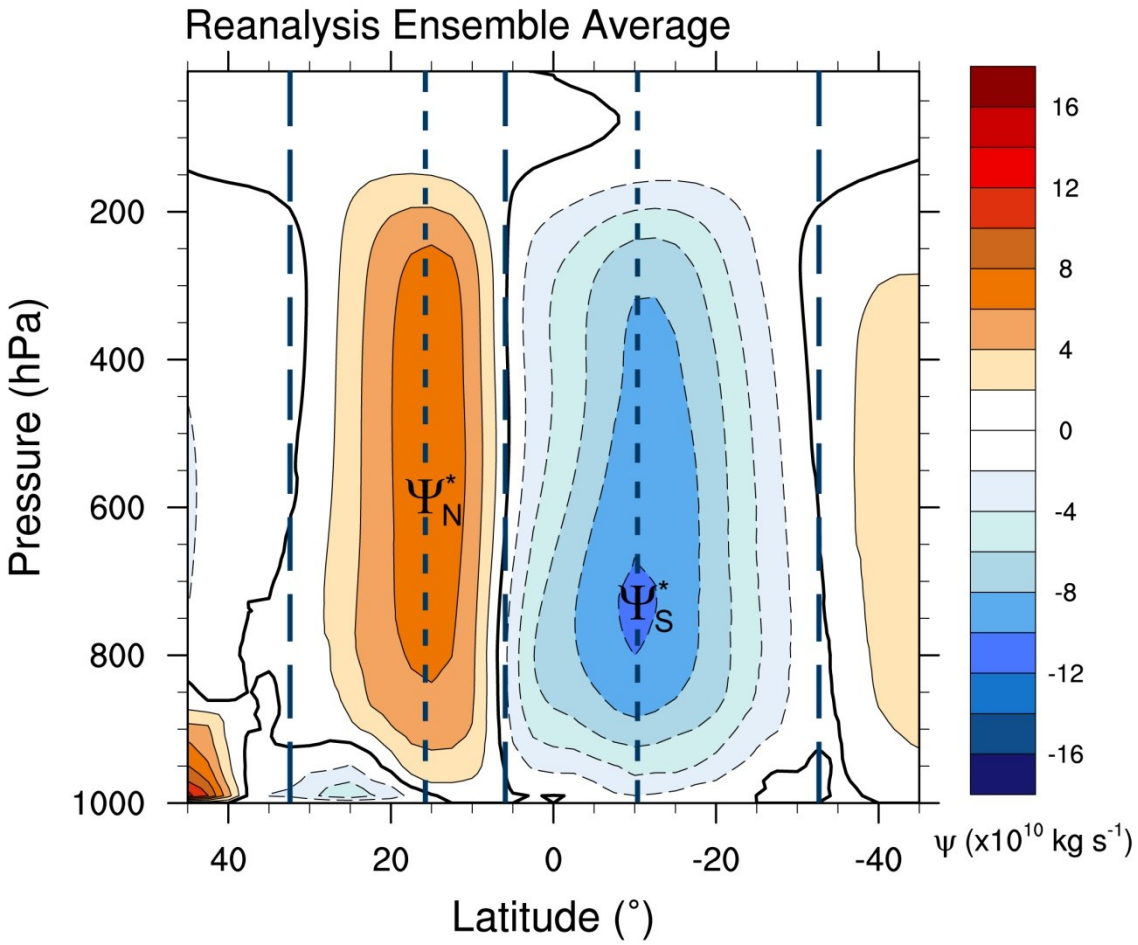

Fig. D-1. Annual average, zonal mean meridional mass streamfunction for the reanalysis ensemble from 1984-2007. Warm (cold) colors and solid (dashed) contours represent counterclockwise (clockwise) circulations. The thick black contour corresponds to values where $\Psi = 0$. The approximate locations of the maximum and minimum streamfunction values are denoted as Ψ_N^* and Ψ_N^*, respectively. Long dashed lines represent the approximate location of the HC boundaries (defined as those locations where the average value of Ψ from 700-400 hPa equals zero) and short dashed lines indicate the center latitude of each cell.

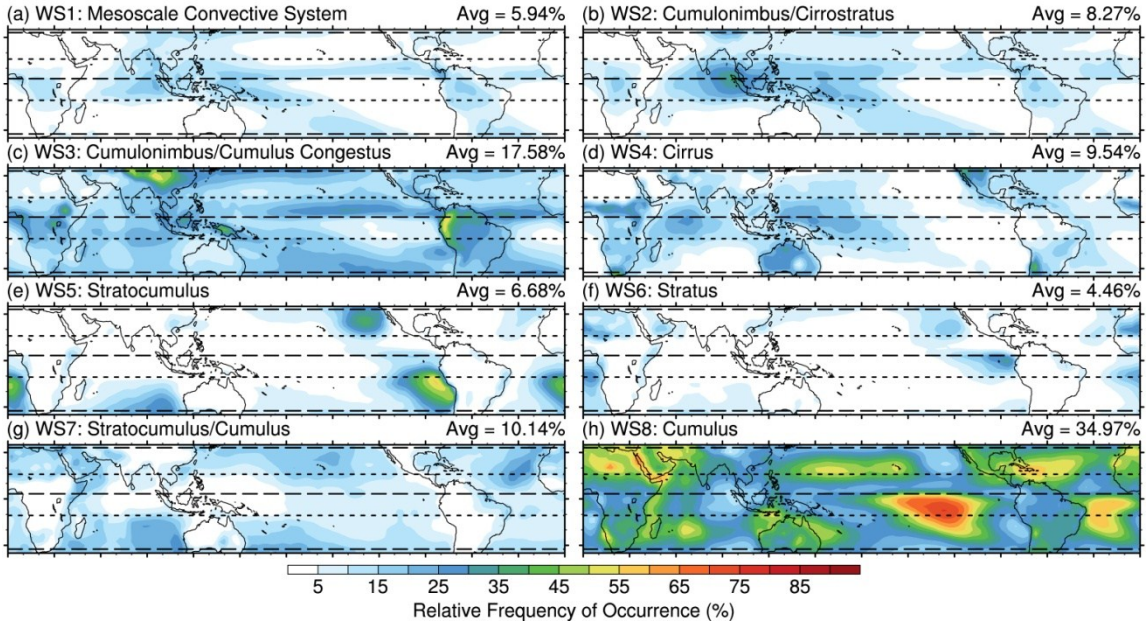

Fig. D-2. Annual average, relative frequency of occurrence (RFO) for each of the ISCCP cloudy weather states from 1984-2007. The long and short dashed lines represent the climatological HC boundaries and center latitudes of each cell taken from the reanalysis ensemble, respectively. The tropical and subtropical domain average RFO is indicated in the top right for each panel.

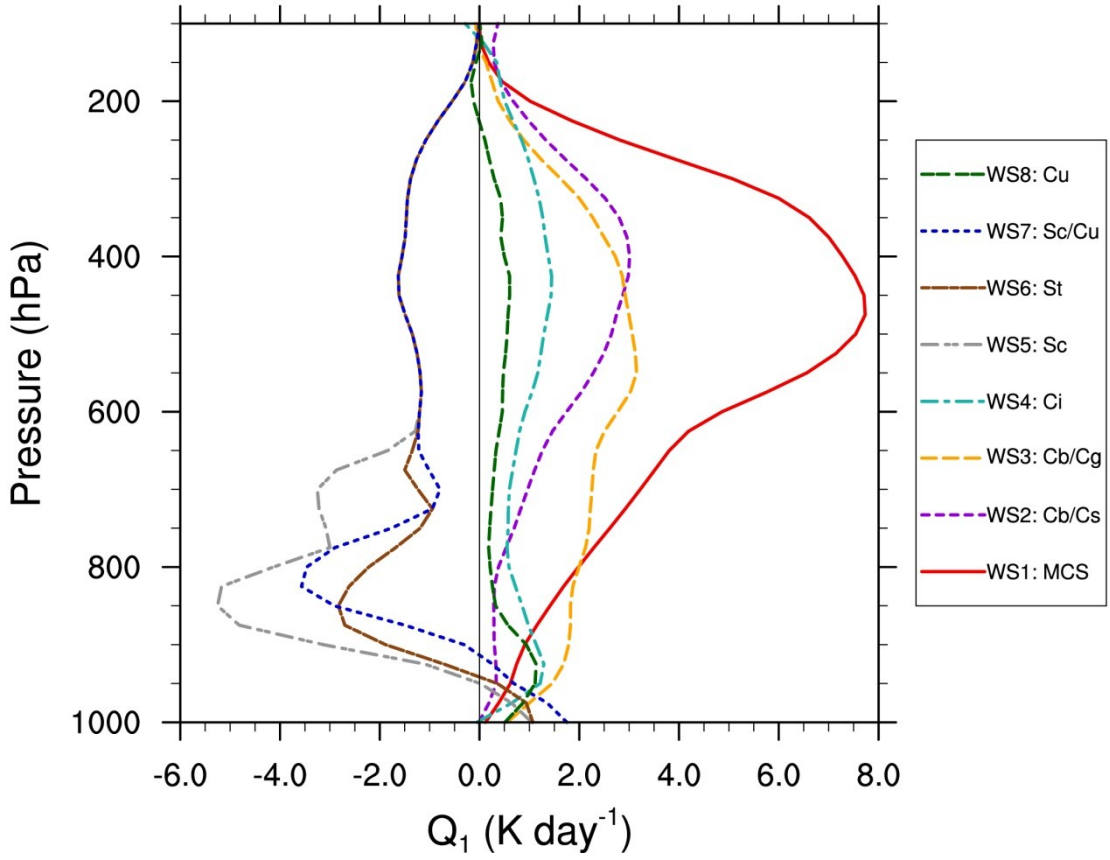

Fig. D-3. Regime-average profiles of the daily average, total diabatic heating (Q_1) for each of the eight ISCCP cloudy weather states. The heating profiles are taken from those calculated by Stachnik et al. (2013).

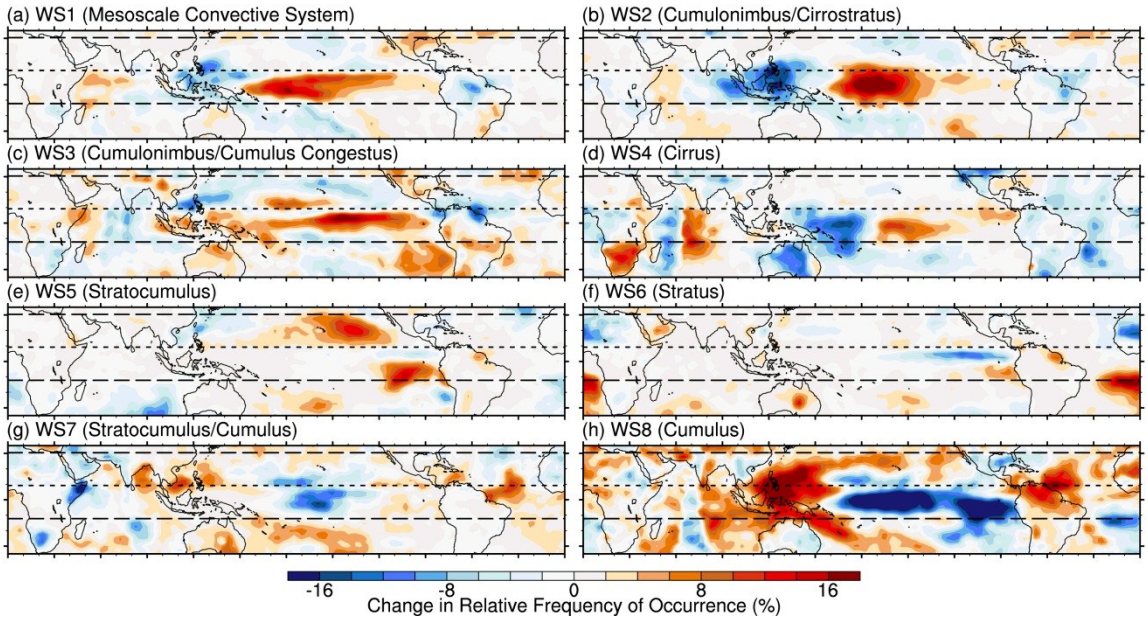

Fig. D-4. Differences in the frequency of occurrence for each weather state corresponding to the times of HC extremes (strong-weak) for the northern hemispheric (dominant, winter) cell during DJF 1983-2008. Warm (cold) colors and positive (negative) values indicate a greater (lesser) RFO of any particular weather state during the years with the strongest intensity. Long and short dashed lines represent the reanalysis ensemble boundaries and center for the NH cell, respectively.

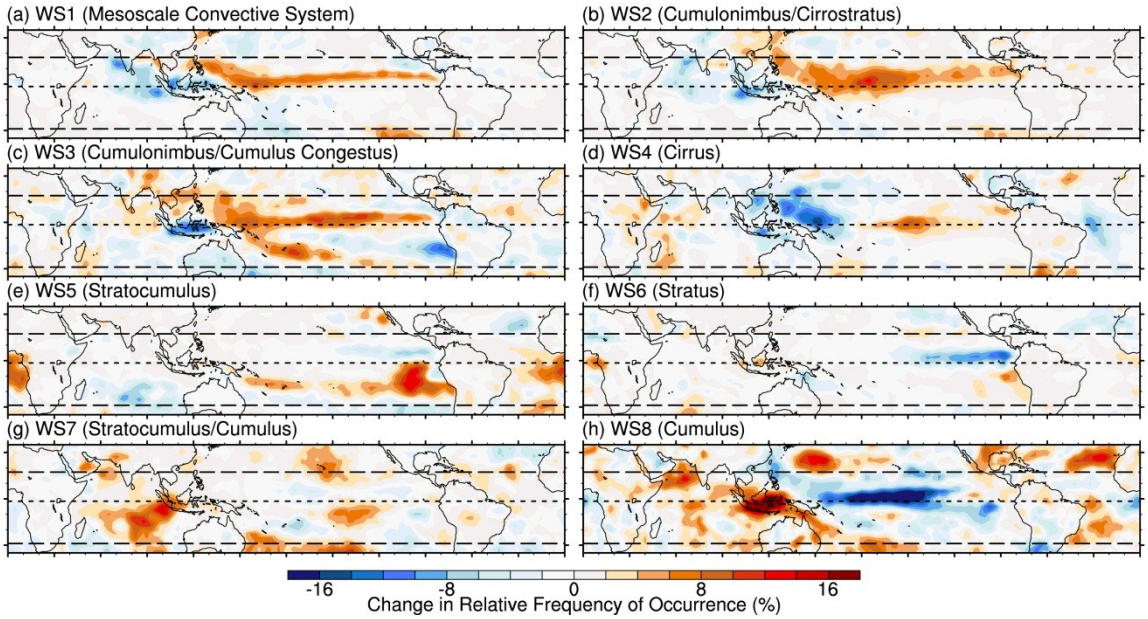

Fig. D-5. Same as Fig. D-4, but for the southern hemispheric (dominant, winter) cell during JJA 1984-2007.

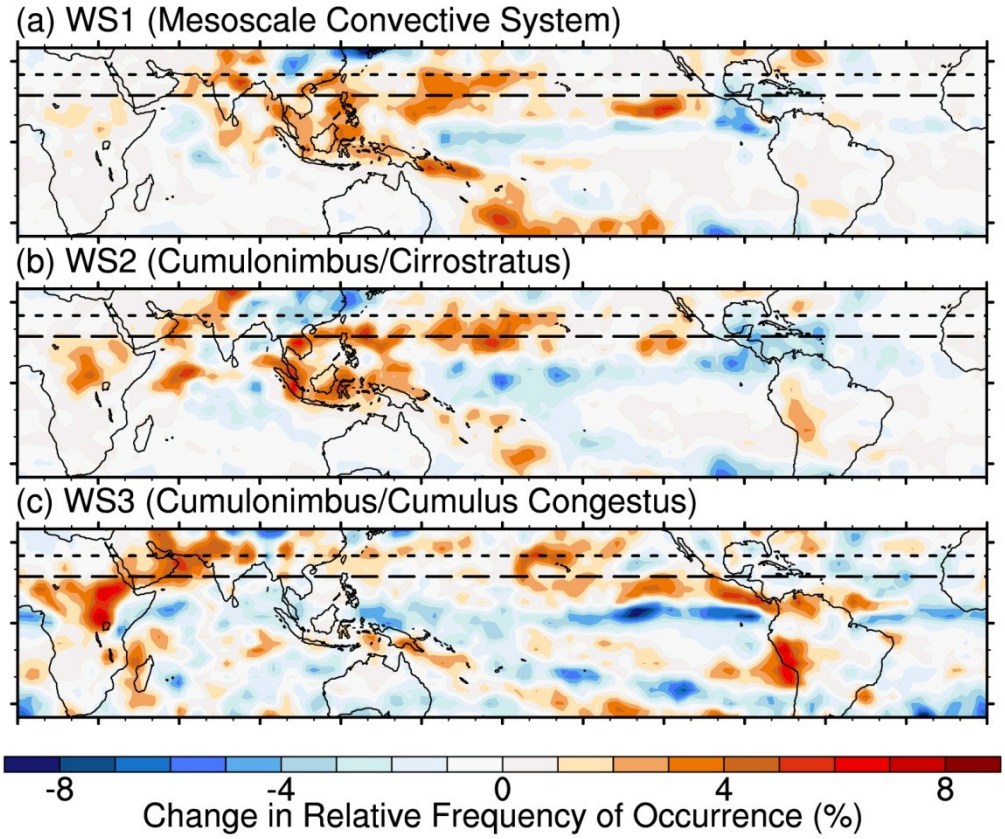

Fig. D-6. Same as Fig. D-4, but for the northern hemispheric (weak, summer) cell during JJA 1984-2007. The scale used differs from that in Figs. D-4 and D-5 for the dominant, winter hemispheric cell. The subtropical terminus of the NH cell is located outside the plot domain.

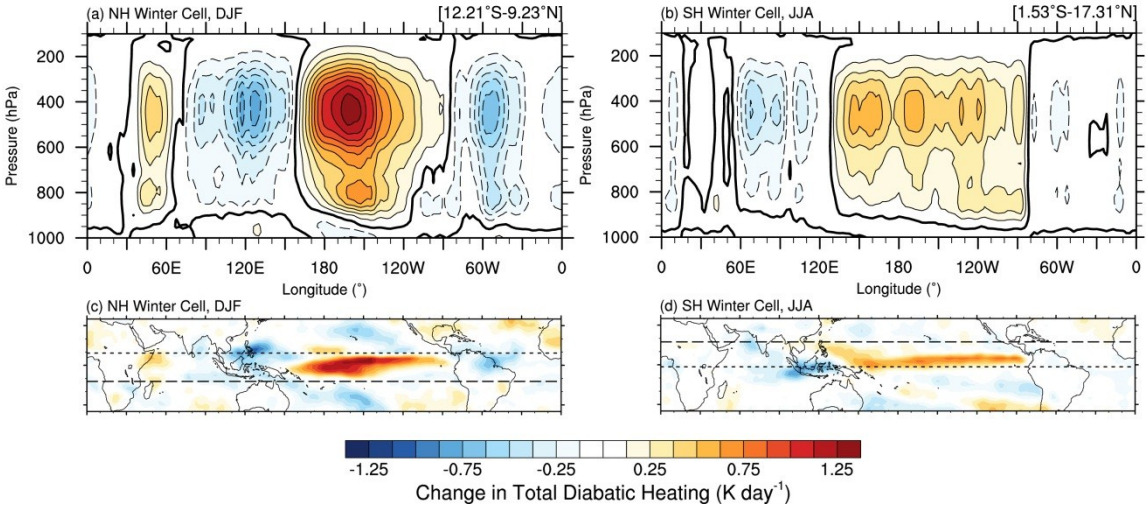

Fig. D-7. Average differences in the ISCCP-derived total heating corresponding to the HC extremes (strong-weak) for the winter hemisphere cell during the 1983-2008 period for the (a) northern hemisphere in DJF and (b) southern hemisphere in JJA. The thick line indicates the zero contour for panels (a) and (b). Heating differences are averaged across all latitudes within the ascending branch (top right of each panel). The corresponding heating differences at 600 hPa are shown in panels (c) and (d) for the NH and SH cell, respectively. Reference lines denote the boundaries of the ascending branch.

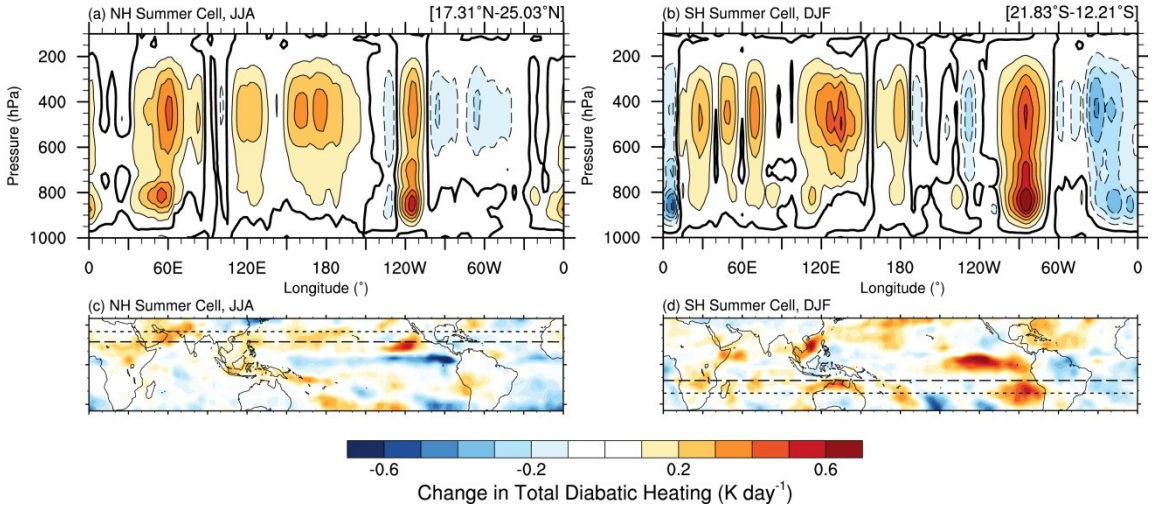

Fig. D-8. Same as Fig. D-7, but for the summer hemisphere cells. Note that the scale used is different from Fig. D-7.

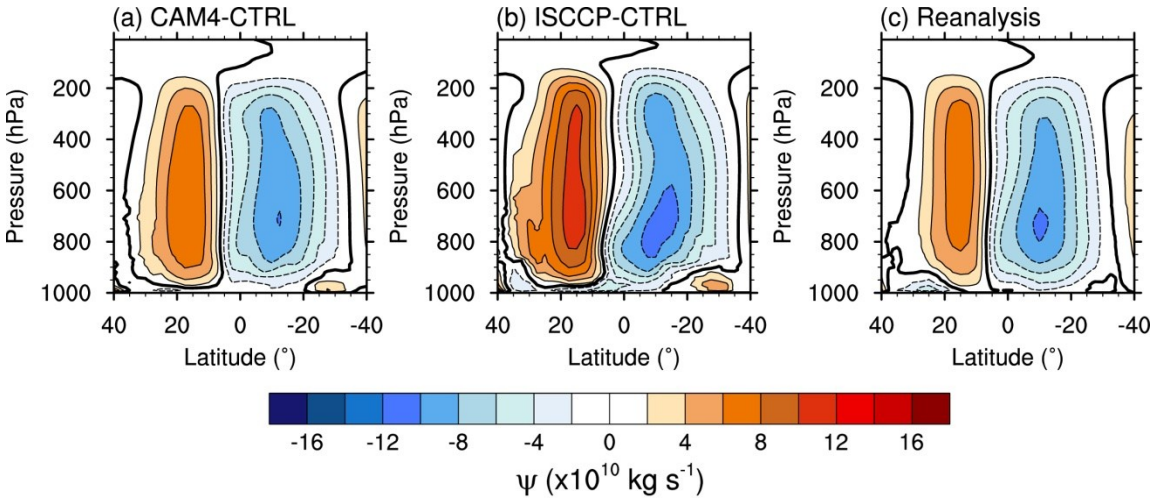

Fig. D-9. Same as Fig. D-1, but for the (a) CAM4-CTRL and (b) ISCCP-CTRL cases. Panel (c) represents the reanalysis ensemble zonal mean meridional mass streamfunction and is identical to that shown in Fig. D-1.

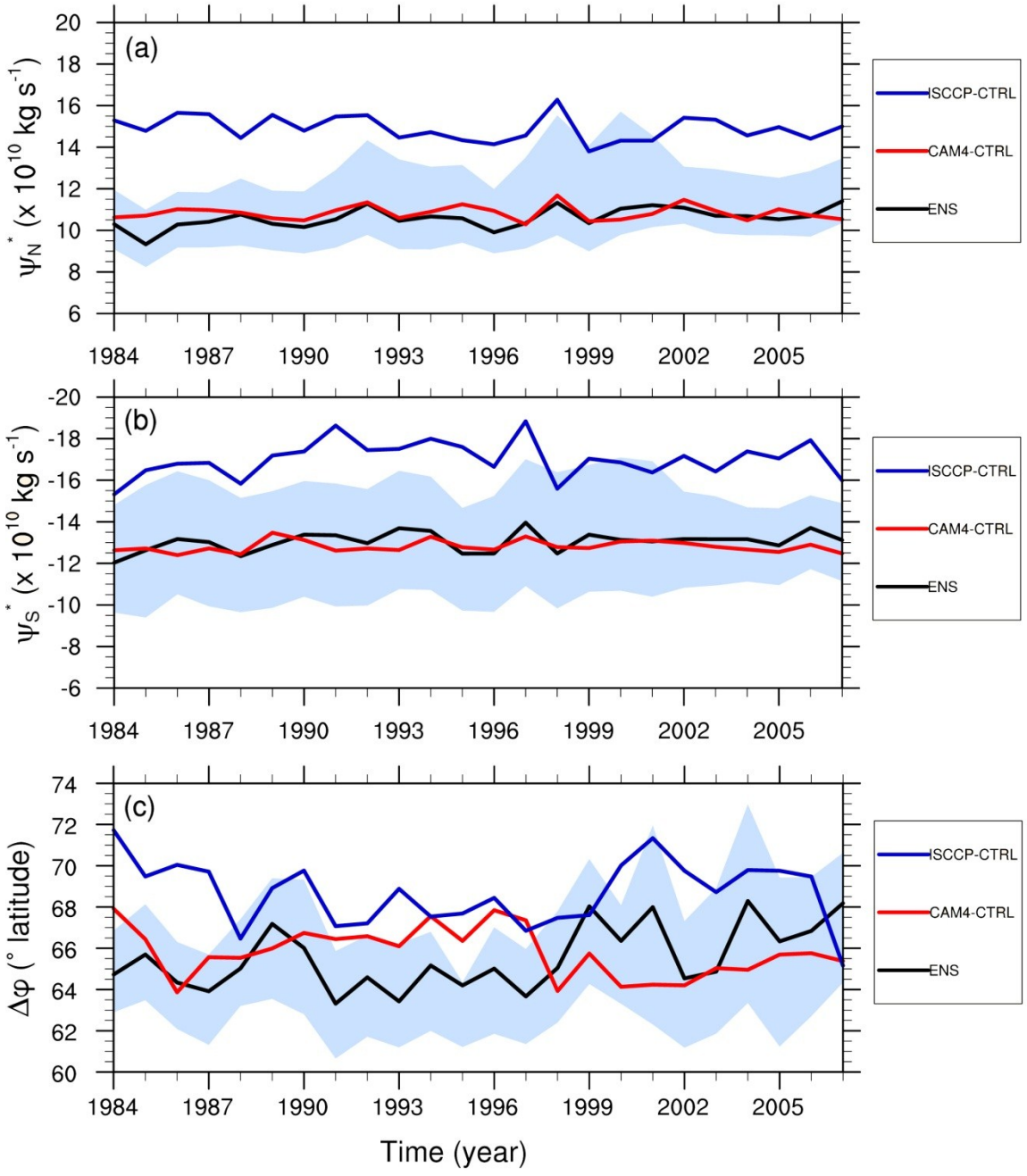

Fig. D-10. Time series of the annual average (a) maximum and (b) minimum meridional mass streamfunction values from the CAM4-CTRL and ISCCP-CTRL simulations for the northern (Ψ_N^*) and southern hemispheric (Ψ_S^*) cells during 1984-2007, respectively. The total HC width ($\Delta\varphi$) is shown in panel (c). The thick black line indicates the HC intensity from the reanalysis ensemble average and the blue shading represents the maximum and minimum values from individual reanalysis datasets.

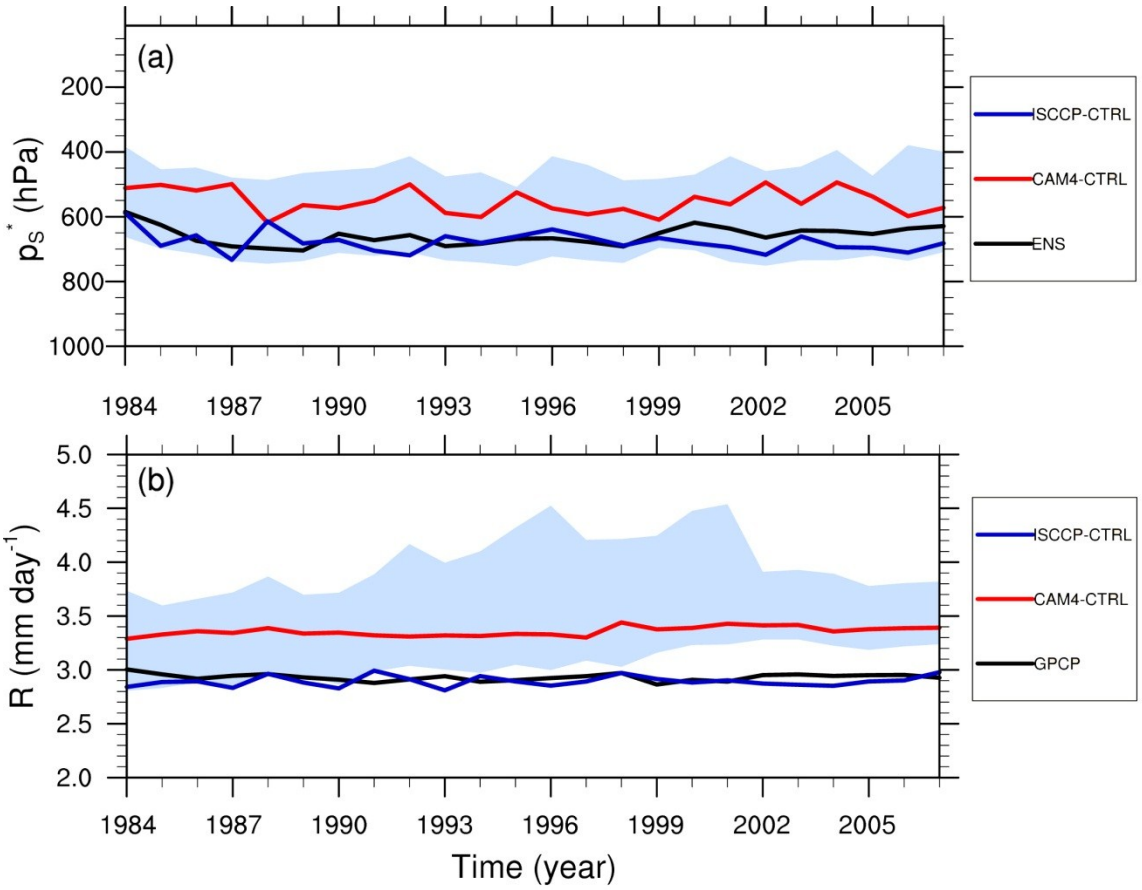

Fig. D-11. Same as Fig. D-10, but for the (a) level of maximum overturning for the southern hemispheric cell and (b) HC domain average precipitation. The thick black line in panel (b) represents the precipitation time series from the GPCP dataset with the blue shading indicating the maximum and minimum values of each variable from the individual reanalyses.